UNIVERSIDADE TECNOLÓGICA FEDERAL DO PARANÁ
PROGRAMA DE PÓS-GRADUAÇÃO EM ENGENHARIA MECÂNICA E DE MATERIAIS

MARCO AURÉLIO FERRARI

A NUMERICAL STUDY OF TWO-PARTICLE SETTLING IN A THIXOTROPIC FLUID USING THE IMMERSED BOUNDARY–LATTICE BOLTZMANN METHOD

Dissertação

CURITIBA
2021

MARCO AURÉLIO FERRARI

A NUMERICAL STUDY OF TWO-PARTICLE SETTLING IN A THIXOTROPIC FLUID USING THE IMMERSED BOUNDARY–LATTICE BOLTZMANN METHOD

Estudo Numérico da Sedimentação de Duas Partículas em Fluido Tixotrópico utilizando o Método de Lattice Boltzmann e Fronteira Imersa

MSc dissertation presented to the Postgraduate Program in Mechanical and Materials Engineering (PPGEM) from The Federal University of Technology - Paraná, as partial fulfilment of the requirements for the degree of Master of Sciences.

Advisor: Prof. Dr. Admilson Teixeira Franco

CURITIBA

2021

Ministério da Educação
Universidade Tecnológica Federal do Paraná
Câmpus Curitiba

MARCO AURELIO FERRARI

ESTUDO NUMÉRICO DA SEDIMENTAÇÃO DE DUAS PARTÍCULAS EM FLUIDO TIXOTRÓPICO UTILIZANDO O MÉTODO DE LATTICE BOLTZMANN E FRONTEIRA IMERSA

Trabalho de pesquisa de mestrado apresentado como requisito para obtenção do título de Mestre Em Engenharia da Universidade Tecnológica Federal do Paraná (UTFPR). Área de concentração: Engenharia Térmica.

Data de aprovação: 05 de Fevereiro de 2021

Prof Admilson Teixeira Franco, Doutorado - Universidade Tecnológica Federal do Paraná

Prof Christian Naaktgeboren, - Universidade Tecnológica Federal do Paraná

Prof Paulo Cesar Philippi, Doutorado - Pontifícia Universidade Católica do Paraná (Pucpr)

Prof Silvio Luiz De Mello Junqueira, Doutorado - Universidade Tecnológica Federal do Paraná

Documento gerado pelo Sistema Acadêmico da UTFPR a partir dos dados da Ata de Defesa em 01/03/2021.

ACKNOWLEDGMENT

"Imagination will often carry us to worlds that never were,
but without it we go nowhere."
Carl Sagan (*1934 †1996)

RESUMO

FERRARI, Marco Aurélio. **Estudo Numérico da Sedimentação de Duas Partículas em Fluido Tixotrópico utilizando o Método de Lattice Boltzmann e Fronteira Imersa**. Dissertação de Mestrado. Programa de Pós-Graduação em Engenharia Mecânica e de Materiais, Universidade Tecnológica Federal do Paraná, Curitiba, Brasil, 110 páginas, 2020.

A sedimentação de múltiplas partículas em fluidos não newtonianos tem grande relevância industrial. Durante a operação de perfuração na exploração de óleo e gás, cascalhos necessitam ser retirados do poço. Para a tarefa é utilizado fluidos de perfuração que carregam os cascalhos para a superfície. Os fluidos de perfuração têm certas propriedades, que no evento de parada, são capazes de reduzir a velocidade no qual os cascalhos sedimentam e consequentemente reduzir a taxa que acumulam no fundo do poço. A capacidade do fluido aumentar sua viscosidade e tensão limite de escoamento é associada com a tixotropia, propriedade dependente do tempo que aumenta o nível de estruturação das partículas presentes no fluido. O problema estudado consiste da sedimentação de esferas soltas em repouso em fluido inicialmente desestruturado, que ao longo do tempo reestrutura-se e aumenta sua tensão de escoamento. Portanto ter uma forma confiável de investigar os efeitos das propriedades do fluido na sedimentação é importante. Para atingir o objetivo, foi proposto modelo numérico baseado no metodo de lattice Boltzmann acoplado com metodo da fronteira imersa, com implementação em linguagem CUDA®/C++. O efeito tixo-viscoplástico foi implementado utilizando uma segunda função de distribuição de partículas, sendo responsável pelo transporte do parâmetro estrutural no escoamento. A dinâmica das partículas possuem seis graus de liberdade, enquanto que para colisão foi utilizado o modelo de esfera macia. O código numérico então foi verificado em etapas para aferir cada componente do método, considerados satisfatórios e permitiram a continuidade do estudo da sedimentação em fluido tixo-viscoplástico. A primeira parte do estudo compreendeu avaliar o comportamento das partículas que sedimentam em função do números de Bingham e do parâmetro estrutural computando a quebra e reconstrução. Os dados para velocidade terminal permitiram propor correlação numérica em função dos parâmetros variados. Na segunda parte foi avaliado o efeito que a propriedades do fluido tem na interação entre duas partículas. Os resultados mostraram que existem diferentes regimes de interação entre as partículas, onde para alguns casos o processo de "aproximação-colisão-tombamento" não ocorre, enquanto em outros casos as partículas continuaram a sedimentar em condições que não ocorreram com uma única.

Palavras-Chave: Sedimentação de Partículas, Tensão de Limite de Escoamento, Tixotropia, método lattice Boltzmann, Fronteira Imersa.

ABSTRACT

FERRARI, Marco Aurélio **A Numerical Study of Two-Particle Settling in a Thixotropic Fluid using the Immersed Boundary–Lattice Boltzmann Method** . Master of Science Dissertation. Postgraduate Program in Mechanical and Materials Engineering, The Federal University of Technology - Paraná, Curitiba, Brazil, 110 pages, 2020.

The settling of multiple particles in non-Newtonian fluids has great industrial importance. During the drilling operation in the oil and gas exploration, cuttings need to be removed from the borehole. The task is accomplished by a drilling fluid is used to transport these cuttings to the surface. The drilling fluid may have certain properties, that in the event of pumping stop, are capable of reducing the cuttings settling velocity and consequently reduce the build-up rate at the bottom of the borehole. The fluid's ability to increase its viscosity and yield-stress is associated with thixotropy, a time-dependent property caused by the increasing structuring level of the particle present in the fluid. The studied problem then consists of spheres settling released from rest in an initially unstructured fluid which will be structured over time and increase its yield stress. Therefore have a reliable form to study the effects of fluid properties in this problem is important. The objetive is achieved by using a numerical model based on the lattice Boltzmann method coupled with the immersed boundary method, with its implementation in CUDA®/C++. The thixo-viscoplastic effect was implemented with the use of secondary particle distribution function, which was responsible for transporting the structural parameter in the flow. The particle dynamics had a six degree of freedom and the collision model used a soft-sphere approach. The numerical code was then verified in steps to assess each component of the numerical method. The results were considered satisfactory and allowed to proceed with the study of particles settling in a thixo-viscoplastic fluid. The first part of the study included evaluating of the settling behavior of a single sphere as a function of the Bingham numbers, breakdown, and build-up parameters. The data for terminal velocity then allowed the construction of numerical correlation as a function of the studied parameters. The second part of the study encompassed studying of the effects of the fluid properties in the interaction between the two settling particles. It was found different interactions regimes between the particles, where some cases did not perform the draft-kissing-tumbling process while others the particles continued to settle in conditions where a single particle would not.

Keywords: Particles Settling, Yield-Stress, Thixotropy, lattice-Boltzmann method, Immersed Boundary.

LIST OF FIGURES

LIST OF TABLES

LIST OF ABBREVIATIONS AND ACRONYMS

BGK	Bhatnagar-Gross-Krook Collision Operator
BHA	Bore Hole Assembly
CFD	Computational Fluid Dynamics
CPU	Central Processing Unit
DEM	Discrete Element Method
DKT	Drafting-Kissing-Tumbling
FEM	Finite Element Method
FVM	Finite Volume Method
GLVM	Generalized Linear Viscoelastic Model
GNF	Generalized Newtonian Fluid
GPU	Graphics Processing Unit
HPC	High-Performance Computing
IBM	Immersed Boundary Method
LBM	Lattice Boltzmann Method
LGA	Lattice Gas Automata
MRT	Multi Relaxation Time
MLUPS	Million Lattices Updates per Second
NEBB	Non-Equilibrium Bounce-Back Method
TRT	Two Relaxation Time

NOMENCLATURE

Latin letters

A	Eq. 2.2	Cross-section area	$[\mathrm{m}^2]$
c	Eq. 4.4	Velocity set vector	$[-]$
C	Eq. 2.2	Coefficient	$[-]$
d	Eq. 4.2	Number of spatial dimensions	$[-]$
D	Eq. 2.1	Diameter	$[\mathrm{m}]$
$\mathfrak{D}$	Eq. 4.26	Diffusion coefficient	$[\mathrm{m}^2\,\mathrm{s}^{-1}]$
E_p	Eq. 4.58	Stiffness collision parameter	$[\mathrm{m}\,\mathrm{N}^{-1}]$
f	Eq. 4.1	Particle distribution function	$[\mathrm{s}^{\mathrm{d}}\,\mathrm{m}^{-2\mathrm{d}}]$
$\mathbf{F}$	Eq. 2.1	Force	$[\mathrm{N}]$
$\mathbf{g}$	Eq. 4.1	Acceleration field	$[\mathrm{m}\,\mathrm{s}^{-2}]$
g	Eq. 4.27	Secondary particle distribution function	$[\mathrm{s}^{\mathrm{d}}\,\mathrm{m}^{-2\mathrm{d}}]$
h	Eq. 4.38	Lattice size	$[lu]$
$\boldsymbol{I}$	Eq. 4.54	Inertia tensor	$[\mathrm{kg}\,\mathrm{m}^2]$
k	Eq. 4.2	Boltzmann constant	$[\mathrm{kg}\,\mathrm{m}^2\,\mathrm{s}^{-2}\,\mathrm{K}^{-1}]$
K	Tab. 2.2	Consistency index	$[\mathrm{Pa}\,\mathrm{s}]$
k_1	Tab. 2.4	Breakdown parameter	$[-]$
k_2	Tab. 2.4	Build-up parameter	$[\mathrm{s}^{-1}]$
L	Eq. 2.10	Length	$[\mathrm{m}]$
m	Eq. 4.2	Particle mass	$[\mathrm{m}]$
n	Eq. 4.2	Number of particles	$[-]$
p	Eq. 4.31	Pressure	$[\mathrm{Pa}]$
q	Eq. 4.26	Source term	$[\mathrm{s}^{-1}]$
r	Eq. 4.40	Distance between Lagrangian and Eulerian nodes	$[-]$
R	Eq. 4.58	Radius	$[\mathrm{m}]$
$\mathcal{R}$	Fig. 5.2	Eulerian mesh and Langragian mesh size	$[-]$
$\boldsymbol{R}$	Eq. 4.57	Rotation matrix	$[-]$
$\mathbf{s}$	Fig. 4.6	Lagrangian parametric coordinates	$[-]$
S	Eq. 4.42	Surface area	$[\mathrm{m}^2]$
t	Eq. 4.1	Time	$[\mathrm{s}]$
T	Eq. 4.22	Auxiliary stress tensor	$[\mathrm{Pa}]$
$\mathcal{T}$	Eq. 4.2	Temperature	$[\mathrm{K}]$
$\mathbf{u}$	Eq. 4.2	Mean particle velocity vector	$[\mathrm{m}\,\mathrm{s}^{-1}]$
U, u	Eq. 2.1	Velocity	$[\mathrm{m}\,\mathrm{s}^{-1}]$
V	Eq. 4.51	Volume	$[\mathrm{m}^3]$
$\mathbf{x}$	Eq. 4.1	Cartesian Eulerian coordinates	$[\mathrm{m}]$
$\mathbf{X}$	Fig. 4.6	Cartesian Lagrangian coordinates	$[\mathrm{m}]$
w	Eq. 4.4	Velocity set weight	$[-]$
W	Fig. 6.14	Separation Distance	$[\mathrm{m}]$

Greek letters

$\dot{\boldsymbol{\gamma}}$	Eq. 2.8	Shear-rate tensor	$[\mathrm{s}^{-1}]$
Γ	Fig. 4.6	Boundary surface	$[-]$
δ	Eq. 4.36	Dirac's delta	$[-]$
ϱ	Eq. 4.38	Discrete Dirac's delta	$[-]$
$\delta_{\alpha\beta}$	Eq. 4.4	Kronecker's delta	$[-]$
ϵ	Eq. 4.58	Expansion parameter / Stiffness collision parameter	$[-] \,/\, [\mathrm{m\,N^{-1}}]$
ζ	Eq. 4.58	Threshold distance for collision	$[\mathrm{m}]$
η	Eq. 4.14	Apparent viscosity	$[\mathrm{m^2\,s^{-1}}]$
Θ	Fig. 4.6	Eulerian domain	$[-]$
λ	Eq. 2.15a	Structural parameter	$[-]$
μ	Eq. 2.1	Dynamic viscosity	$[\mathrm{Pa\,s}]$
ν	Eq. 2.6	Kinematic viscosity	$[\mathrm{m^2\,s^{-1}}]$
ξ	Eq. 4.1	Particle velocity vector	$[\mathrm{m\,s^{-1}}]$
Π	Eq. 4.12	Velocity moment	$[-]$
ρ	Eq. 2.2	Density	$[\mathrm{kg\,m^{-3}}]$
σ	Eq. 2.8	Viscous stress tensor	$[\mathrm{Pa}]$
τ	Eq. 4.3	BGK relaxation time	$[\mathrm{s}]$
ϕ	Eq. 4.38	Distribution kernel	$[-]$
ω	Eq. 4.9	Relaxation frequency	$[\mathrm{s^{-1}}]$
$\boldsymbol{\omega}$	Eq. 4.54	Rotational velocity	$[\mathrm{s^{-1}}]$
Ω	Eq. 4.1	Collision operator	$[\mathrm{kg\,s^{(d-1)}\,m^{-2d}}]$

Non-dimensional groups

Ar	Eq. 2.6	Archimedes number	$[-]$
Bi	Eq. 2.10	Bingham number	$[-]$
De	Eq. 2.13	Deborah Number	$[-]$
He	Eq. 2.11	Hedstrom number	$[-]$
Re	Eq. 2.4	Reynolds number	$[-]$
Tx	Eq. 2.17	Thixotropic number	$[-]$
Wi	Eq. 2.14	Weissenberg Number	$[-]$
Y_G	Eq. 3.1	Yield gravity parameter	$[-]$

Superscripts

$(\,)^{eq}$	Eq. 4.2	Equilibrium
$(\,)^{E}$	Eq. 4.36	Eulerian
$(\,)^{L}$	Eq. 4.36	Lagrangian
$(\,)^{m}$	Eq. 4.47	Iteration
$(\,)^{neq}$	Eq. 4.17	non-Equilibrium
$(\,)^{reg}$	Eq. 4.15	regularized
$(\,)^{t}$	Eq. 4.52	Time-step
$(\,)^{*}$	Eq. 4.10	Post collision populations, non-Dimensional
$(\,)^{+}$	Appx. B	Lattice Unit
$(\,)^{noF}$	Eq. 4.45	Without force term

Subscripts

$(\ )_B$	Fig. 2.2	Buoyancy
$(\ )_D$	Eq. 2.1	Drag, Diameter
$(\ )_{\text{eff}}$	Eq. 6.1	Effective
$(\ )_f$	Eq. 2.2	Fluid
$(\ )_g$	Eq. 4.27	Secondary
$(\ )_i$	Eq. 4.4	Discrete velocity direction
$(\ )_j$	Eq. 4.58	Particle index
$(\ )_p$	Eq. 2.5	Particle, plastic
$(\ )_s$	Eq. 4.4	Sound
$(\ )_t$	Eq. 2.5	Terminal
$(\ )_y$	Tab. 2.2	Yield
$(\ )_w$	Eq. 4.21	Wall
$(\ )_\alpha$	Eq. 4.4	Cartesian direction
$(\ )_\infty$	Tab. 2.3	Infinity shear-rate
$(\ )_0$	Tab. 2.3	Zero (Initial, Shear-rate)

CONTENTS

1 INTRODUCTION

1.1 Context

Petroleum has been one of the principal energy sources for humankind since the 19th century. Its by-products have several applications, from vehicle's fuel to road construction. In most cases, it is necessary to drill the Earth's crust to extract the oil contained in the reservoir rocks (CHILINGAR et al., 2005). In many operations, this is accomplished by using a rotary drilling process, Fig. 1.1.

Figure 1.1 – Schematic representation of drilling fluid flow.
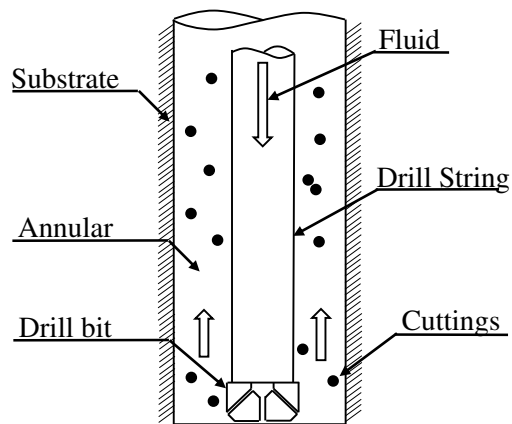
Source: Own elaboration.

In this type of drilling process, a bit rotates while weight is applied in the drill pipe direction. The combination of axial pressure and circular movement breaks the rock in small pieces. A drilling fluid is then continuously pumped through the center of the drill pipe until it reaches the borehole's bottom. There, the fluid removes the cuttings from the bit region and transports them to the surface through the annular region between the rocks and the external surface of the drill pipe. When the cuttings reach the surface, they are separated from the fluid, which returns to the system continuing the cycle.

Other than removing the cuttings from the bit region, the drilling fluid also needs to perform other functionalities while remaining physicochemically stable (EUSTES, 2011):

- Cooling and lubrication of the drilling bit;

- Fluid-loss control;

- Pressure control;

- Transmit power to the drilling bit.

However, due to programmed or unforeseen circumstances, such as increasing the drill pipe length or drill head switch, the drilling operation needs to be halted. When this happens, the cuttings in mid transport will tend to sink, due to the relative density difference to the fluid, and pile up in the bottom

of the borehole assembly (BHA) region. If enough cuttings pile up in the BHA, they will stick the drill pipe and, in severe cases, leading to the loss of the well.

In order to prevent the cuttings from settling is necessary that the fluid buildup a gel-like structure when at rest, but it also needs to exhibit a low viscosity when pumping. Some fluids feature this reversible change between gel-like material in low strain rates and liquid in high strain rates. The phenomenon may be associated with the microstructure change between a highly structured and unstructured condition of the immersed particles present in the fluid. Also, in some fluids, if a minimum shear is not reached, the cuttings will remain suspended, thus preventing their settling. The rheological behavior allows the cuttings to be transported during the regular drilling operation and reduce the settling rate when it is necessary. Being able to predict the rate at which the cuttings pile up at the bottom of the borehole (in case of the circulation interruption) is highly essential since it allows the field engineer to determine the correct time window safe to operate without risk of losing the well.

1.2 Non-Newtonian, Thixotropic and Drilling Fluids

Depending on fluid's composition, they exhibit different rheological behaviors. To study these materials, classes or groups are created to cluster the ones that present similar properties. Chhabra and Richardson (2008) divide the fluids into three groups based on their stress time-response.

The first group, denominated generalized Newtonian fluids (GNF) have time-independent properties, in other words, the shear stress only depends on the instantaneous strain rate. GNFs can be divided into some categories (BIRD et al., 1987): shear-thinning fluids exhibit a decrease in the apparent viscosity with the increase of shear rate. Meanwhile, shear-thickening fluids increase the apparent viscosity as the shear rate increases. Another subgroup of time-independent fluids inside the GNFs is the one where a minimal stress needs to be applied to shear, named yield-stress. The subgroup that encompass this kind of fluid is denominated viscoplastic fluids. Like the previously mentioned time-independent fluids, the viscoplastic fluids can also have the viscosity that changes with the shear rate.

Another class of fluids defined by Chhabra and Richardson (2008) is composed of the ones whose apparent viscosity also dependent on the shear's duration. The class can be further divided into two subgroups: thixotropic or rheopectic fluids. Thixotropic fluids exhibit a decrease in the apparent viscosity as a function of the shear's duration, while rheopectic fluids have the opposite behavior: it increases the apparent viscosity the longer the fluid is under shear (CHHABRA and RICHARDSON, 2008). An accepted definition of thixotropic fluid is given by Mewis as: "The continuous decrease of viscosity with time when a flow is applied to a sample that has been previously at rest and the subsequent recovery of viscosity in time when the flow is discontinued." (MEWIS and WAGNER, 2009, p. 215)[1]. The thixotropic effect can be explained as the process of microstructure breakdown, of the immersed particles present in the fluid, caused by the shear and the microstructure build-up back to the previous state, when at rest, occasioned by the Brownian motion of these particles (BARNES, 1997). These states are represented in Fig. 1.2:

On the left side, the fluid sample was let to age for a long period. Due to the Brownian motion, a microstructure will be formed. If shear is applied over time, the microstructure connections will start to

---

[1]   Reprinted from Advances in Colloid and Interface Science, Vol 147, Jan Mewis, Norman J. Wagner, Thixotropy, 214-227,2009, with permission from Elsevier

Figure 1.2 – Schematic representation of the thixotropic structure in a a) structured and b)unstructured state.

a) Structured   b) Unstructured
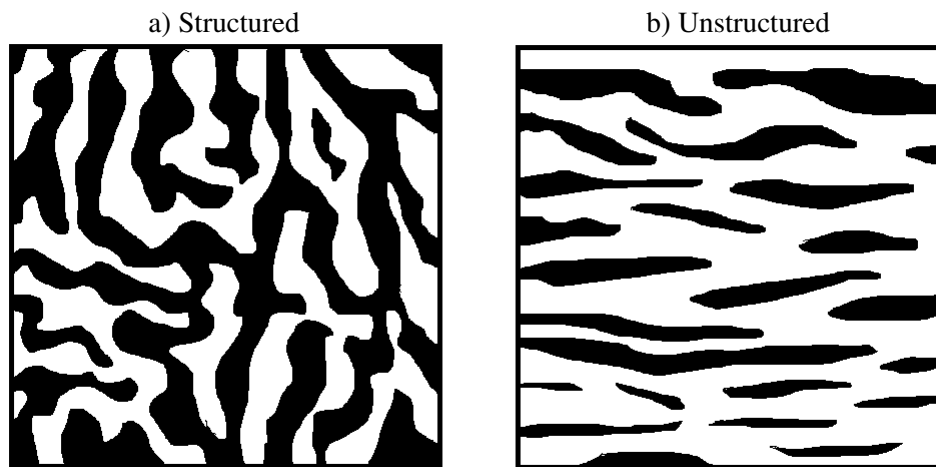
Source: Own elaboration

collapse, represented on the right side, and the material will start to flow. If the shear is then removed, the immersed particles will start to structure again and return to the previous state. The rheological behaviors previously mentioned are not strict; this means that some fluids can exhibit properties from one or more groups, e.g. plasticity and elasticity at same time. The overlapping often depends on time and force scale. These fluids are usually denominated as thixo-elasto-visco-plastic fluids (EWOLDT and MCKINLEY, 2017). Drilling fluids are not an exception to this. They can present the properties of one or more of the behaviors cited above. This work will be focusing on the drilling fluids that exhibit thixotropic effects allied with yield-stress, in other words, the elastic behavior that may exist will be excluded from the analysis.

1.3 Problem Statement

The problem under consideration is the particle settling in the annular region between the drill pipe and the borehole walls after the drilling fluid flow shut down, as represented in previously in Fig. 1.1. Initially, the drilling fluid is pumped inside the drill string until it leaves through the drill bit. In this region, the fluid removes the cuttings and transports them through the annular region between the drill string and the substrate. When the drilling fluid stops being pumped, the cuttings begin to sink and start to settle.

In order to gain a basic understanding of the phenomenon, the analysis will consider a simplified version settling in the borehole region. The problem will be composed of two spherical particles immersed in a thixo-viscoplastic quiescent fluid. The particles will be released from rest, in a rectangular prism domain, and settle due to the gravitational force until the movement stops, either by hitting the domain floor or by the fluid gelification. A visual representation of the simplified problem described above is shown in Fig. 1.3.

Figure 1.3 – Geometry of the simplified problem of two particles settling in drilling fluid.
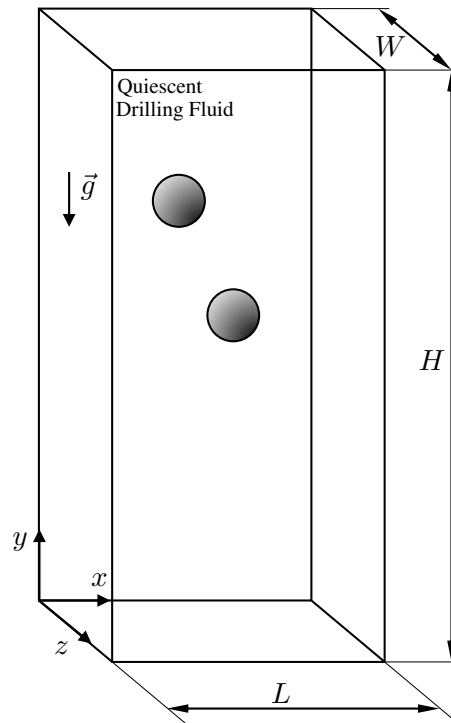
Source: Own elaboration.

1.4 Kinetic Theory

The lattice Boltzmann method (LBM) is a numerical method that approaches the fluid flow solution in the mesoscopic scale, where conventional CFD solvers based on finite element methods (FEM) or finite volume method (FVM) solve the fluid flow in the macroscopic scale. At the microscopic scale, the fluid dynamic is analyzed through Newton's second law and intermolecular forces have a significant role. On the mesoscopic scale, the molecules are grouped and Boltzmann kinetic theory is applied. Meanwhile, in the macroscopic scale, the fluid flow parameters are resolved, ignoring possible molecular interactions, the mass and momentum transport equations represent the fluid behavior (GUO and SHU, 2013).

On the mesoscopic scale, a group of atoms/molecules/particles are clustered. Over time these mesoscopic clusters, often called populations, will collide with another group and will change its momentum. The particle distribution function then represents the probability of the particles to be in a given velocity state.

1.4.1 Why LBM?

In the last years, an increasing interest in using the lattice Boltzmann method (LBM) to solve the Navier-Stokes equations arose. This change in perception could be attributed to how High-Performance Computing (HPC) changed in the last 15 years. At the beginning of the century, the computational performance was closely related to the operational frequency of the central processing unit (CPU). But because of thermal constraints, the maximum CPU frequency has been slowly increasing since 2005

(MOORE, 2011).

In order to increase the processing speed, the focus changed from higher frequencies to a higher number of cores in a single CPU. This allowed the increase of processing power in CPUs to continue, as long the application is capable of running in multiple cores. Alongside the CPUs, graphical processing units (GPU) also started to increase the number of cores. One difference from CPUs to GPUs is the architecture design focused on multiple cores instead, currently with two times the order of magnitude higher but lower operating frequencies. This high number of cores allows several processes to be executed at the same time. In the LBM the operations are local, which allows the calculations to be spread in multiple cores, and consequently take advantage of the shift to multi-core architectures of the last decade.

1.5 General Objective

In this work is developed a mathematical and numerical method based on LBM coupled with the immersed boundary method (IBM) for the representation of two particles settling in a thixotropic fluid. The method will allow comprehend the settling phenomenon of spherical particles and determine the effects of fluid properties, yield stress, and thixotropic parameters in such a system. Also, the results will be used to construct a numerical correlation for the terminal velocity of a single settling sphere, which could be used by field engineers in the decision-making process when restarting a drilling operation, potentially avoiding the loss of the well.

Due to the complex interactions between immersed particles and non-Newtonian fluids expected on this work, the application was written in CUDA®/C++, an application programming interface (API) from NVIDIA® for GPUs. The implementation of the computational code follows several methodologies for memory transfer (MAWSON and REVELL, 2014), memory layout (JANUSZEWSKI and KOSTUR, 2014), and parallelization strategy (VALERO-LARA et al., 2015) which are combine (OLIVEIRA et al., 2019) to accomplish a high degree of efficiency in memory arrangement and processing speed [2]. Several substeps were performed to execute this study: First, a computational application capable of solving three-dimensional non-Newtonian models (Power-Law, Bingham) fluid flows, utilizing the lattice Boltzmann method was created. Next, the Immersed Boundary method was coupled to solve the settling problem. Finally, a numerical model that considers some of the thixotropic behaviors of the drilling fluid was added.

1.6 Document Outline

The dissertation is organized into seven chapters as follows: Chapter 2 describes the fundamentals regarding non-Newtonian fluids and settling of immersed particles in Newtonian fluids. Chapter 3 exposes the literature review about particle settling in Newtonian and non-Newtonian fluids. Chapter 4 presents the mathematical and numerical method utilized to model and solve the settling behavior of the spheres. Validations cases are presented in chapter 5 for both non-Newtonian fluids and particle settling. Chapter 6 presents the results and discussions about the settling of two spherical particles in a thixotropic fluid. The final remarks related to the study and suggestions for future works are shown in Chapter 7.

---

[2] An open-source version can currently be found in https://github.com/CERNN/

2 THEORETICAL FOUNDATION

In this chapter, the basis regarding the flow patterns behind a sphere and single-particle settling behavior in Newtonian fluids are introduced. It also presents the fundamentals of non-Newtonian fluids and its essential properties, with emphasis on mathematical modeling.

2.1 Flow over a Static Sphere

The foundation for the particle settling can be based on the flow around a static sphere. Taneda (1956) executed an experimental study on the wake formation for Reynolds numbers between 5 and 300. In his experiment, it was obtained the Reynolds number for when the wake vortex ring is established (Re = 25), as well as when the vortex begins to oscillate (Re = 130). Sakamoto and Haniu (1990) extended experimental study for the flow around a sphere, with Reynolds numbers between 130 and 4000. For Reynolds numbers under 130, there is no detached wake pattern, as shown by Taneda (1956) and Sakamoto and Haniu (1990). Increasing the Reynolds numbers between 130 and 300, an oscillatory movement surges. When the Reynolds numbers surpass 300, hairpin-shaped vortices start to form in a stable axial position (ACHENBACH, 1974). The wake pattern then begins to rotate along the axis when it reaches Reynolds numbers superior to 420. Finally, for Reynolds numbers over 800, a vortex instability and breakdown begin to be observed.

When a fluid flow passes over an immersed object, a drag force will emerge due to pressure differences and friction. Stokes (1850) proposed an analytical solution for the drag force in spherical particle immersed in a fluid at low Reynolds number, later named as Stokes' drag (CHHABRA, 2006):

$$\boldsymbol{F_D} = -3\pi\mu D\boldsymbol{U} \tag{2.1}$$

where μ is the dynamic viscosity, D is the sphere diameter, and U is the relative velocity between the particle and the fluid. The drag force is generally defined as:

$$F_D = -\rho_f \frac{U^2}{2} C_D A \tag{2.2}$$

where A the cross-section area of the particle relative to the flow direction, ρ_f is the fluid density and C_D is the drag coefficient. Combining the Eq. 2.2 with the Eq. 2.1, the drag coefficient for a sphere in creeping flow is:

$$C_D = 24/\mathrm{Re_D} \tag{2.3}$$

where $\mathrm{Re_D}$ is the Reynolds number defined as :

$$\mathrm{Re_D} = \frac{\rho_f U D}{\mu} \tag{2.4}$$

The Stokes' solution agrees with experimental data obtained for Reynolds numbers under 0.1. Meanwhile, for Reynolds numbers over 0.1, the drag coefficient starts to diverge from the analytical solution, mainly because the inertial terms of the Navier-Stokes equations cannot be disregarded. Due to that, the drag coefficient for Reynolds number higher than 0.1 have been collected over the years and consequently allowing the construction of correlations which are later used by engineers. Figure 2.1 presents the drag coefficient as a function of the Reynolds number based on one of these correlations.

Figure 2.1 – Drag coefficient of a smooth sphere as a function of Reynolds number using the correlation proposed by Morrison (2013).
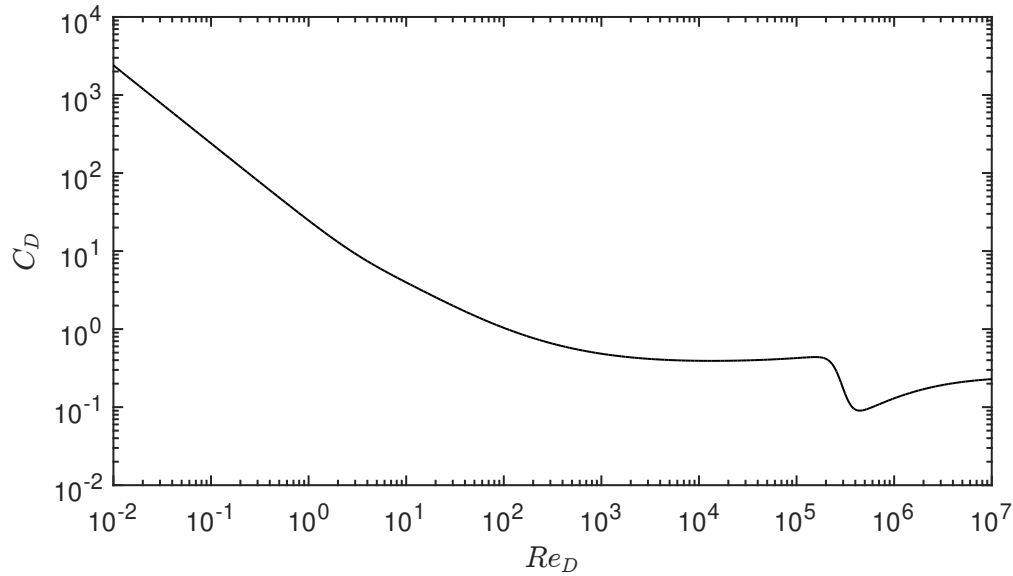
Source: Own elaboration.

For higher Reynolds numbers than the creeping flow regime, the adverse pressure gradient over the sphere surface causes the detachment of the laminar boundary layer and consequently create vortices behind the sphere, reducing the drag coefficient. As the Reynolds number increases $\left(\mathrm{Re_D} \gtrsim 3 \times 10^5\right)$ the boundary layer over the sphere transition from laminar to turbulent (SCHLICHTING, 1979) and causes a drop in the drag coefficient.

2.2 Particle Settling

A body immersed in a fluid under the action of a gravitational force is subject to Archimedes' principle. If the buoyant force is larger than the gravitational force, the body will rise until it reaches the fluid surface. On the contrary, if the gravitational force is stronger than the buoyancy force, the particle will sink. According to Newton's second law of motion, the body will accelerate in both conditions unless an equilibrium between the forces acting in the body occurs. When the body reaches a certain velocity, the forces acting up in the body (drag, buoyancy, and gravitational) will reach that equilibrium state and the particle will not accelerate, which is known as terminal velocity. Figure 2.2 represents the free body diagram of the forces in acting in a sphere settling in a fluid.

In the creeping flow regime ($\mathrm{Re_D} < 0.1$), the force balance using the Stokes' solution for the drag force, Eq. 2.1, and Newton's second law of motion can be used for derivation of the terminal velocity (DAVIS and ACRIVOS, 1985):

$$U_t = \frac{1}{18}\frac{(\rho_p - \rho_f)}{\mu}gD^2 \tag{2.5}$$

combining the Eq. 2.5 and Eq. 2.4, the terminal Reynolds number ($\mathrm{Re_t}$) in creeping flow is:

$$\mathrm{Re_t} = \frac{gD^3}{18\nu^2}\left(\frac{\rho_p}{\rho_f} - 1\right) = \frac{\mathrm{Ar}}{24} \tag{2.6}$$

Figure 2.2 – Force balance in sphere particle settling in creeping flow.
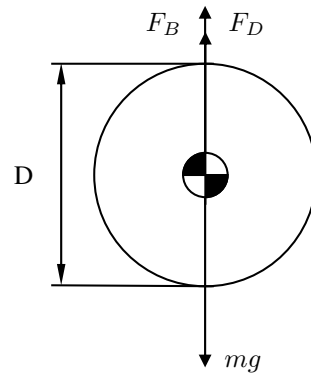
Source: Own elaboration.

where Ar is Archimedes number for a Newtonian fluid, commonly encounter in the literature regarding particle settling, which will represent the ratio between the difference of the gravitational and buoyant forces versus the viscous forces acting in an immersed particle and it is defined as (CHHABRA, 2006):

$$\text{Ar} = \frac{4}{3} \left[\frac{gD^3 \rho_f \left(\rho_p - \rho_f \right)}{\mu^2} \right] \tag{2.7}$$

When the Reynolds number increase, the different vortex shedding patterns change the forces acting in the settling particle, affecting its trajectory. In this case, there are two main force directions: one parallel to the gravity field and another perpendicular. The first is linked to the drag coefficient and, consequently, on the Reynolds number, as previously mentioned, and determine the speed at which the particle settles. The analytical solution for the transient behavior from a static position to settling velocity in low Reynolds numbers in Newtonian was studied by Bromwich (1929). But for flows outside the creeping flow, there is no knowledge of an analytical solution, and hence experimental evaluations were carried. Table 2.1, compiled by Cliff et al. (2005), shows some of the correlations created, which can be used to determine the drag coefficient and, consequently, the terminal velocity.

Meanwhile, the lateral trajectory of the particle depends on the lift coefficient. Through experiments, Horowitz and Williamson (2010) analyzed the settling regimes of spherical particles for Reynolds numbers between 100 and 15 000 and different density ratios. For Reynolds numbers below 260, the particles settle with a linear trajectory and may exhibit some minimal oscillation. For rising spheres, density ratio less than unity, with a Reynolds number over 260 and density ratio less than critical, the particle will perform a zigzag pattern. For densities ratio above this critical value, which depends on the Reynolds number, the particle trajectory in a sense, agrees with the wake patterns of static spheres, independent of the density ratio of fluid and particle. These lateral movements will cause some increase in the drag coefficient when compared with data of a fixed sphere in a wind tunnel, and thus it cannot be ignored.

Table 2.1 – Recommended drag coefficient correlations

Reynolds Range	Drag Coefficient (C_D)
$Re_D < 0.01$	$C_D = \frac{24}{Re_D}\left(1 + \frac{3}{16}Re_D\right)$
$0.01 < Re_D < 20$	$C_D = \frac{24}{Re_D}\left[1 + 0.1315Re_D^{(0.82-0.05w)}\right]$
$20 < Re_D < 260$	$C_D = \frac{24}{Re_D}\left[(1 + 0.1935Re_D^{-0.06305})\right]$
$260 < Re_D < 1500$	$\log C_D = 1.6435 - 1.1242w + w^2$
$1500 < Re_D < 1.2 \times 10^4$	$\log C_D = -2.4571 + 2.558w - 0.9295w^2 + 0.1049w^3$
$1.2 \times 10^4 < Re_D < 4.4 \times 10^4$	$\log C_D = -1.9181 + 0.637w - 0.0636w^2$
$4.4 \times 10^4 < Re_D < 3.38 \times 10^5$	$\log C_D = -4.339 + 1.5809w - 0.1546w^2$
$3.38 \times 10^5 < Re_D < 4 \times 10^5$	$C_D = 29.78 - 5.3w$
$4 \times 10^5 < Re_D < 10^6$	$C_D = 0.1w - 0.49$
$10^6 < Re_D$	$C_D = 0.19 - \left(\frac{8 \times 10^4}{Re_D}\right)$

where: $w = \log Re_D$

Source: Used with permission of Dover Publications Inc, from Bubbles, Drops, and Particles, Clift, R., Grace, J. R., Weber, M. E., 2005; permission conveyed through Copyright Clearance Center, Inc

2.3 Non-Newtonian Fluids Models

Newton's law of viscosity defines the linear relationship between the viscous stress tensor and the strain rate tensor, for what came to be known as a Newtonian fluid (BIRD et al., 1987):

$$\boldsymbol{\sigma} = \mu\dot{\boldsymbol{\gamma}} \tag{2.8}$$

where $\boldsymbol{\sigma}$ is the viscous stress tensor, $\dot{\boldsymbol{\gamma}}$ is the strain-rate tensor and μ is the scalar dynamic viscosity of the fluid. Non-Newtonian fluids are the ones which do not obey Newton's viscosity law. The viscosity of these fluids depends on several factors. One of them is the magnitude of the strain rate tensor ($\dot{\gamma}$). In incompressible and shear flows, $\dot{\gamma}$ reduces to be only a function of the strain-rate tensor magnitude (BIRD et al., 1987):

$$|\dot{\gamma}| = \sqrt{\frac{1}{2}\sum_i\sum_j \dot{\gamma}_{ij}\dot{\gamma}_{ji}} \tag{2.9}$$

where $\dot{\gamma}_{ij}$ are the components of the strain rate tensor. Constitutive equations have been proposed for the apparent viscosity (η) over the years to accommodate the different fluid behaviors. For generalized Newtonian fluids, one can cite Power-Law, Bingham, and Herschel-Bulkley models, represented in Table 2.2. The Power-Law model represents a fluid with shear-thinning or shear-thickening behavior depending on the value of the power-law index n. Meanwhile, the Bingham and Herschel-Bulkley model represent a viscoplastic fluid with a yield stress value (σ_y). Two dimensionless numbers are typically associated with the analysis of viscoplastic fluids flows. The Bingham number correlates the ratio of yield stress and viscous stress (HUILGOL, 2015):

$$Bn = \frac{\sigma_y}{\mu}\frac{L}{U} \tag{2.10}$$

where L is the characteristic length, μ is the viscosity and U is the fluid velocity. Another important non-dimensional group relevant to viscoplastic fluids is the Hedström number, which was initially defined on the work of Hedström (1952), where the friction factor for cement suspensions was correlated as a

Table 2.2 – Generalized Newtonian fluid constitutive equations (BIRD et al., 1987)

Model	Equation
Power-Law	$\eta(\dot{\gamma}) = K\|\dot{\gamma}\|^{n-1}$
Bingham	$\eta(\dot{\gamma}) = \begin{cases} \infty & , \|\boldsymbol{\sigma}\| \leq \sigma_y \\ \mu_p + \sigma_y/\|\dot{\gamma}\| & , \|\boldsymbol{\sigma}\| > \sigma_y \end{cases}$
Herschel-Bulkley	$\eta(\dot{\gamma}) = \begin{cases} \infty & , \|\boldsymbol{\sigma}\| \leq \sigma_y \\ K\|\dot{\gamma}\|^{n-1} + \sigma_y/\|\dot{\gamma}\| & , \|\boldsymbol{\sigma}\| > \sigma_y \end{cases}$

Source: Own elaboration.

function of Reynolds number. Both these dimensionless numbers help correlate similar flow patterns and friction for viscoplastic fluids.

$$\text{He} = \frac{\rho_f L^2 \sigma_y}{\mu^2} = \text{ReBn} \tag{2.11}$$

Figure 2.3 shows the rheological behavior of the previous models for time-independent fluids, where the shear-thinning fluids reduce the apparent viscosity with increasing shear rate, meanwhile the shear-thickening fluids increase. For viscoplastic fluids, there is a minimum necessary stress for flow to occur.

Figure 2.3 – Apparent viscosity as a function of shear strain rate for some time-independent fluid models.
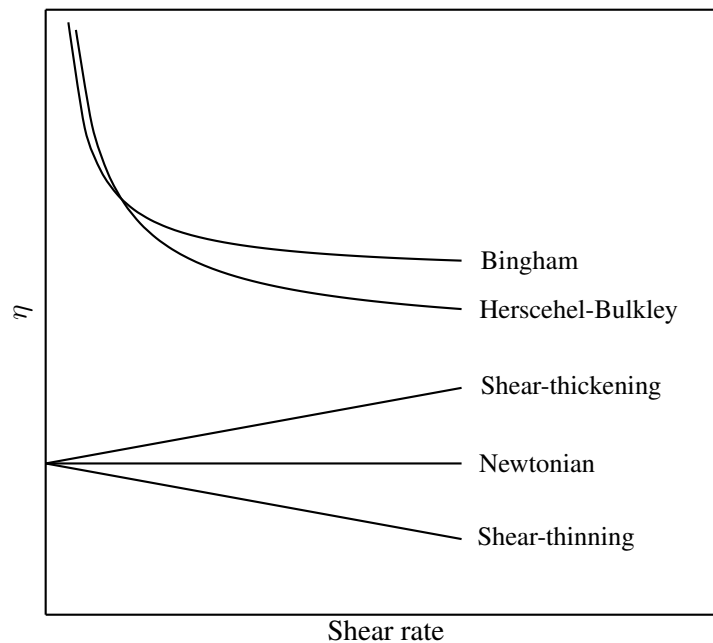
Source: Own elaboration.

Another group of fluids, defined by Chhabra and Richardson (2008), exhibits a Hookean solid property at a low strain rate: elasticity. The elasticity of the fluids allows them to return to the original state of deformation when the stress is removed, like solids in the elastic regime. Because of the nature of elastic and viscous properties, these fluids are denominated viscoelastic. James Clerk-Maxwell (1867

apud BIRD et al., 1987) correlated both effects, elastic and viscous, in only one equation. Other models emerged later, like Jeffrey's model. These models can be written in integral form denominated the General Linear Viscoelastic Model (GLVM) (BIRD et al., 1987):

$$\boldsymbol{\sigma} = \int_{-\infty}^{t} M\left(t - t'\right) \boldsymbol{\gamma}\left(t, t'\right) dt' \tag{2.12}$$

where $M\left(t - t'\right)$ is the memory function that stores the time-dependent behavior of the fluid, and it depends on the model utilized, γ is the shear function of the previous time. Since the memory function continually decreases to zero as the time between past events (t') and the current time (t) increase, the effects of previous stress fade over time. Flows with viscoelastic fluids can be described by Weissenberg and Deborah numbers (POOLE, 2012):

$$\mathrm{De} = \frac{t_c}{T} \tag{2.13}$$

$$\mathrm{Wi} = \frac{t_c U}{L} \tag{2.14}$$

where U is the flow velocity, L is the characteristic length, T is the duration of the observation and t_c is characteristic time that is related to the fluid relaxation times. The Deborah number correlates the material response time to the observation time. Low Deborah numbers indicate that the material will behave like a fluid, while for high Deborah numbers, the material will behave like a solid with elastic properties. The Weissenberg number is the ratio of elastic and viscous forces.

2.3.1 Fundamentals of Thixotropic Fluids

As mentioned earlier, thixotropic fluids present a nature that depends on the shear duration. In order to accommodate this behavior and understand it better, researchers created constitutive equations to model it. These constitutive equations can be divided into two approaches: phenomenological or microstructural (BARNES, 1997). In the phenomenological approach, the constitutive equations are formulated to fit the experimental data of material response with time and shear rate. Microstructural approaches formulate constitutive equations based on physical phenomena. It can be divided into direct and indirect microstructural models. Direct models are based on the actual physics in the fluid and immersed particle structures responsible for the buildup and breakdown. Indirect models are formulated based on a numerical structural parameter, λ. The structural parameter then represents how bounded the polymeric structure is. It can assume values between 0, for fluid without connections Fig. 1.2.b, and 1, for fluid with particles fully interconnected Fig. 1.2.a. The general constitutive form is given by (MEWIS and WAGNER, 2009):

$$\boldsymbol{\sigma} = f_1\left[\lambda\left(t\right), \Pi_{\dot{\gamma}}\left(t\right)\right] \tag{2.15a}$$

$$\frac{d\lambda\left(t\right)}{dt} = f_2\left[\lambda\left(t\right), \Pi_{\dot{\gamma}}\left(t\right)\right] \tag{2.15b}$$

where $\Pi_{\dot{\gamma}}$ is a function of the flow condition and λ is the structural parameter.

Mewis and Wagner (2009) list mechanisms that affect λ: Particle attraction, thermal and convective motion can operate to build up the fluid-structure. Meanwhile, the flow shear and even the thermal motion can act to breakdown the structure. Typically, indirect microstructural models only consider the Brownian motion as an aging factor and the shear rate as the responsible term for the structure

breakdown. Mewis and Wagner (2009) on their review, compiled a table for some of the structural thixotropic models, for the function f_1 is listed on Table 2.3 while f_2 is on Table 2.4. In the kinetic

Table 2.3 – Constitutive equations for thixotropic fluids in the form $\sigma = \sigma_y(\lambda) + \eta_\lambda(\lambda, \dot{\gamma})\dot{\gamma}$

Author(s)	$\sigma_y(\lambda)$	$\eta_\lambda(\lambda, \dot{\gamma})$
Moore (1959)	–	$\lambda\eta_0$
Worrall and Tuliani (1964)	$\sigma_{y,0}$	$\lambda\eta_0$
Houska (1981)	$\lambda(\sigma_{y,0} - \sigma_{y,\infty}) + \sigma_{y,\infty}$	$\lambda K_0 \dot{\gamma}^{n-1}$
Toorman (1997)	$\lambda\sigma_{y,0}$	$\lambda\eta_0$
Mujumdar et al. (2002)	$\lambda^{a+1} G_0 \gamma_c^a$	$-\lambda K_0 \dot{\gamma}^{n-1}$
Coussot et al. (2002)	–	$\lambda^a \eta_\infty$
Dullaert and Mewis (2006)	$\lambda G_0 \gamma_c (\lambda\dot{\gamma})^a$	$\lambda\eta_0$

Source: Reprinted from Advances in Colloid and Interface Science, Vol 147, Jan Mewis, Norman J. Wagner, Thixotropy, 214-227,2009, with permission from Elsevier.

Table 2.4 – Kinetic equations for thixotropic fluids in the form $d\lambda(t)/dt = -f_{break} + f_{build}$

Author(s)	f_{break}	f_{build}
Moore (1959)	$k_1 \dot{\gamma}\lambda$	$k_2(\lambda_0 - \lambda)$
Worrall and Tuliani (1964)	k_1	–
Houska (1981)	$k_1 \lambda \dot{\gamma}^m$	$k_2(1 - \lambda)$
Toorman (1997)	$k_1 \lambda^a \dot{\gamma}$	$k_2(1 - \lambda)^b$
Mujumdar et al. (2002)	$k_1 \lambda \dot{\gamma}$	$k_2(1 - \lambda)$
Coussot et al. (2002)	$k_1 \dot{\gamma}\lambda$	k_2
Dullaert and Mewis (2006)	$k_1 \dot{\gamma}\lambda t^{-\beta}$	$k_2(1 - \lambda)t^{-\beta} + k_3 \dot{\gamma}^{0.5}(1 - \lambda)t^{-\beta}$

Source: Reprinted from Advances in Colloid and Interface Science, Vol 147, Jan Mewis, Norman J. Wagner, Thixotropy, 214-227,2009, with permission from Elsevier.

equation for the structural parameter, f_{break} represents the rate at which the structural parameter breaks due to the local shear rate and f_{build} model the aging process of the fluid.

Moore (1959) and Coussot et al. (2002) constitutive equations do not include yield stress, Worrall and Tuliani (1964) has constant yield stress, while the other models the value of the yield stress depends on the structural parameter. The apparent viscosity is then based on the product between the structural parameter λ and the viscosity at zero shear rate η_0. Coussot et al. (2002) adopted the viscosity at a high shear rate as a base. Houska (1981) and Mujumdar et al. (2002) added shear-thinning effects to it.

The current work was used a simplified version of the Houska (1981) model, where only the yield stress is dependent on the structural parameter, with plastic viscosity remaining constant. The shear-rate exponents were kept constant and equal to a unit. Finally, the kinetic equation is modified to support the

transport of the structural parameter for an incompressible fluid:

$$\boldsymbol{\sigma} = \eta(\dot{\gamma}, \lambda)\dot{\boldsymbol{\gamma}}, \tag{2.16a}$$

$$\eta(\dot{\gamma}, \lambda) = \begin{cases} \infty & , |\boldsymbol{\sigma}| \leq \sigma_y \\ \eta_p + \sigma_y|\dot{\gamma}| & , |\boldsymbol{\sigma}| > \sigma_y \end{cases} \tag{2.16b}$$

$$\sigma_y = \lambda\sigma_{y,0} + (1 - \lambda)\,\sigma_{y,\infty} \tag{2.16c}$$

$$\frac{\partial \lambda}{\partial t} + u_i\frac{\partial \lambda}{\partial x_i} = -k_1\lambda|\dot{\gamma}| + k_2(1 - \lambda), \tag{2.16d}$$

where η_p is the plastic viscosity, $\sigma_{y,0}$ and $\sigma_{y,\infty}$ the static and dynamic yield stress, k_1 is the breakdown parameter, and k_2 is the build-up parameter. For the chosen fluid model, an important dimensionless parameter is the Thixotropic number, which represents the ratio between the breakdown and build-up rates:

$$\mathrm{Tx} = \frac{k_1}{k_2}\frac{U}{L} \tag{2.17}$$

Chapter Summary

In this chapter, the foundation for the particle settling phenomena was presented. Details about the vortex shedding in a sphere as a function of the Reynolds number are presented. Next, the basic theory for modeling non-Newtonian fluid was shown. In the next chapter, a literature review about the settling behavior of spheres in non-Newtonian fluids will be presented.

3 LITERATURE REVIEW

In this chapter introduces a review of previous works regarding the settling behavior of one or two particles in Newtonian and non-Newtonian fluids. It is also shown the methods developed to solve the boundary conditions that arise when trying to model immersed bodies using the lattice Boltzmann method.

3.1 Particle settling in non-Newtonian fluids

Non-Newtonian fluids exhibit different behaviors when compared with Newtonian fluids, so it is expected that the particle settling phenomenon to change. The creeping flow around a sphere create regions with different shear rates. Consequently, the apparent viscosity will be a function of the surface distance and angle from the particle's axis (REYNOLDS and JONES, 1989). Reynolds and Jones (1989) characterized four different settling behaviors in shear-thinning fluids. For tiny Reynolds numbers the fluid behaves like a Newtonian-fluid, followed by a transition zone connecting to the power-law region as the Reynolds number increases. On the power-law region, the particle settling velocity depends on the power-law index. In the last region, where $Re_D > 0.1$, the convective effects start to act in the particle. Numerical models were also used to study the particle settling in power-law fluids, such as the work of Nardi and Franco (2018), which implemented an IB–LBM solution to analyze the effect of the power-law index in the settling behavior of a two-dimensional particle.

Viscoplastic fluids need minimum stress to start shear, creating regions around the particle with an unyielded fluid (WHITMORE and BOARDMAN, 1962). Ansley and Smith (1967) obtained experimental results in tomato sauce and proposed the shape of the unyielded region using the slip-line field theory. The shape obtained by them was the external surface of a spindle toroid with the particle in its center. Beaulne and Mitsoulis (1997) executed numerical simulations with the Finite Element Method for Herschel-Bulkley fluids and compared with the experimental results of the unsheared region data from Atapattu et al. (1995), reproduced in Fig. 3.1, showing the spindle toroidal form.

Due to minimal stress for fluid flow to occur, some situations where a particle left to settle in an unyielded fluid will not move, because not enough stress is exerted by the particle weight. Tabuteau et al. (2007) define the yield number for a sphere in a viscoplastic fluid as:

$$Y_G = \frac{3\sigma_y}{gD\left(\rho_p - \rho_f\right)} \tag{3.1}$$

where τ_y is the yield stress, g is the gravity acceleration, D is the particle diameter and $\rho_p - \rho_f$ is the density difference between the particle and the fluid. The yield number correlates the stress necessary to start the fluid motion and the force applied by the particle. Blackery and Mitsoulis (1997) and Beris et al. (1985) obtained the breakpoint value of 0.143, through the finite-element method, on which values inferior to that the particle starts to move. Meanwhile, Tabuteau et al. (2007) obtained the value of 0.145 through experimental data with Carbopol gels, showing an agreement between experimental and numerical results. Several factors can influence this value such as fluid elasticity (FRAGGEDAKIS et al., 2016), particle shape (PUTZ and FRIGAARD, 2010)(FRIGAARD et al., 2017), and wall effects (BEAULNE and MITSOULIS, 1997)(MITSOULIS, 2004).

Figure 3.1 – Comparison between numerical results and the experiments by Atapattu et al. (1995) for Bi = 1.285.
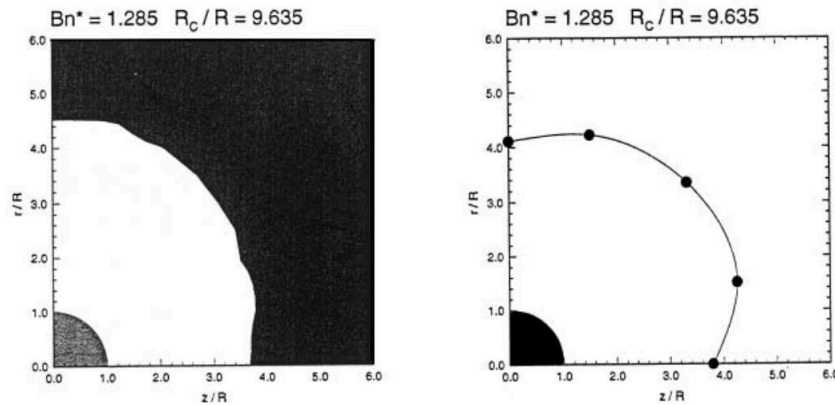
Source: Reprinted from Journal of Non-Newtonian Fluid Mechanics, Vol 72 Issue 1, M. Beaulne and E Mitsoulis, Creeping motion of a sphere in tubes filled with Herschel–Bulkley fluids, 55-71,55-71, with permission from Elsevier

Ferroir et al. (2004) performed experiments of a settling iron sphere in a mixture of water and Laponite, a thixotropic fluid. They obtained results for the particle velocity and travel distance as a function of the fluid aging time and the influence of the frequency when the fluid is mechanically agitated. It was observed that depending on fluid aging levels, the particle would either reach terminal velocity or slow down and stop. A mathematical model was formulated and validated with experimental results to predict the settling behavior as a function of the particle's terminal velocity in an unstructured fluid; their results are reproduced in Fig. 3.2. Their result was in a function of W, which is similar to

Figure 3.2 – Predictions of the Ferroir et al. (2004) mathematical model for the motion of a sphere through a thixotropic paste under the action of a force of different levels (from top to bottom: $(\rho_p - \rho_f)\, gD^2/18\eta_0 = 0.60; 0.59; 0.58; 0.575; 0.57; 0.568; 0.565; 0.56; 0.55$).
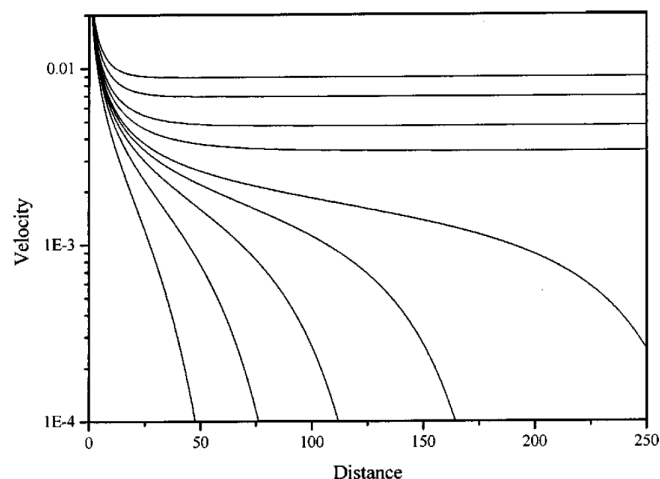
Source: Reprinted from Physics of Fluids, Vol 16 Issue 3, Ferroir, T., Huynh, H. T., Chateau, X., Coussot, P., Motion of a solid object through a pasty (thixotropic) fluid, 594-601, with permission from AIP Publishing

the inverse of yield parameter for viscoplastic fluids. If its value is below a certain critical point, the build-up of the fluid-structure will be faster than the breakdown created by the sphere settling, which will cause an increase in the apparent viscosity and consequently reduce the particle velocity. Otherwise,

the breakdown and build-up process will reach an equilibrium, and the particle will attain a terminal velocity.

Other studies were conducted with thixotropic fluids, such as in Gueslin et al. (2009) where experiments in laponite suspensions observed an exponential decrease in the terminal velocity of the particle as a function of the aging time. Gumulya et al. (2014) analyzed the effects of Deborah number in the structural parameter field as well as in the drag coefficient, through Volume-of-Fluid numerical method. Fluids with a higher relaxation time had an increase in the drag coefficient while fluids with lower relaxation times had a reduced drag associated with the shearing regions being close to the sphere at high relaxation times. A reduced apparent viscosity was observed in the region where a settling sphere had passed. The effect of the breakdown and build-up parameters in flow past a cylinder was investigated through the finite element method in the work of Syrakos et al. (2015). The breakdown rate was observed to be higher in the boundary layer, while unyielded zones were observed behind the cylinder. Finally, an elasto-viscoplastic thixotropic fluid was studied with the finite element method in the work of Fonseca et al. (2013), where the thixotropic model of Souza Mendes (2009) was utilized. It was observed an increase in the drag around a sphere as the thixotropic number increases.

3.1.1 Two-Particle Settling

When two or more particles settle together, interactions between them are bound to happen. Fortes et al. (1987) analyzed the fluidization of two-dimensional beds composed of spherical particles in a Newtonian fluid. In their work is explained the primary mechanism of how two particles interact with each other when settling together.

Initially, when two particles are settling together in a vertical alignment and separated by initial distance, the upper one begins to approach the other, denominated "Drafting". Because of the existence of a relative velocity between the particles, a collision will occur. The collision stage is then denominated "Kissing". Due to instabilities generated in the collision, the top particle will tumble over and both particles stay side by side. The complete phenomenon is often called "Drafting-Kissing-Tumbling" (DKT) and it is represented in Fig. 3.3, where it also shows the relative distance between the particles over time. When the particles are side by side, it creates a non-symmetric wake that, depending on the conditions, can make the particles being vertically aligned again and consequently restarting the DKT process.

Riddle et al. (1977) carried out experiments of two vertically aligned spheres in a shear-thinning fluids. They found that exists a minimum distance for the DKT process to occur. For Generalized Newtonian fluids, Sulaymon et al. (2013) conducted experiments with fluids that can be approximated by the power-law model. In their study, the critical distance on which two settling spheres will interact was analyzed. With a vertical alignment, the collision occurred if the initial distance is less than five diameters. Meanwhile, for horizontal alignment, if the distance is less than two diameters, the collision would occur. For distances between two and five diameters, it was observed a decrease in the separation distance but no collision, while for higher separation distance, no interaction would happen.

Liu et al. (2003) conducted one of the first numerical studies for two particles settling in a Bingham fluid, it utilized the finite element method to obtain the yielded regions. With the separation distance kept constant it was observed a union of the yielded zones that exist around each particle. The arising of this

Figure 3.3 – Drafting-kissing-tumbling process.
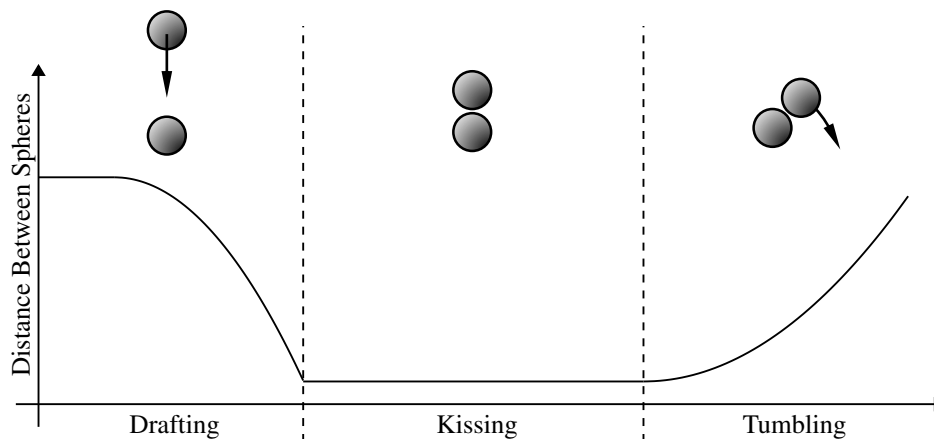
Source: Own elaboration.

connection would depend on the Bingham number as well as the distance between the particles

Prashant and Derksen (2011) analyzed the separation distance in the settling of two spheres in Bingham fluid using the lattice Boltzmann method, with Reynolds numbers of 1 and 6.2, and Bingham number of 0.36 inside a rectangular channel. For the Reynolds number equal to 1, both spheres settle with the same terminal velocity independently of the initial gap between them, meaning that the DKT process was not observed. When the distance between the spheres increased, the terminal velocity also raised, approaching the single sphere terminal velocity for large gaps. When the Reynolds number raised to 6.2 and the initial distance between the particles was two diameters it was observed a collision between the particles.

Pan and Glowinski (2018) used a distributed Lagrange multiplier based fictitious domain method to study the behavior of two and three spheres horizontally aligned, settling in Oldroyd-B fluid. In the viscoelastic fluid studied, the DKT process was inverted, which means that when two particles horizontally aligned start to settle, then they will perform lateral drafting, collide and finally tumble. The final configuration was both particles settling in a stable vertical alignment.

Daugan et al. (2002) conducted experiments of two vertically aligned spherical particles settling in Xanthan gum in a creeping flow regime $\text{Re}_D < 10^{-2}$). In their analysis, the distance between particles varied from 5 to 60 diameters. If the separation distance were less than critical, the trailing particle would have a higher velocity than the leading particle, causing them to create a chain. The chain formation is attributed to the shear-thinning behavior of the fluid that will create a "corridor of reduced viscosity" and consequently increasing the trailing particle velocity. The critical separation distance was between 15 and 30 diameters depending on the fluid properties. Daugan et al. (2002) also presented data regarding the ratio of the settling velocity of the leading and trailing sphere as a function of the non-dimensional separation distance, which increases as the particles get closer.

Yu et al. (2006) utilized a finite element method to analyze the settling of two spheres in a structural parameter thixotropic model. Their study focused mainly on a Reynolds number of 0.1. It was noted, on their numerical model, that the trailing particle would start to accelerate when it reached the initial position of the leading particle. When more than two particles settle together, the chain behavior was

observed, but was not stable, causing the DKT process to repeat multiple times over time between the particle that formed the chain.

Moseley et al. (2019) obtained experimental results of two spheres settling in Xanthan gum. The experiments were conducted for a Reynolds number of 0.04. Data was obtained using particle image velocimetry, allowing to obtain the velocity field in the settling direction. They also provided a correlation for the particle velocities.

3.2   Immersed Bodies in Lattice Boltzmann Method

The lattice Boltzmann method is one of the methods that researchers have to numerically study fluid flows. One of the LBM benefits is the higher level of parallelization when compared to velocity-pressure solvers utilized in conventional CFD methods. The basic LBM can then be modified to include the effects of solid boundaries and non-Newtonian fluid behavior. This section introduces the available methods to model these solid objects when coupled with the LBM, and the reasoning to behind choose the immersed boundary method.

First, the simplest method to implement the no-slip boundary condition in LBM is the bounce-back method. In the bounce-back method, the populations are reflected to their oncoming position when meeting a flat wall. Following this principle, Ladd and Verberg (2001) developed a method to enable both static and moving walls. The method exhibits some advantages and disadvantages, one of them is that the boundary exists somewhere between the lattice, however, it is viscosity dependent.

Following a different route to work around viscosity dependency of the bounce-back method, Zou and He (1997) developed the Non-equilibrium Bounce-Back Method (NEBB). In this formulation, the non-equilibrium populations are reflected instead and while the lattice nodes are placed on the fluid-solid interface. These modifications removed the viscosity dependence and allowed it to be a third-order accurate scheme. Nevertheless, the issue that the lattice structure defines where the fluid-solid interface is not removed from either of these approaches, causing the staircase effect when modeling curved walls.

Researchers developed several techniques to improve the model's accuracy near curved boundaries. Lallemand and Luo (2003) modified the bounce-back method making the interpolation based on the distance between the boundary and the lattice nodes. Yu et al. (2002) developed the multi-block strategy that allows the existence of fine and refined lattice in the same domain with a coarse one. For movable boundaries, the method needs adaptive mesh refinement, first utilized in Yu and Fan (2010).

The no-slip condition can also be modeled by using the partially saturated bounce-back method, initially idealized by Noble and Torczynski (1998), where the bounce-back depends on the fluid saturation in the lattice. Figure 3.4 represents a schematic of this method, where each lattice cell has a solid/fluid ratio. For cells that describe the immersed body, the value is 1, while for fluid cells the value is 0. The computational challenge of this method is in determining the solid fraction for each time-step when working with a moving particle. This occur because populations need to be transported when a lattice that previously only had fluid and now has part of it occupied by a solid, in order to conserve the system mass.

Finally, there is the Immersed Boundary Method (not exclusive for LBM) designed by Peskin (1972). On this approach, a set of Lagrangian points represent a surface by exerting a body force in the momentum transport equation. By doing that, the fluid decelerates in order to satisfy non-penetration and

Figure 3.4 – Two-dimensional sketch of two DEM spheres mapping on the LBM lattice grid with the lattice resolution N =5. The darkness of a lattice cell corresponds to its solid ratio: white ($\epsilon = 0$), grey ($0 < \epsilon < 1$) and black (ϵ=1) refer to fluid, partially saturated and solid cells, respectively.
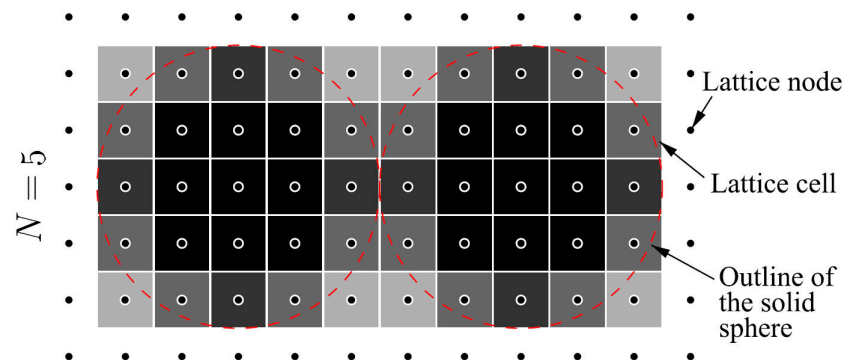
Source: Reprinted from Computers and Geotechnics, Vol 114, G.C. Yang,L. Jing,C.Y. Kwok,Y.D. Sobral, A comprehensive parametric study of LBM-DEM for immersed granular flows, 103100, with permission from Elsevier.

no-slip in surface that is represented by the Lagrangian points. Figure 3.5 represents a circular surface overlapped with an Eulerian domain.

Figure 3.5 – Representation of Lagrangian and Eulerian nodes.
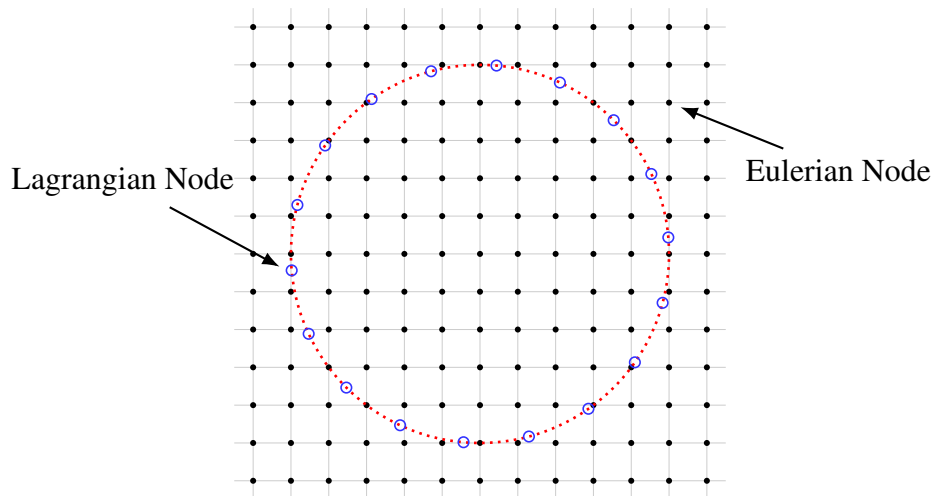
Source: Own elaboration.

Feng and Michaelides (2004) implemented the IBM coupled within the LBM scheme. In their method, each node of the Lagrangian mesh applies a local body force in the nearest lattices, scaled by a kernel. The forces then changes the particle distribution function and consequently modifies the flow velocity. The problem arises when trying to determine the correct force direction and magnitude so that no-slip condition be satisfied in the boundary nodes. Several techniques were developed to solve this problem.

The first approach is the explicit feedback adopted in Feng and Michaelides (2004). In this method, the force is proportional to the node displacement, similar to Hooke's law. However, on this method, instabilities will arise if an unsatisfactory proportionality constant value is chosen. Other methods were designed in other to bypass this problem.

One of them is the implicit velocity correction developed by Uhlmann (2005) and applied into the LBM by Wu and Shu (2009). The method solves simultaneously both the force required and the no-slip condition in the boundary nodes, which it is accomplished by building a linear equation system. The number of variables in the system increases with the number of Lagrangian nodes. For movable boundaries, a new linear equation system is necessary for each time-step, a computationally costly operation for a broad set of Lagrangian nodes.

An iterative process to determine the force was formulated in the works of Luo et al. (2007) and Wang et al. (2008) with LBM implementation by Kang and Hassan (2011) denominated multi-direct-forcing scheme. The force and the velocity interpolation are then locally evaluated by the iterative method, which avoids solving the linear equation system in each time step. The current work opted for the iterative formulation of Kang and Hassan (2011), due to reduced memory usage.

Because two grid coexist in the method (one Lagrangian and another Eulerian), the discretization ratio between then will have a effect over the solution. Fučík et al. (2019) analysed its effect for a flow over a fixed sphere and concluded that a ratio close to 1 presented satisfactory results for drag coefficient. This result will be later investigated in the present work.

Chapter Summary

In this chapter, it was presented the literature review regarding the particle settling phenomenon in non-Newtonian fluids. The drafting-kissing-tumbling process when two particles interact was reviewed, as well as the changes that might occur in non-Newtonian fluids. It was observed by the author that exists a scarcity of studies regarding the settling of two particles in thixo-viscoplastic fluids. From the works researched, the particles are relatively small, around 1mm in diameter, and settle in the creeping flow regime. For the problem declared in chapter 1, the particles are larger, up to 5mm, and density ratio particle-fluid up to 3. Therefore, it exists a scientific opportunity regarding the settling of two particles in different geometry, fluid, and flow configurations. The multiple methods to model immersed bodies in the lattice Boltzmann method were presented, and the immersed boundary method was chosen due to its ease of implementation compared to the other available method. The next chapter will present the mathematical and numerical methods used in the implementation of LBM-IBM for non-Newtonian fluids.

4 NUMERICAL METHOD

This chapter presents the mathematical basis of the lattice Boltzmann method to model the fluid flow. Next, the mathematical formulation used to consider the effects of non-Newtonian fluids, including thixotropy, is explained. The particle settling is then modeled using the immersed boundary method. The collisions between two particles and the walls use a soft sphere model, where the collision force is a function of the inter-particle penetration. Finally, the methods coupling and the algorithm's flowchart is described.

4.1 The Lattice Boltzmann Method

As previously mentioned in Chapter 1, the particle dynamics can be modeled by the Boltzmann equation, which represents the time evolution of the particle distribution function f (BOLTZMANN, 1896 apud KREMER, 2010):

$$\partial_t f + \boldsymbol{\xi} \cdot (\nabla_\mathbf{x} f) + \mathbf{g} \cdot (\nabla_{\boldsymbol{\xi}} f) = \int \left(f_1' f' - f_1 f \right) (\boldsymbol{\xi}_1 - \boldsymbol{\xi}) \, d\Psi d\boldsymbol{\xi}_1 = \Omega \tag{4.1}$$

where $\boldsymbol{g}$ is the acceleration field, $\nabla_{\boldsymbol{x}} = \partial/\partial x_\alpha$, $\nabla_{\boldsymbol{\xi}} = \partial/\partial \xi_\alpha$ and Ω is the collision operator responsible for the change in the particle trajectory due to collisions with other groups of particles [1]. Which assumes a rarefied gas, negligible external force during collision, assumption of molecular chaos and a small variation of the distribution function over time (BOLTZMANN, 1896 apud KREMER, 2010). If enough time is given, a point in the space will reach an equilibrium state. This equilibrium is achieved when the number of particles in a particular state that enters and leaves the space is equal ($\Omega = 0$). Applying this condition in the Eq. 4.1 is possible to determine the particle distribution function as (PHILIPPI et al., 2006):

$$f^{eq} = n \left(\frac{m}{2\pi k \mathcal{T}} \right)^{\frac{d}{2}} \exp \left[-\frac{(\boldsymbol{\xi} - \boldsymbol{u})^2}{2k\mathcal{T}/m} \right] \tag{4.2}$$

where d is the number of Euclidean dimensions, k is the Boltzmann constant, $\mathcal{T}$ is the temperature, $\boldsymbol{\xi}$ is the particle velocity, $\boldsymbol{u}$ is the particle mean velocity, and m is the particle's mass. The Eq. 4.2 is denominated the Maxwell-Boltzmann distribution function and represent the probability equilibrium distribution function of particles to be in a given velocity state. The lattice Boltzmann method is based on the discrete form of the Boltzmann equation, Eq. 4.1. Bhatnagar et al. (1954) proposed a simplification of the collision operator. In their model, currently called the BGK collision operator, Ω is defined as:

$$\Omega = \frac{f^{eq} - f}{\tau} \tag{4.3}$$

where τ is a relaxation time parameter, and f^{eq} is the particle equilibrium distribution function. There are other collision operators, for example, the two relaxation time (TRT)(GINZBURG et al., 2008) and the multiple relaxation time (MRT)(HUMIERES, 1994). Both models increase the number of relaxation parameters when compared with BGK in order to increase the stability of the model, but they also might raise the simulations computational cost.

---

[1] f' and f_1' represent post collision values of two particle which have the respectively pre-collision velocities: ξ and ξ_1.

4.1.1 Discretization of Boltzmann equation

The discretization of the Boltzmann equation, Eq. 4.1, requires a transformation of the phase space into a discrete domain. Because the LBM originates from the lattice gas automata (LGA), the phase space is divided into lattices that accommodate the particle populations between each time step. These particles can only travel to other lattices by determined paths defined by velocity sets.

The velocity space can be discretized by using Hermite polynomials (HE and LUO, 1997), (SHAN et al., 2006), (PHILIPPI et al., 2006). The discretization then returns a group of lattice directions on which the particles can move, denominated velocity sets. The velocity sets are commonly classified based on the number of spatial dimensions and discrete velocities. For two dimensional space and isothermal case, the most common velocity set that preserves the mass and momentum is the D2Q9 (2 dimensions and 9 directions). While for three-dimensional space and isothermal, it is the D3Q19 (3 dimensions and 19 directions), shown in Fig. 4.1.a , and the D3Q27(3 dimensions and 27 directions), Fig. 4.1.n.

Figure 4.1 – a) D2Q9 and b) D3Q19 velocity sets.
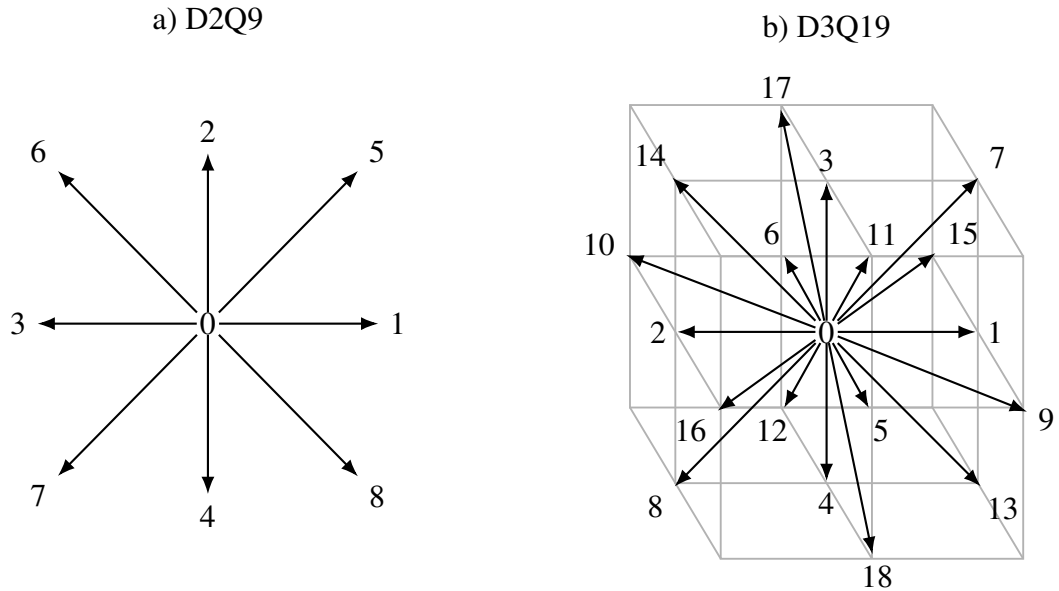
Source: Own elaboration.

Another important part related to the velocity space is the discretization of the equilibrium distribution function, 4.2, which requires that the first moments in the velocity space of the discrete function being equal to the moments in the continuous velocity space. By using Hermite polynomials expansions (PHILIPPI et al., 2006):

$$f_i^{eq} = w_i \rho \left[1 + \frac{c_{i\alpha} u_\alpha}{c_s^2} + \frac{u_\alpha u_\beta \left(c_{i\alpha} c_{i\beta} - c_s^2 \delta_{\alpha\beta} \right)}{2c_s^4} \right] \tag{4.4}$$

where c_s is the speed of sound, u is the fluid velocity, c_i is the velocity vector and w_i is the direction weight. For the velocity sets previously mentioned (D2Q9, D3Q19, D3Q27), the speed of sound is equal to $1/\sqrt{3}$, while the other constants (c_i and w_i), are exposed in Table 4.1.

The Eq. 4.1 in the discrete DdQq velocity space can be described as (HE et al., 1998):

$$\partial_t f_i + c_{i\alpha} \partial_\alpha f_i = \Omega_i + F_i, \quad i = 0, \ldots, q-1 \tag{4.5}$$

Table 4.1 – Weight values for D2Q9 and D3Q19 velocity schemes.

Velocity Set	i	w_i
	0	16/36
D2Q9	$1-4$	4/36
	$5-8$	1/36
	0	12/36
D3Q19	$1-6$	2/36
	$7-18$	1/36

Source: Own elaboration.

using the BGK collision operator and with a discretization over time:

$$
\begin{aligned}
f_i \left(\boldsymbol{x} + c_i \Delta t, t + \Delta t \right) - f_i \left(\boldsymbol{x}, t \right) = \\
- \frac{1}{\tau} \int_0^{\Delta t} \left[f_i \left(\boldsymbol{x} + c_i s, t + s \right) - f_i^{eq} \left(\boldsymbol{x} + c_i s, t + s \right) \right] ds + \int_0^{\Delta t} F_i \left(\boldsymbol{x} + c_i s, t + s \right) ds
\end{aligned}
\tag{4.6}
$$

with a second order discrete integration scheme is:

$$
\begin{aligned}
f_i \left(\boldsymbol{x} + c_i \Delta t, t + \Delta t \right) - f_i \left(\boldsymbol{x}, t \right) = &- \frac{\Delta t}{2\tau} \left[f_i \left(\boldsymbol{x} + c_i \Delta t, t + \Delta t \right) - f_i^{eq} \left(\boldsymbol{x} + c_i \Delta t, t + \Delta t \right) \right] \\
&- \frac{\Delta t}{2\tau} \left[f_i \left(\boldsymbol{x}, t \right) - f_i^{eq} \left(\boldsymbol{x}, t \right) \right] \\
&+ \frac{\Delta t}{2} F_i \left(\boldsymbol{x} + c_i \Delta t, t + \Delta t \right) + F_i \left(\boldsymbol{x}, t \right) + \mathcal{O} \left(\Delta t^3 \right)
\end{aligned}
\tag{4.7}
$$

adopting the variable change proposed by He et al. (1998):

$$
\bar{f}_i = f_i + \frac{\Delta t}{2\tau} \left(f_i - f_i^{eq} \right) - \frac{\Delta t}{2} F_i
\tag{4.8}
$$

considering $\Delta t = 1$ the Eq. 4.7 becomes:

$$
\bar{f}_i \left(\boldsymbol{x} + c_i \Delta t, t + \Delta t \right) = \left(1 - \omega \Delta t \right) \bar{f}_i \left(\boldsymbol{x}, t \right) + \omega \Delta t f_i^{eq} \left(\boldsymbol{x}, t \right) + \left(1 - \frac{\omega \Delta t}{2} \right) F_i \left(\boldsymbol{x}, t \right) \Delta t
\tag{4.9}
$$

where ω is the relaxation frequency defined as the inverse of the relaxation time. Equation 4.9 can be divided into two operations denominated "Streaming" and "Collision". The collision part is represented as:

$$
f_i^* \left(\boldsymbol{x}, t \right) = \left(1 - \omega \Delta t \right) \bar{f}_i \left(\boldsymbol{x}, t \right) + \omega \Delta t f_i^{eq} \left(\boldsymbol{x}, t \right) + \left(1 - \frac{\omega \Delta t}{2} \right) F_i \left(\boldsymbol{x}, t \right) \Delta t
\tag{4.10}
$$

where the particle collisions occur, and the populations on the lattices are calculated, represented by Fig. 4.2.a. In the second part of the equation denominated streaming, the populations propagate to neighboring lattices, the right side of Fig. 4.2.b. Both of these operations happen at the same time step.

$$
\bar{f}_i \left(\boldsymbol{x} + \boldsymbol{c}_i \Delta t, t + \Delta t \right) = f_i^* \left(\boldsymbol{x}, t \right)
\tag{4.11}
$$

Knowing the particle populations is not enough to solve engineering problems. It is also necessary to know the macroscopic properties: pressure and velocity. These macroscopics can be obtained by calculating the lower order moments in the velocity space (SILVA and SEMIAO, 2012):

$$
\rho = \Pi_0 = \sum_i \bar{f}_i + \frac{\Delta t}{2} \sum_i F_i
\tag{4.12a}
$$

$$
\rho u_\alpha = \Pi_\alpha = \sum_i \bar{f}_i c_{i\alpha} + \frac{\Delta t}{2} \sum_i F_i c_{i\alpha}
\tag{4.12b}
$$

Figure 4.2 – Collision–streaming process. On the collision (a) the particles collide and change direction. While on the streaming step (b) the particles propagate to neighbor lattices.

a) Collision   b) Streaming
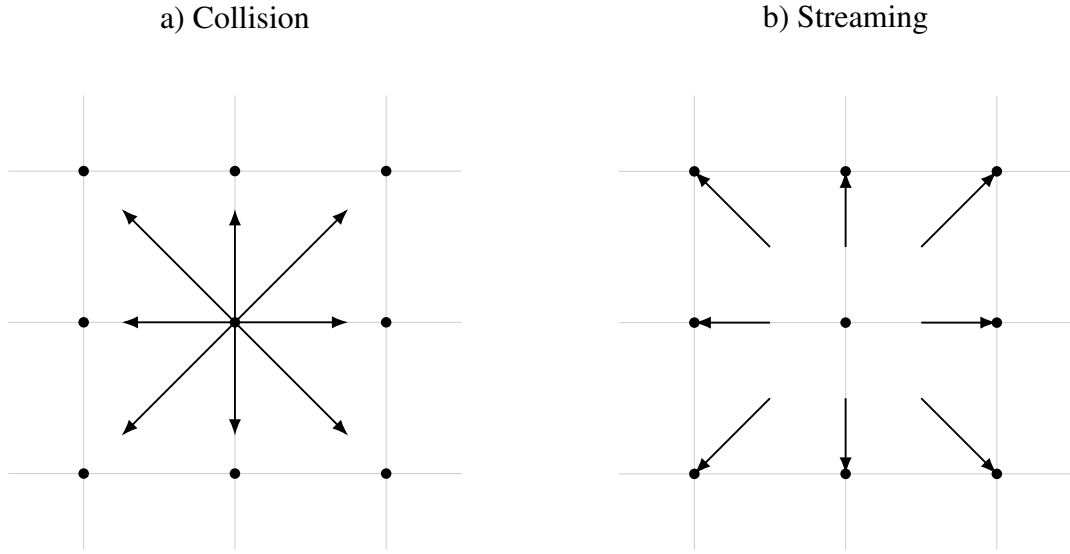
Source: Own elaboration.

It is also necessary to define the force term presented in Eq. 4.9 and Eq. 4.12. The force can be obtained the same way as the equilibrium distribution function, through Hermite polynomials expansions (SHAN et al., 2006). For a second-order discretization, the force term can be approximate as (GUO et al., 2002):

$$F_i = w_i \left[\frac{c_{i\alpha}}{c_s^2} + \frac{\left(c_{i\alpha} c_{i\beta} - c_s^2 \delta_{\alpha\beta} \right) u_\beta}{c_s^4} \right] F_\alpha \tag{4.13}$$

A critical aspect is that the lattice Boltzmann method can be used to model fluid flow. If the BGK collision operator is utilized, the Boltzmann equation returns the Navier-Stokes equations if the relaxation time is correlated with the fluid viscosity as (GUO et al., 2002):

$$\eta = \rho c_s^2 \left(\tau - \frac{\Delta t}{2} \right) \tag{4.14}$$

4.1.2 Regularized Lattice Boltzmann Method

One of the methods to increase the accuracy and stability of the lattice Boltzmann method is the pre-collision regularization proposed by Latt and Chopard (2006). On this approach, instead of propagating the particle distribution function, it is used the regularized populations. The regularized distribution function with a force term is defined as:

$$f_i^{reg} = f_i^{eq} + f_i^{(1)} \tag{4.15}$$

where $f_i^{(1)}$ is the second term of expansion $f_i = f_i^{(0)} + \epsilon f_i^{(1)} + \epsilon^2 f_i^{(2)} + \dots$ from the Chapman-Enskog expansion (BUICK and GREATED, 2000). The term $f_i^{(1)}$ can be correlated with the force term of the Boltzmann equation as (LUGARINI et al., 2020):

$$\epsilon f_i^{(1)} \approx \frac{w_i}{2c_s^4} \left[\left(c_{i\alpha} c_{i\beta} - c_s^2 \delta_{\alpha\beta} \right) \sum_i f_i^{neq} c_{i\alpha} c_{i\beta} - \Delta t c_s^2 c_{i\alpha} F_\alpha \right] \tag{4.16}$$

where f_i^{neq} is the non-equilibrium distribution function defined as:

$$f_i^{neq} = f_i - f_i^{eq} \tag{4.17}$$

using the definition of regularized population, Eq. 4.15, into Eq. 4.10, is obtained the regularized lattice Boltzmann equation with force term:

$$f_i^* \left(\boldsymbol{x}, t \right) = \left(1 - \frac{\Delta t}{\bar{\tau}} \right) f_i^{reg} \left(\boldsymbol{x}, t \right) + \frac{\Delta t}{\bar{\tau}} f_i^{eq} \left(\boldsymbol{x}, t \right) + \left(1 - \frac{\Delta t}{2\bar{\tau}} \right) F_i \left(\boldsymbol{x}, t \right) \Delta t \tag{4.18}$$

Another advantage of this method is the local calculation of $\Pi_{\alpha\beta}^{neq}$, which correlates to the viscous stress tensor (SILVA and SEMIAO, 2012), which will be necessary to model a non-Newtonian fluid behavior.

4.2 Boundary Conditions

In order to correctly simulate a problem is necessary to define what is the fluid's behavior on the system's boundary. In the finite volume method, the macroscopic quantities, such as pressure and velocity, are defined in the boundary surface. Meanwhile, in the LBM context, this is achieved by changing how the streaming-collision process behaves in the boundary lattices. On this work mainly three boundary conditions are utilized: symmetry, periodicity, and walls. Here is utilized the D2Q9 scheme for visualization purposes.

4.2.1 Periodic

The periodic boundary condition considers that the fluid leaving through a surface will resurface on the opposite surface. It is mainly used to model channel flows or represent periodic arrangements such as porous media or an array of immersed bodies. In the lattice Boltzmann method is the periodic boundary condition is computed by a modification of the streaming equation, Eq. 4.11, as (KRÜGER et al., 2017):

$$f_i \left(\boldsymbol{x}, t \right) = f_i^* \left(\boldsymbol{x} + \boldsymbol{L} - c_i \Delta t, t \right) \tag{4.19}$$

where L is the domain's period, implicating that the population leaving in one of the boundaries will be transported to the boundary on the opposite side, as represented in Fig. 4.3:

Figure 4.3 – Representation of a periodic boundary condition for D2Q9 scheme with a period of $L = 7$.
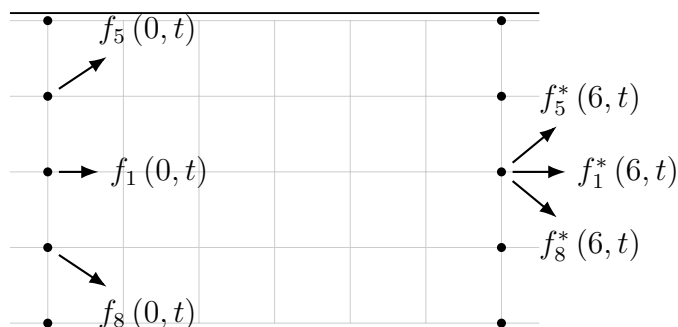
Source: Own elaboration.

In the middle node at $x = 6$, three post-collision populations are leaving the domain (f_1^*, f_5^* and f_8^*). Because no lattices exist outside of the domain and the periodic condition is applied in the east and west sides, these populations will stream to lattices at $x = 0$.

4.2.2 Symmetry / Free-slip

The symmetry and free-slip boundary conditions are often used to reduce the domain size. It applies zero normal velocity through its plane, which can be accomplished in the LBM by reflecting the streaming of the populations specularly (KRÜGER et al., 2017):

$$f_i \left(\boldsymbol{x} + \boldsymbol{c}_j \Delta t, t + \Delta t \right) = f_i^* \left(\boldsymbol{x}, t \right) \tag{4.20}$$

where $\boldsymbol{c}_j = -\boldsymbol{c}_i$, meaning that the velocity components opposite to the symmetry plane have the signal reversed. Figure 4.4 represents this condition, applied to the populations f_2, f_5, and f_6.

Figure 4.4 – Representation of a symmetric/free-slip boundary condition for D2Q9 scheme post-collision (a) and post-streaming (b).
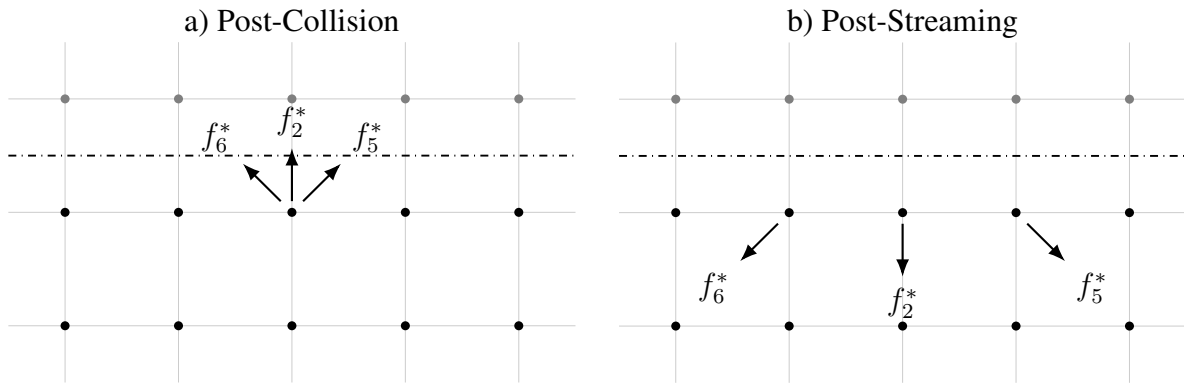
Source: Own elaboration.

4.2.3 No-Slip

The no-slip boundary condition makes the fluid near a wall have the same velocity as the wall itself. In the LBM, this condition translates to determining the unknown populations from the wall while also respecting the no-slip condition. It can be adopted two approaches to solve this problem. The first is the wet-node, which considers the lattice being approximately in the same position as the boundary, and the macroscopic condition is imposed. Inside this approach, there are several methods to find the unknown populations, such as the non-equilibrium bounce-back scheme by Zou and He (1997), which uses the non-equilibrium populations.

The other approach is the link-wise, in which the boundary is located between a fluid node and a solid node. The most common method on this approach is the half-way bounce back method. In this method, the unknown populations are obtained by the reflection back to the original position, as showed in Fig.4.5.

Figure 4.5 – Representation of a link-wise no-slip boundary condition in D2Q9 scheme post-collision (a) and post-streaming (b).

a) Post-Collision

b) Post-Streaming
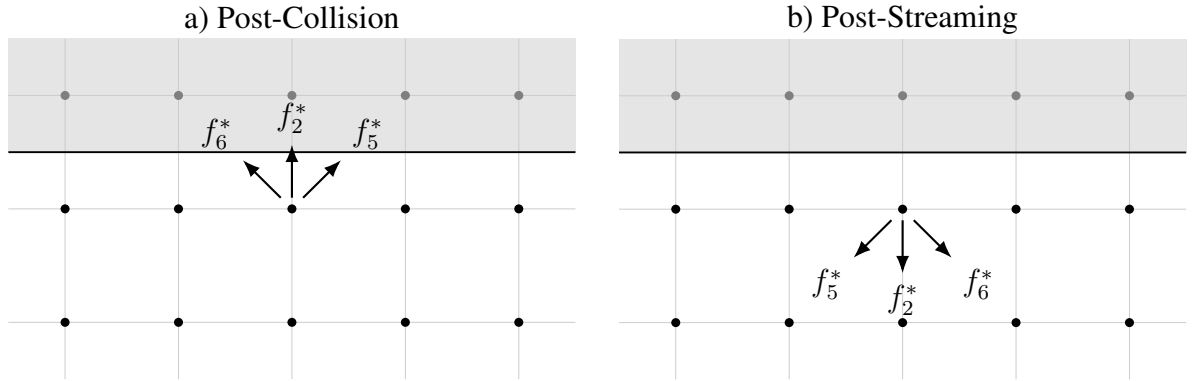
Source: Own elaboration.

For moving walls, this boundary can mathematically be expressed as (LADD and VERBERG, 2001):

$$f_{\bar{i}}\left(\boldsymbol{x}, t + \Delta t\right) = f_i^*\left(\boldsymbol{x}, t\right) - 2w_i\rho_w \frac{\boldsymbol{c_i} \cdot \boldsymbol{u_w}}{c_s^2} \tag{4.21}$$

where $\bar{i}$ represents the opposite velocity direction, $\boldsymbol{u_w}$ is the wall velocity in $\boldsymbol{x} + \boldsymbol{c_i}\Delta t/2$.

One of the LBM problems is about corner treatment, especially in three-dimensional problems, which can cause some directions to other lattices. The wrong treatment of the corners might not lead to the mass conservation of the system by removing or adding populations.

4.3 Lattice Boltzmann method for non-Newtonian Fluids

In order to model non-Newtonian fluids in LBM is usually necessary to compute stress tensor and strain tensor in each lattice. From Silva and Semiao (2012) the viscous stress tensor can be computed as:

$$\sigma_{\alpha\beta} \approx -\left(1 - \frac{\Delta t}{2\tau}\right)\sum_i \left(f_i - f_i^{eq}\right)c_{i\alpha}c_{i\beta} - \frac{\Delta t}{2}\left(1 - \frac{\Delta t}{2\tau}\right)\left(F_\alpha u_\beta + u_\alpha F_\beta\right) = \left(1 - \frac{\Delta t}{2\tau}\right)T_{\alpha\beta} \tag{4.22}$$

then the stress tensor can be correlated with the rate of strain-rate tensor $\dot{\gamma}_{\alpha\beta}$ for a generalized Newtonian fluid, by using the viscosity information from the previous time-step:

$$\dot{\gamma}_{\alpha\beta}^n = \frac{\sigma_{\alpha\beta}^n}{\eta\left(|\dot{\gamma}|\right)^{n-1}} \tag{4.23}$$

where n is the time-step. An option is utilize iterative methods in order to avoid using explicit formulation, Appendix A. With the rate of strain tensor determined in each point, the apparent viscosity on the next time is determined using the proper constitutive equation of the non-Newtonian fluid. Using a reordered version of Eq. 4.14 the relaxation frequency ω is determined for the streaming-collision LBM step is:

$$\frac{1}{\tau} = \left(\frac{\eta}{c_s^2} + \frac{\Delta t}{2}\right)^{-1} = \omega \tag{4.24}$$

For fluids that exhibit yield stress, it is necessary to make some modifications. If the stress is smaller than the yield stress, it can be numerically modeled as the apparent viscosity tends to infinity, this will

cause $\omega \rightarrow 0$. If the stress is greater than the yield stress, then the viscosity is modeled according to the Eq. 4.24.

4.3.1 Thixotropy modeling

It will be used a structural parameter model to model thixotropy, as mentioned in Chapter 2. On this approach, the thixotropy is based on the parameter (λ), which determines the structural level of the fluid. The time-dependency is then described based on the transport evolution equation for λ:

$$\frac{\partial \lambda}{\partial t} + u_i \frac{\partial \lambda}{\partial x_i} = -k_1|\dot{\gamma}|\lambda + k_2(1 - \lambda) \tag{4.25}$$

Derksen and Prashant (2009) utilized explicit finite volume discretization with flux limiter to solve this transport equation and reduce the numerical diffusion. Derksen and Prashant (2009) pointed out that it is possible to solve this transport equation in the LBM context, that will be opted in this work in order to take advantage of the GPU architecture. Equation 4.25 is part of a more general transport equation that accounts for diffusive terms:

$$\frac{\partial \lambda}{\partial t} + \frac{\partial (u_i \lambda)}{\partial x_i} = \frac{\partial}{\partial x_i}\left(\mathfrak{D}\frac{\partial \lambda}{\partial x_i}\right) + q \tag{4.26}$$

where $\mathfrak{D}$ is the diffusive coefficient and $q = -f_{break} + f_{build}$. Similar to the lattice Boltzmann method, this equation can be discretized as (SETA, 2013):

$$g_i\left(\boldsymbol{x} + c_i\Delta t, t + \Delta t\right) = \left(1 - \frac{1}{\tau_g}\right)g_i\left(\boldsymbol{x}, t\right) + \frac{1}{\tau_g}g_i^{eq}\left(\boldsymbol{x}, t\right) + \left(1 - \frac{1}{2\tau_g}\right)w_i q\left(\boldsymbol{x}, t\right) \tag{4.27}$$

$$g_i^{eq} = w_i\lambda\left(1 + \frac{c_{i\alpha}u_\alpha}{c_s^2} + \frac{(c_{i\alpha}u_\alpha)^2}{2c_s^4} - \frac{u_\alpha u_\alpha}{2c_s^2}\right) \tag{4.28}$$

$$\lambda = \sum_i g_i + \frac{Q_i\Delta t}{2} \tag{4.29}$$

where through Chapman-Enskog analysis it returns the Eq. 4.26 if:

$$\omega_g = \frac{1}{\tau_g} = \left(\frac{\mathfrak{D}}{c_s^2} + \frac{\Delta t}{2}\right)^{-1} \tag{4.30}$$

where τ_g is the relaxation time and $\mathfrak{D}$ is the diffusion coefficient of the convection-diffusion equation, Eq. 4.26, which only returns the Eq. 4.25 if $\tau_g = 0.5$. However, adopting a value of 0.5 for the relaxation time is infeasible due to the nature of LBM, where is unstable for this value and so is necessary to utilize a value close to it. The method is similar to the one adopted by Guo et al. (2002) with the Boussinesq approximation for buoyancy or in Malaspinas et al. (2010) and Wang et al. (2019) to transport the conformation tensor in viscoelastic fluids.

Chopard et al. (2009) underline an issue in using this formulation for the advection-diffusion equation. It was observed the necessity of correction factor in Eq. 4.27, which will depend on the equilibrium distribution function chosen. For the equilibrium distribution adopted, the correction factor is:

$$F_i = -\frac{w_i}{c_s^2}\left(1 - \frac{1}{2\tau_g}\right)\frac{\rho}{\rho_f}c_i\nabla p_f \tag{4.31}$$

where ρ_f is the fluid density and p_f is the pressure field. But since a value of $\tau_g \approx 0.5$ will be utilized, the correction factor will be $F_i \approx 0$, and consequently, the error if ignored, will be small. In order to

reduce overall memory usage, will be used reduced velocity set (D3Q7) for the transport of the structural parameter. According to Ginzburg et al. (2010) this should not be an issue regarding numerical stability or accuracy based on the results of Wang et al. (2019).

With the structural parameter and the stress tensor determined in every lattice is then possible to calculate the apparent viscosity and, consequently, the local relaxation frequency based on Eq. 4.24, which is used in the next time-step. In this work, the thixotropic model adopted is a simplified version of the one proposed by (HOUSKA, 1981), which is reproduced below:

$$\sigma = \eta(\dot{\gamma}, \lambda)\dot{\gamma}, \tag{4.32a}$$

$$\eta(\dot{\gamma}, \lambda) = \begin{cases} \infty & , |\sigma| \le \sigma_y \\ \eta_p + \tau_y|\dot{\gamma}| & , |\sigma| > \sigma_y \end{cases} \tag{4.32b}$$

$$\sigma_y = \lambda\sigma_{y,0} + (1 - \lambda)\sigma_{y,\infty} \tag{4.32c}$$

$$\frac{\partial \lambda}{\partial t} + u_i \frac{\partial \lambda}{\partial x_i} = -k_1\lambda|\dot{\gamma}| + k_2(1 - \lambda) \tag{4.32d}$$

The model adopted has five constants: k_1 represents the breakdown rate caused by shear, k_2 is the build-up parameter, η_p is the plastic viscosity, $\sigma_{y,0}$ and $\sigma_{y,\infty}$ the static and dynamic yield stress. Through some algebraic manipulation, for this constitutive equation, is possible to avoid the different time steps in Eq. 4.23. The relaxation frequency is then defined as, Appendix A:

$$\omega = \omega_p \max\left(0, 1 - \frac{\lambda\sigma_{y,0} + (1 - \lambda)\sigma_{y,\infty}}{|T|}\right) \tag{4.33}$$

where $\omega_p = (1/2 + 3\eta_p)^{-1}$ and T is the auxiliary stress tensor from the Eq. 4.22:

$$|\sigma| \approx \left(1 - \frac{\Delta t}{2\tau}\right)|T| \tag{4.34}$$

4.4 Immersed Boundary Method

4.4.1 Continuous IBM

The Immersed Boundary Method (IBM) was developed by Peskin (1972) in order to study the blood flow patterns inside a heart. In this method, a body force term is added to the momentum transport equations and with its location in the surface of a immersed boundary. The force magnitude and direction is defined to exert in the flow the same effects that wall would apply, i.e.: no-penetration and no-slip. This boundary is then composed of Lagrangian poins (Γ), that must have the same velocity as the fluid in order to satisfy the non-slip boundary condition, hence:

$$\frac{\partial \boldsymbol{X}(s,t)}{\partial t} = \boldsymbol{u}(\boldsymbol{X}(s,t),t) \tag{4.35}$$

where $\boldsymbol{u}$ is the fluid velocity on the boundary node location and $\boldsymbol{X}(s,t)$ is the Lagrangian surface coordinates. The body force defined in the Lagrangian surface it is then transferred to the fluid domain (Θ):

$$\boldsymbol{F}^E(\boldsymbol{x},t) = \int_\Gamma \boldsymbol{F}^L(s,t)\,\delta(\boldsymbol{x} - \boldsymbol{X}(s,t))\,ds \tag{4.36}$$

where $\delta\left(\boldsymbol{x}-\boldsymbol{X}\left(\boldsymbol{s},t\right)\right)$ is the Dirac delta function. Meanwhile, this same transformation can be applied for no-slip condition:

$$\frac{\partial \boldsymbol{X}\left(s,t\right)}{\partial t} = \int_{\Theta} \boldsymbol{u}\left(\boldsymbol{x},t\right)\delta\left(\boldsymbol{x}-\boldsymbol{X}\left(s,t\right)\right)d\boldsymbol{x} \tag{4.37}$$

4.4.2   Discretized IBM

The first implementation of IBM simultaneously with LBM was presented in the work of Feng and Michaelides (2004), which was discretization of the Lagrangian surface in set of Lagrangian points over the Eulerian Mesh utilized in the LBM, represented in Fig. 4.6.

Figure 4.6 – Representation of Lagrangian ($\boldsymbol{X}\left(s,t\right)$) and Eulerian lattices ($\boldsymbol{x}$) and respective forces (F^L and F^E).
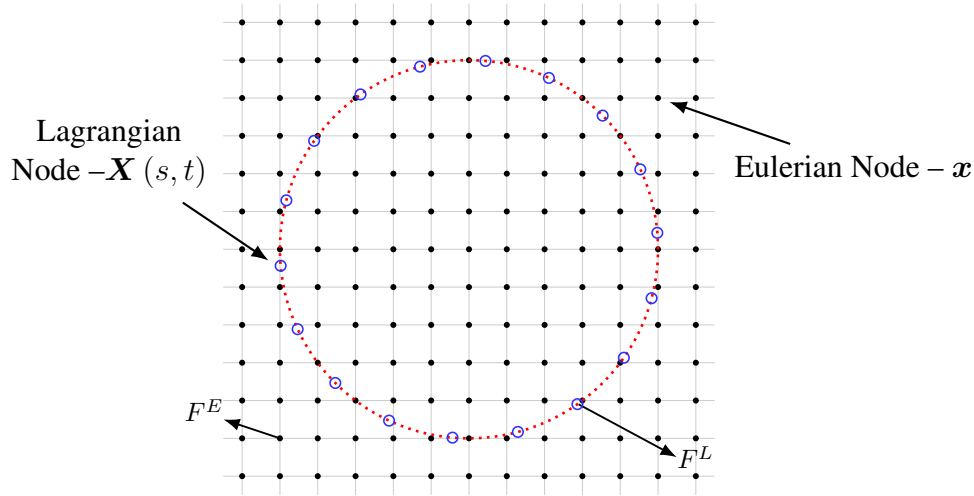
Source: Own elaboration.

The black dots, in the coordinate $\boldsymbol{x}$, represent the lattice nodes and are used in the lattice Boltzmann method. Meanwhile, the blue dots of index s and coordinate $\boldsymbol{X}\left(s,t\right)$, denote the Lagrangian nodes and are part of the immersed boundary method. Each of these nodes has a respective body force acting on them. $\boldsymbol{F}^L\left(s,t\right)$ is the force exerted by the Lagrangian node s while $\boldsymbol{F}^E\left(\boldsymbol{x},t\right)$ is the body force suffered the fluid in the Eulerian domain (Θ).

The continuous Dirac delta function has a value different than zero in just one point. Because of this, the force distribution will only affect the fluid when the position of a Lagrangian node is the same as the Eulerian if this definition is used in a discrete domain. The Dirac delta function then needs to be modified to affect a specific area in order to work around this problem. The Dirac delta function can be mollified for a tridimensional system as (PESKIN, 2002):

$$\varrho\left(\boldsymbol{x}-\boldsymbol{X}\left(s,t\right)\right) = \frac{1}{h^3}\phi\left(\frac{x-X}{h}\right)\phi\left(\frac{y-Y}{h}\right)\phi\left(\frac{z-Z}{h}\right) \tag{4.38}$$

where some of the kernels (ϕ) formulated by Peskin are:

$$\phi_2\left(r\right) = \begin{cases} 1-|r| & 0 \leq |r| \leq 1 \\ 0 & 1 < |r| \end{cases} \tag{4.39}$$

$$\phi_4\left(r\right) = \begin{cases} \frac{1}{8}\left(3 - 2|r| + \sqrt{1 + 4|r| - 4|r|^2}\right) & 0 \leq |r| \leq 1 \\ \frac{1}{8}\left(5 - 2|r| - \sqrt{-7 + 12|r| - 4|r|^2}\right) & 1 < |r| \leq 2 \\ 0 & 2 < |r| \end{cases} \quad (4.40)$$

with r being the distance between the Lagrangian node and the Eulerian lattice and h is the lattice size. The ϕ_4, when compared with ϕ_2 features a smooth distribution, Fig. 4.7.a, but increases the computational load due to the presence of roots and powers. It also affects more lattices, 16 vs 4 in 2 dimensions and 64 vs 8 in 3 dimensions as represented in Fig. 4.7.b. With the same number of points,

Figure 4.7 – Effect of distribution kernel – a) Kernel magnitude as a function of r. b) Bi-dimensional area of effect of the kernels around a Lagrangian node.
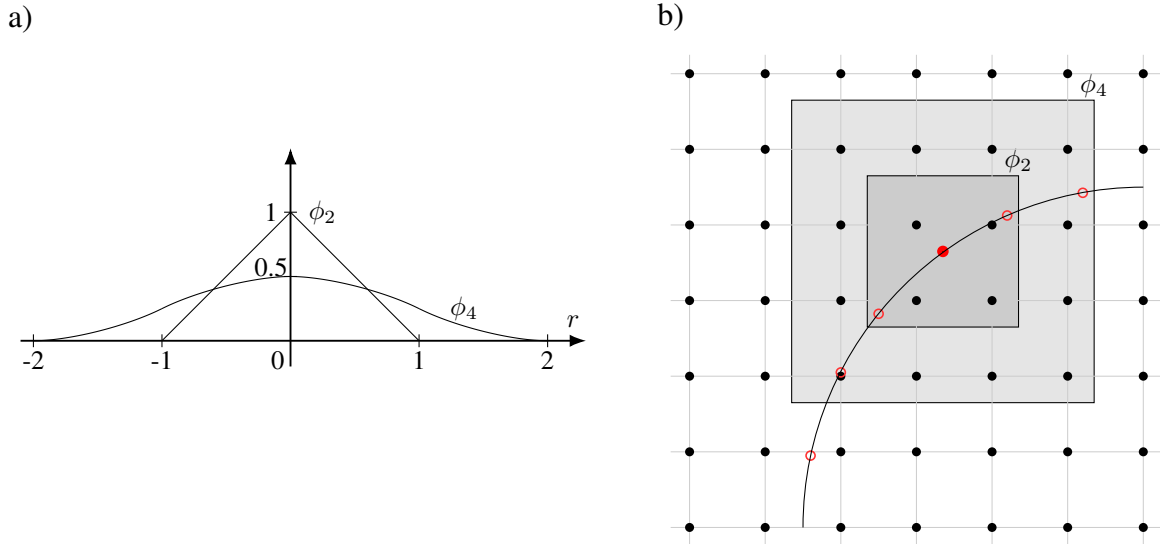
Source: Own elaboration.

ϕ_2 introduces a higher body force in the lattice node when compared to ϕ_4, consequently, it attributes a sharper behavior of ϕ_2 when compared with the diffusive effect of ϕ_4, which spreads the force over a higher number of lattice nodes. It is opted to utilize the ϕ_4 kernel because it offers an increase in the numerical stability for moving particles.

After defining the Dirac delta function for a discrete system is possible to proceed with the derivation of the discrete immersed boundary equations. From the definition of fluid velocity, Eq. 4.35, is possible to separate in two terms, velocity without the force and force correction term:

$$\boldsymbol{u}^E = \frac{1}{\rho}\sum_i \bar{f}_i c_{i\alpha} + \frac{\Delta t}{2\rho}\sum_i F_i c_{i\alpha} = \boldsymbol{u}^{E,noF} + \frac{\Delta t}{2\rho}\boldsymbol{F}^E \quad (4.41)$$

Equation 4.36 can then be discretized as:

$$\boldsymbol{F}^E = \sum_L \boldsymbol{F}^L \varrho\left(\boldsymbol{x} - \boldsymbol{X}\right)\Delta S \quad (4.42)$$

where ΔS is the surface area of the Lagrangian node. The no-slip condition, Eq. 4.37, can also be discretized as:

$$\boldsymbol{u}^L = \sum_E \boldsymbol{u}^E \varrho\left(\boldsymbol{x} - \boldsymbol{X}\right)h^3 \quad (4.43)$$

substituting the Eq. 4.41 and 4.42 in the Eq. 4.43, and after some algebraic manipulation:

$$\boldsymbol{u}^L = \sum_E \boldsymbol{u}^{E,noF} \varrho\left(\boldsymbol{x} - \boldsymbol{X}\right) h^3 + \sum_E \left[\sum_L \frac{\Delta t}{2\rho} \boldsymbol{F}^L \varrho\left(\boldsymbol{x} - \boldsymbol{X}\right) \Delta S\right] \varrho\left(\boldsymbol{x} - \boldsymbol{X}\right) h^3 \qquad (4.44)$$

The linear system can be solved by matrix inversion (WU and SHU, 2010), which for fixed boundaries will stay the same during the simulation. However, for moving boundaries, it is necessary to determine a new matrix for each time step, which is a cumbersome task, and for large domains and nodes would not be viable.

In order to avoid matrix inversion, it is possible to utilize iterative methods to determine the force. One of the methods is the implicit direct forcing method with the diffuse interface used by Kang and Hassan (2011). The method can be improved with a successive relaxation parameter(ε) proposed by Dash et al. (2014). In this method, after the LBM streaming step, the uncorrected velocities are calculated, without the IBM force term:

$$\boldsymbol{u}^{E,noF} = \frac{1}{\rho} \sum_i f_i \boldsymbol{c}_i \qquad (4.45)$$

followed by the calculation of the unforced velocity in the Lagrangian node as

$$\boldsymbol{u}^{L,0} = \sum_E \boldsymbol{u}^{E,0} \varrho\left(\boldsymbol{x} - \boldsymbol{X}\right) h^3 \qquad (4.46)$$

then the iterative procedure begins, with sub-step m. The first step is the evaluation of the force on the boundary node:

$$\boldsymbol{F}^{L,m+1} = 2\rho \frac{\boldsymbol{u}^{L,m} - \sum_E \boldsymbol{u}^{E,m} \varrho\left(\boldsymbol{x} - \boldsymbol{X}\right) h^3}{\Delta t} \qquad (4.47)$$

then the force is distributed to Eulerian lattices:

$$\boldsymbol{F}^{E,m} = \sum_L \boldsymbol{F}^{L,m} \varrho\left(\boldsymbol{x} - \boldsymbol{X}\right) \Delta S \qquad (4.48)$$

The fluid velocities are recalculated with the force correction term:

$$\boldsymbol{u}^{E,m} = \boldsymbol{u}^{E,m-1} + \frac{\Delta t}{2\rho} \boldsymbol{F}^{E,m} \qquad (4.49)$$

and finally, the velocity on the boundary nodes is recalculated:

$$\boldsymbol{u}^{L,m} = \sum_E \boldsymbol{u}^{E,m} \varrho\left(\boldsymbol{x} - \boldsymbol{X}\right) h^3 \qquad (4.50)$$

The algorithm returns to the step represented by Eq. 4.47 and repeats the process. Dash et al. (2014) proposed use of $|\frac{\Delta t}{2\rho} \boldsymbol{F}^{E,m}| \leqq 10^{-6}$ as a stop criterion for the iterative process to ensure the no-slip condition in the wall. Dash et al. (2014) pointed out the necessity of number of sub-steps between 20 and 30 to ensure the no-slip condition in the wall. Finally, the term $\sum_m \boldsymbol{F}^{E,m}$ will correspond to the force necessary to accelerate the fluid from a situation where the immersed boundary does not exist to a state where it exist, in a single time step. Chapter 5 will be verified the necessary number of sub-steps.

4.5 Particle Dynamics

It is necessary to describe its dynamics equations in order to model the movement of a particle inside the fluid. Due to the IBM's nature, the fluid flow inside the immersed boundary still affects the particle movement. Some methods were created by researchers, and their differences investigated in the work of Suzuki and Inamuro (2011), in order to mitigate this problem. Based on their conclusions, the method chosen is the rigid body approximation of Feng and Michaelides (2009), due to the explicitness and no constrains regarding density ratios between particle and fluid. Suzuki and Inamuro (2011) recommend to be careful about its application when there is a significant rotational movement of the immersed body. Because of their results, where a settling sphere showed no apparent errors, this method was adopted.

4.5.1 Movement

The equation for the translation of one particle immersed in a fluid is defined by Newton's second law of motion:

$$m_p \frac{dU}{dt} = \int_{\Gamma p} (\sigma + p) \, dS + (\rho_p - \rho_f) V_p g \qquad (4.51)$$

where the integral term of the right side corresponds to the sum of all forces acting the immersed boundary, while the second term is the buoyancy force, the explicit discrete form is then (FENG and MICHAELIDES, 2009):

$$U_p^{t+1} = \left(1 + \frac{\rho_f}{\rho_p}\right) U_p^t - \frac{\rho_f}{\rho_p} U_p^{t-1} + \frac{1}{m_p} \left[-\sum_{L_p} F^L \Delta S + (m_p - m_f) g \right] \Delta t \qquad (4.52)$$

the negative sign on the force term is due to Newton's Third Law and F^L be the force acting in the fluid. With the particle velocity defined is possible to determine its center in a given time step by the trapezoidal rule as:

$$X_p^{t+1} = X_p^t + \frac{U_p^{t+1} + U_p^t}{2} \Delta t \qquad (4.53)$$

Newton's second law of motion can also be applied for rotation. Thus the equation is defined as:

$$I_p \frac{d\omega}{dt} = -\int_{\Gamma p} (X - X_p) \times \sigma dS \qquad (4.54)$$

with the discrete form:

$$\omega_p^{t+1} = \left(1 + \frac{\rho_f}{\rho_p}\right) \omega_p^t - \frac{\rho_f}{\rho_p} \omega_p^{t-1} + I_p^{-1} \left[-\sum_{L_p} (X^t - X_p^t) \times F^L \Delta S_s \right] \Delta t \qquad (4.55)$$

where I is the inertia tensor of the particle.

After obtaining information of both translation and rotation velocity in the particle's center of mass is possible to update the velocity of the nodes that create the particle as:

$$U_n^{t+1} = U_p^{t+1} + \omega_p^{t+1} \times \left(X_n^{t+1} - X_p^{t+1}\right) \qquad (4.56)$$

as well its position:

$$X_n^{t+1} = X_p^{t+1} + R \left(X_n^t - X_p^t\right) \qquad (4.57)$$

where R is the rotation matrix around the rotation axis.

4.5.2 Particle Collision

When two or more particles are modeled in the same spatial domain, it must compute how they will interact with each other. If no particle collision treatment is done, the boundary of two or more bodies will penetrate each other. A repulsive force is added when the distance between two particles is less than a threshold distance in order to avoid the particles to occupy the same space. Feng and Michaelides (2005) proposed a force term for spherical particles as:

$$
\boldsymbol{F}_{ij}^{P} = \begin{cases} \left[\frac{c_{ij}}{\epsilon_p} \left(\frac{\|\boldsymbol{x}_i - \boldsymbol{x}_j\| - R_i - R_j - \zeta}{\zeta} \right)^2 + \frac{c_{ij}}{E_p} \frac{R_i + R_j - \|\boldsymbol{x}_i - \boldsymbol{x}_j\|}{\zeta} \right] \left(\frac{\boldsymbol{x}_i - \boldsymbol{x}_j}{\|\boldsymbol{x}_i - \boldsymbol{x}_j\|} \right), & \|\boldsymbol{x}_i - \boldsymbol{x}_j\| \leq R_i + R_j \\[4mm] \frac{c_{ij}}{\epsilon_p} \left(\frac{\|\boldsymbol{x}_i - \boldsymbol{x}_j\| - R_i - R_j - \zeta}{\zeta} \right)^2 \left(\frac{\boldsymbol{x}_i - \boldsymbol{x}_j}{\|\boldsymbol{x}_i - \boldsymbol{x}_j\|} \right), & R_i + R_j < \|\boldsymbol{x}_i - \boldsymbol{x}_j\| \leq R_i + R_j + \zeta \\[4mm] 0, & \|\boldsymbol{x}_i - \boldsymbol{x}_j\| > R_i + R_j + \zeta \end{cases}
$$

$$(4.58)$$

where R_i and R_j are the radii of the spheres pair i and j respectively, $\boldsymbol{x}$ is the position of the sphere's center, ζ is the threshold distance for the force act, c_{ij} is the force scale, ϵ and E_p is the stiffness collision parameters for field force and overlapping, respectively. In order to model the particle collision with a wall, virtual sphere is placed symmetrically on the other side of it, then the collision is performed if the critical distance is satisfied . The definitions for scale and stiffness parameters are described in the work of Glowinski et al. (2001). The behavior of the collision force based on its parameters is represented in Fig. 4.8 as a function of the penetration distance δ.

Figure 4.8 – Magnitude of the collision force as a function of penetration distance and calibration parameters.
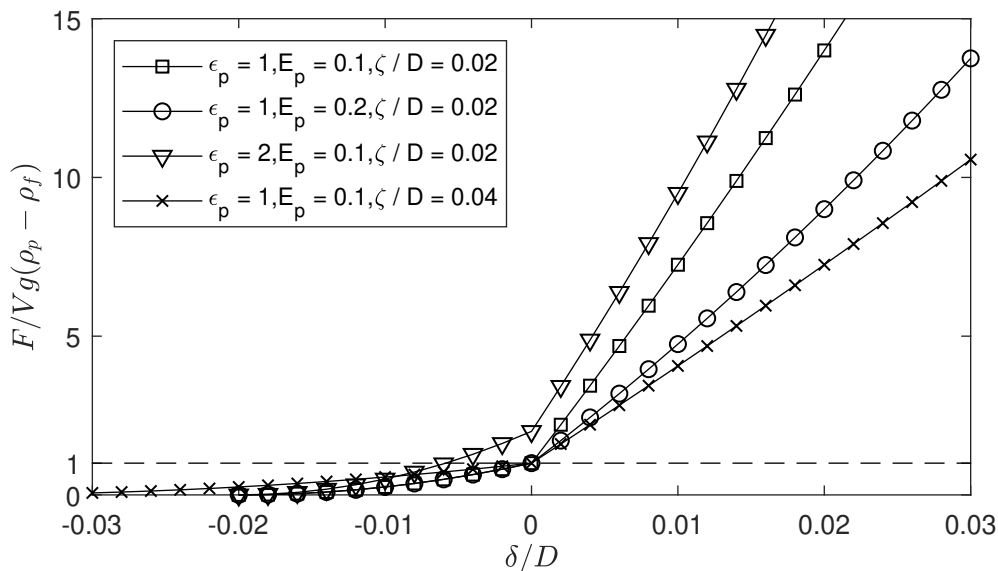
Source: Own elaboration.

When $\delta/D > 0$ it will represent an overlap of the particles, while for $\delta/D < 0$, there will be no collision. The component c_{ij} is chosen to be equal buoyancy force, $\forall g (\rho_p - \rho_f)$, like in the work Feng and Michaelides (2004). The adoption of this value and $\epsilon_p = 1$ permit that when the particle

is at rest in the floor, no penetration will be perceived. The reason is that the collision force acting will be equal to the difference between buoyancy and gravitational forces acting in the particle. The coefficient E_p will dictate the elastic behavior of the material when an overlap of the particles occurs. Meanwhile, ζ will represent the area of effect for the collision force and the allowed penetration. Due to the force being configured in this format, special care is necessary with the relative velocity of the particles. High velocity can cause a high penetration, leading to a high collision force and consequently causing instabilities. Two solutions are possible to avoid this problem: reduce the time step or increase the value of ζ.

4.6   Coupling between methods

The proposed numerical scheme uses different methods to model the settling of a particle in a thixo-viscoplastic fluid. So it is expected that some coupling occurs between the main equations, which will mainly occur by forces. First, the coupling between the immersed particle and the fluid occurs through a body force term imposed by the Lagrangian nodes in Eq. 4.12 and 4.18. In the opposite direction, the fluid velocity will affect the immersed boundary through Eq. 4.47. The influence of the mass/momentum transport in the transport of λ occurs through Eq. 4.28. With the inverse direction taking a longer path, where it first defines the new relaxation frequency, Eq. 4.33, that is used in the majority of the LBM equations. In Eq. 4.33 there is another coupling, where $|T|$ will depend on the body force applied to the fluid, which can originate from the IBM.

4.7   Algorithm

The computational routine developed to resolve the numerical method previously described is elucidated in Fig. 4.9. Each step is described as:

1. **Parameters Initialization**: Domain size is defined. Macroscopic parameters ρ , $\boldsymbol{u}$ and λ are initialized with an initial value. Lattices are populated with equilibrium distribution function. Boundary conditions are defined. Particles are converted into a set of Lagrangian nodes.

2. **Collision**: The collision step is performed according to Eq. 4.10. The collision step for the structural parameter is also performed.

3. **Streaming** : The streaming step is performed according to Eq. 4.11. The streaming step for the structural parameter is also performed.

4. **Boundary Conditions**: Depending on the lattice locations, the populations are recalculated based on which boundary conditions are imposed.

5. **Macroscopic**: Both ρ and $\boldsymbol{u}$ are calculated based on Eq. 4.12 and λ according to 4.29.

6. **IBM**: If an immersed boundary is presented:

   a) **Velocity Interpolation**: The velocity on the Lagrangian is defined according to Eq. 4.46

   b) **Lagrangian Force**: The Lagrangian force is calculated based on Eq. 4.47.

c) **Eulerian Force**: With the force in the Lagrangian nodes defined, it is spread to lattices Eq. 4.48.

d) **Velocity Update**: With the force defined, the velocity for the Eulerian system can be updated using the Eq. 4.49 followed by the spread to the Lagrangian velocities, Eq. 4.50

e) **Convergence**: If the sub-iteration is over a limit of steps, it proceeds to the next time step, otherwise, it resumes to step 6.a

f) **Particle Collision**: If a particle collides, the force defined by Eq. 4.58 is applied.

g) **Particle Position Update**: With all forces defined in the particle, the positions of the Lagrangian nodes are updated according to Eq. 4.52 – 4.57.

7. **Stress Tensor**: With all populations and forces defined over the fluid space, the stress tensor is calculated based on Eq. 4.22.

8. **Calculate $D\lambda/Dt$**: With the stress tensor determined, the rate of change of the structural parameter is calculated based on the kinetic equation that relates both breakdown and build-up, RHS of Eq. 4.25.

9. **Calculate η**: With the structural parameter and stress tensor determined, the value of the apparent viscosity is calculated, consequently the relaxation frequency based on Eq. 4.24.

10. **Stop Criterion**: For transient problems, the simulation ends with a fixed number of time-steps, which will depend on the problem conditions. If the max duration is not reached, it returns to step 2 on a new time step.

Chapter Summary

In this chapter, it was presented the mathematical and numerical models. It was exposed the discrete equations necessary for the lattice Boltzmann method and immersed boundary method. Regarding the particle dynamics, the equations and collision models utilized were presented. Finally, the algorithm design to build the numerical model was explained. In the next chapter, preliminary verification studies will be presented.

Figure 4.9 – Algorithm flowchart.
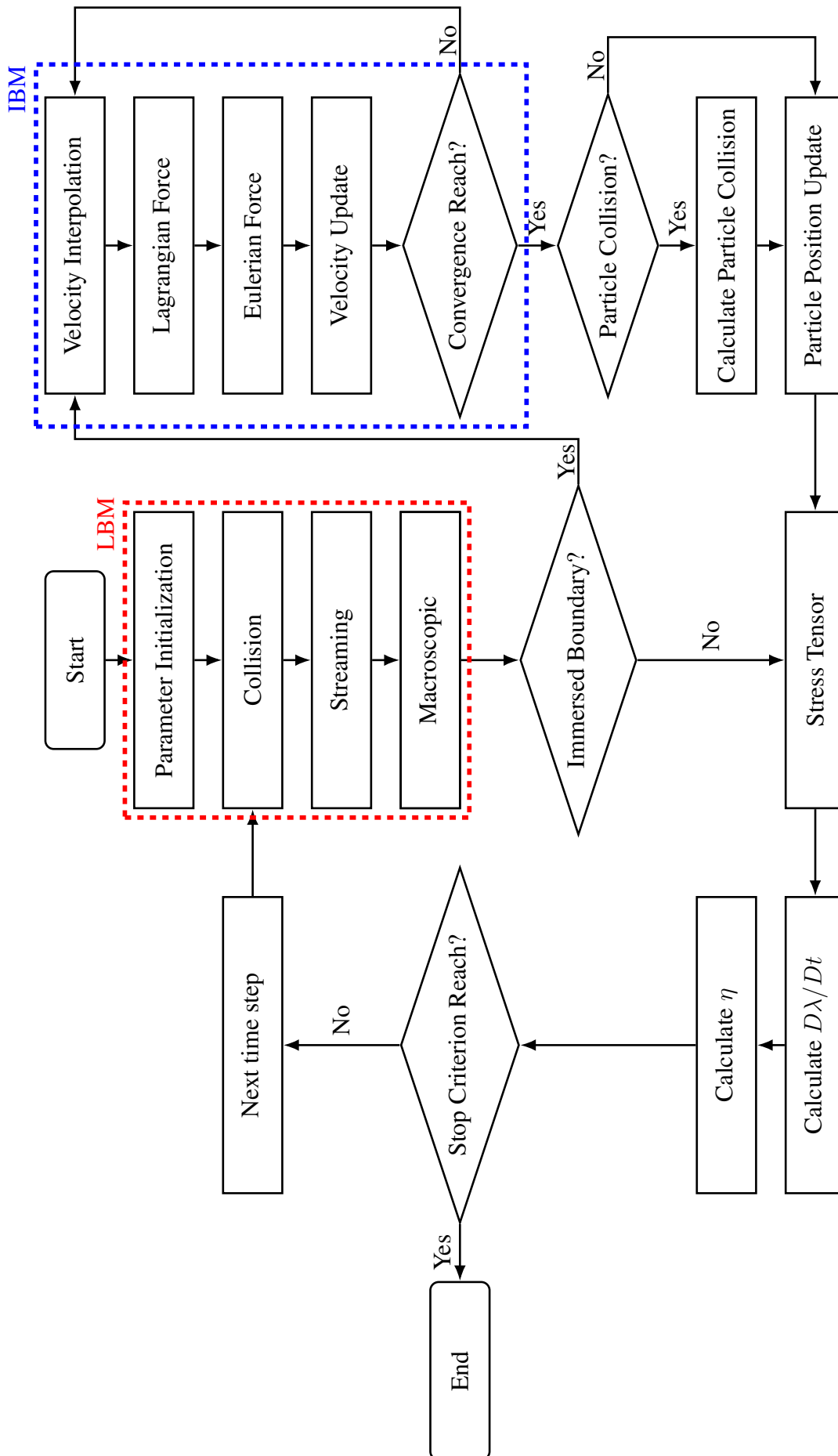
5 VALIDATION TESTS

In order to ensure reliability in the developed algorithm is necessary to compare its results with already consolidated studies in the literature. The first section presents the results for Newtonian fluids, where the numerical code is compared with the analytical solution for two–dimensional Hagen–Poiseuille flow in a circular duct. Next, the analysis of the drag coefficient over a sphere in a channel is used to understand the meshing for the Langrangian nodes. Then, the particle movement is assessed by the settling of one sphere in a closed domain. The test is also used to determine the number of sub-iterations. The second section presents the results for non-Newtonian fluids. Here, the Hagen–Poiseuille solution for Power-Law, Bingham, and Thixotropic fluids is utilized to assess the non-Newtonian implementation. Finally is analyzed the effect of diffusion factor in the advection-diffusion transport equation for the structural parameter.

5.1 Newtonian Fluid

5.1.1 Hagen–Poiseuille Duct Flow

The first test to assess the method's accuracy is the Hagen–Poiseuille fluid flow inside a circular duct. A schematic of the problem is represented in Fig. 5.1, the dots represent the Langrangian nodes of the IBM and the black square is the frontier of the LBM domain:

Figure 5.1 – Schematic representation of the Hagen–Poiseuille flow in a circular duct.
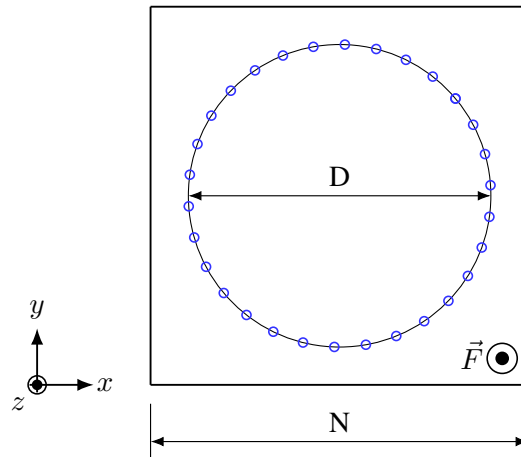
Source: Own elaboration.

A cylindrical immersed boundary with diameter D is placed centered inside a square-shaped domain with sizes $L \times L \times L/8$. A constant force field, represented by the vector $\vec{F}$ leaving the plane in the Fig. 5.1, is applied in the z-direction to start the flow. The velocity of the immersed boundary nodes is set to be equal to 0, to model a stationary wall. Meanwhile, the boundaries of the rectangular domain are set periodic in the z-direction and for the walls parallel to the force is utilized the halfway bounce-back. The purpose of this verification is to assess the error convergence rate of the implemented immersed

boundary method. For this, the quadratic error norm is utilized (PENG et al., 2019), defined as:

$$L_2 = \sqrt{\frac{\sum \left(q_{num} - q_{ref}\right)^2}{\sum \left(q_{ref}\right)^2}} \tag{5.1}$$

where q_{num} is the value of the numerical results, evaluated only inside the duct, and q_{ref} is the reference value, which for this problem is the analytical solution. The simulations are conducted with $\tau = 0.9$, $\epsilon = 0.8$, sub-iteration convergence criteria is used 30 sub-timesteps, which is based on the results of Dash et al. (2014), and using the kernel ϕ_4. The ratio between the Eulerian mesh and Langragian mesh size ($\mathcal{R}$) was evaluated for values of 0.5, 1, and 2. The dimensional values, number of Lagrangian nodes for each mesh ratio, force magnitude, and time-steps are presented in Table 5.1 and the L_2 error as a function of the mesh refinement showed in Fig. 5.2.

Table 5.1 – Dimensional parameters utilized for the circular Hagen–Poiseuille flow.

$N_x \times N_y \times N_z$	D	$\mathcal{R} = 0.5$	$\mathcal{R} = 1$	$\mathcal{R} = 2$	$|\vec{F}|$	Time Steps
$32 \times 32 \times 4$	25	4710	936	521	1.00×10^{-4}	2000
$64 \times 64 \times 8$	50	9420	2512	702	2.50×10^{-5}	8000
$128 \times 128 \times 16$	100	28 888	7536	2041	6.25×10^{-6}	32 000
$256 \times 256 \times 32$	200	97 968	25 120	6594	1.56×10^{-6}	128 000

Source: Own elaboration.

Figure 5.2 – Quadratic error norm L_2 for a Poiseuille duct flow with different meshes ratios.
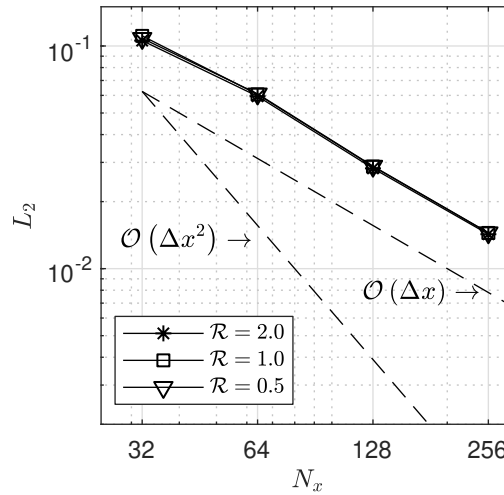
Source: Own elaboration.

According to the results, the decay error is strongly dependent on the lattice numbers. The error decay has an order of approximately $\mathcal{O}(\Delta x)$. The result agrees with the analysis and findings of Peng et al. (2019), where IBM is only first-order accurate for this case. Refining the Lagrangian mesh did not have a significant improvement in the accuracy. One possible explanation is that the flow does not have a velocity component perpendicular to the mesh. Hence there is no fluid penetration in the Lagrangian mesh. The velocity magnitude for the case where the mesh is $128 \times 128 \times 16$ is displayed in Fig. 5.3.

Figure 5.3 – Velocity contour of the flow inside a circular duct formed by IBM (white circle) inside a squared domain. $N_x = N_y = 128$, $N_z 16$ and $\mathcal{R} = 1$. The red dashed circles delimit the kernel influence area.
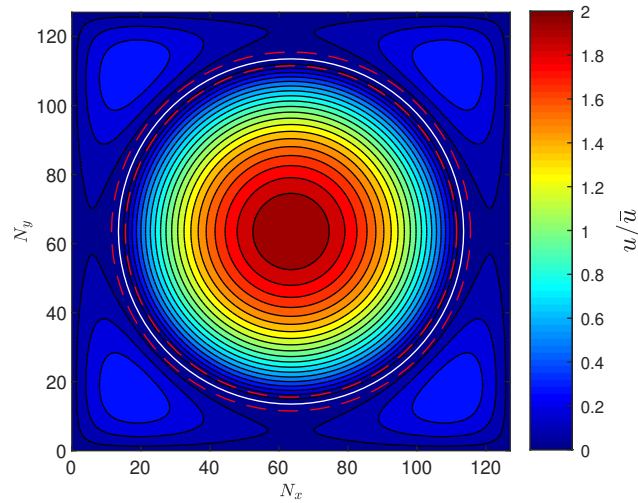
Source: Own elaboration.

The Lagrangian mesh used for the IBM is represented by the white circle, with its inner radius being coincident with the nodes. Inside the duct, the fluid velocity exhibit the parabolic profile with its maximum velocity being in agreement with the analytical solution. It can seem that still exists a flow in the region between the Lagrangian nodes and the domain frontier, which is a consequence of the force field affect all domain. The presence of this flow was reported by Peng et al. (2019) when using the same boundary conditions.

5.1.2 Fixed Sphere

The second verification test for the immersed boundary method is the laminar flow over a stationary sphere, and it has the objective to understand how spatial discretization affects the force over a spherical particle. In this case, the sphere is positioned in a square channel, according to Fig. 5.4:

Figure 5.4 – Geometry of the flow around a fixed sphere.
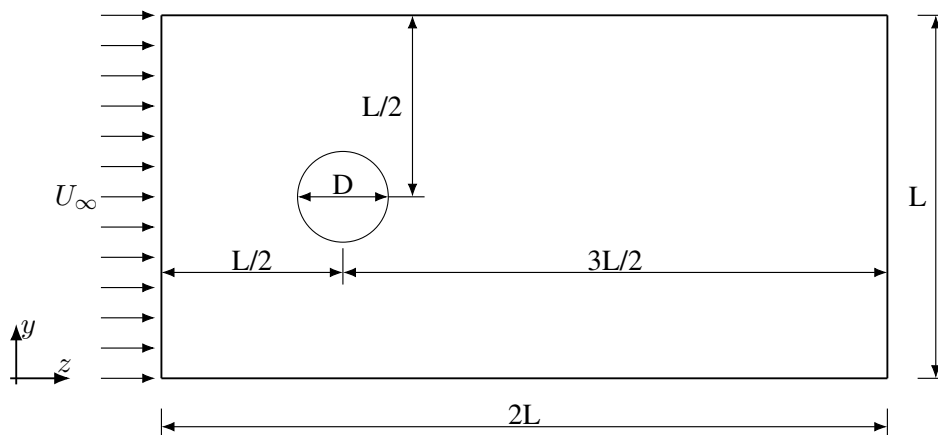
Source: Own elaboration.

The sphere with diameter D is positioned in the channel's centerline at a distance $L/2$ from the inlet, the channel has dimensions of $L \times L \times 2L$. In the inlet, a prescribed velocity U_∞ is imposed with half-way bounce back method, Eq. 4.21. For the outlet, the same inlet uniform velocity is applied, since in preliminary tests it only started to affect the significantly when the domain length was lower than 1.5D. Meanwhile, for other boundaries, the free-slip condition is utilized, Eq. 4.20. Details for spherical mesh construction can be found in Appendix C.

Due to hardware constraints was not possible to execute simulations without the wall stop affecting the solution. Hence three blockage ratios (D/L) are evaluated: $1/3$, $1/4$, and $1/6$. Three Reynolds numbers were evaluated with the different blockage ratios: 7.5, 100, and 300, with four mesh refinements, $D = 10, 20, 30$, and 40 lattice units. The values for U_∞ and τ are shown in Table 5.2.

Table 5.2 – Simulation parameters utilized for the drag of a fixed sphere.

D	U	τ	Re_D	D/L
10	0.1			1/3
20	0.05	0.9	7.5	1/4
30	0.033			1/6
40	0.025			
10	0.1			1/3
20	0.05	0.53	100	1/4
30	0.033			1/6
40	0.025			
10	0.1			1/3
20	0.05	0.51	300	1/4
30	0.033			1/6
40	0.025			

Source: Own elaboration.

Figure 5.5 depicts the results for the drag coefficient as a function of the Reynolds number, the mesh refinement and the inverse of blockage ratio (D/L). For the Reynolds numbers 7.5 and 100, the drag coefficient converged as the mesh was refined. For the Reynolds number of 300, the coarse mesh with $D = 10$ did not converge, indicating that it is not sufficient to represent the flow structures. Another aspect is that the drag coefficient for $\mathrm{Re}_D = 300$ had a relatively small change with the mesh refinement when compared with the other Reynolds numbers.

With the decrease of the blockage ratio (D/L) the drag coefficient for all evaluated Reynolds numbers approach the values of Morrison's (2016) correlation. Because the fluid is compressed between the sphere and the channel walls leading to a increase of the fluid velocity. Consequently, the friction and the pressure difference between the fore and aft regions of the sphere increases, causing a rise in the drag coefficient. The ratio between the Langrangian and Eulerian mesh is again evaluated, with the results presented in Fig. 5.6.

Increasing the ratio d/h, a coarse Langrangian mesh only promoted a change in the drag coefficient results when the nodes' distance was higher than 2. When the distance was equal or lesser than 2, the lattices are always affected by at least two Lagrangian nodes when utilizing the ϕ_4 kernel. Increasing the separation distance to 3 causes that some lattices will only be affected by one Langragian node, meaning

Figure 5.5 – Drag coefficient for a fixed sphere in a channel for Reynolds numbers a) $Re_D = 7.5$, b) $Re_D = 100$, and c) $Re_D = 300$ with three blockage ratios $L/D = 6$, 4, and 3 as a function of mesh discretization. d) Represents the convergence towards Morrison's (2016) external flow correlation values with $D = 40$ lattices units.
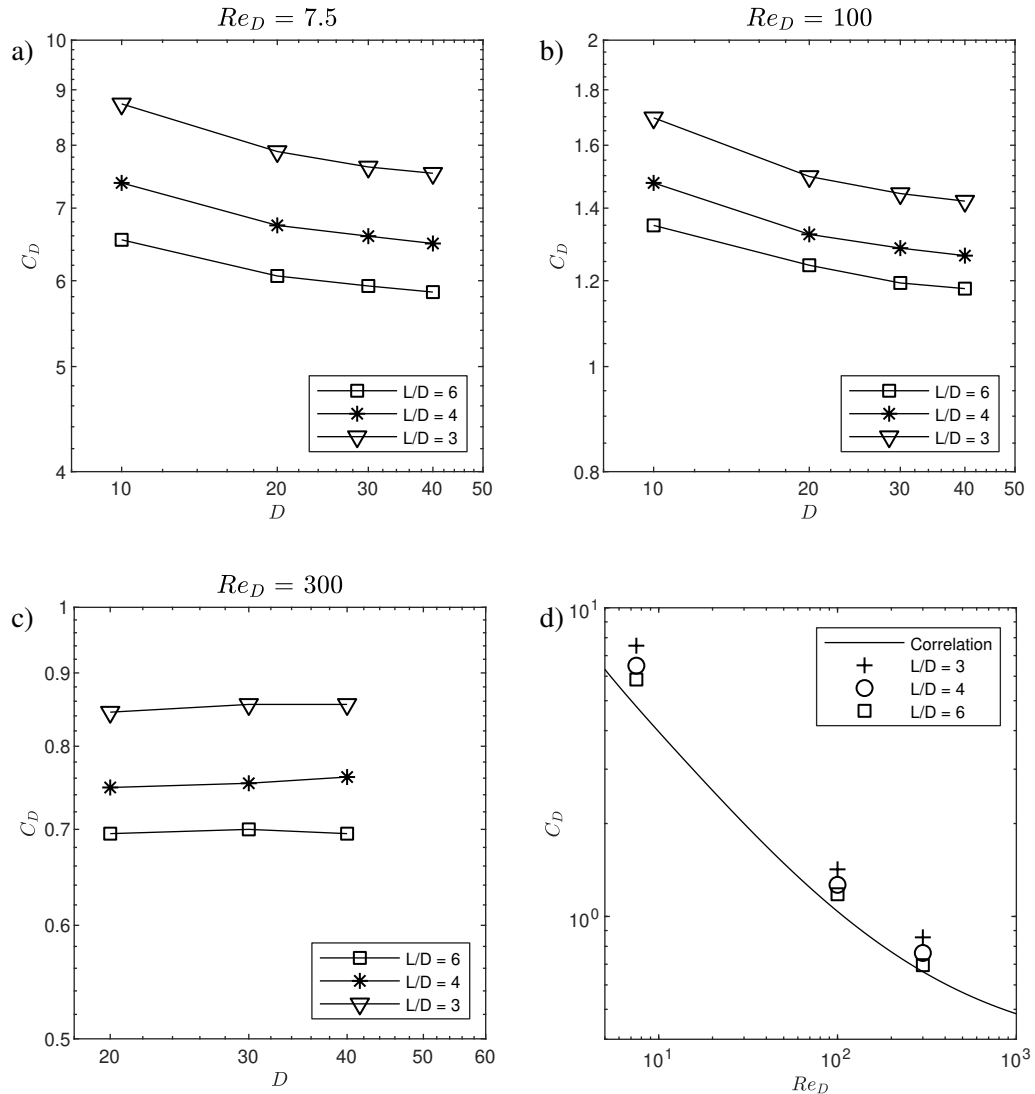
Source: Own elaboration.

that this node is the only responsible for ensuring the non-slip condition in that lattice. Consequently, the force imbalance will be distributed to the neighbor's lattices, leading to numerical errors. Increasing the ratio further will imply that no overlap between the kernels will exist and therefore, the no-slip condition is not satisfied in some nodes. The error increases with the Reynolds number because a higher force is required to be applied to satisfy the no-slip condition.

5.1.3　One particle settling

The dynamic aspect of the immersed boundary method is tested by investigating the settling of one particle in a Newtonian fluid and comparing with the experimental results of Cate et al. (2002). The results for the trajectory and velocity are evaluated for Reynolds numbers ranging from 1.5 to 32. The geometry of Cate et al. (2002) experiment is shown in Fig. 5.7.

Figure 5.6 – Effect of ratio between the lattices size (h) and Langrangian nodes (d) drag coefficient for Reynolds numbers equal to 7.5, 100, and 300.
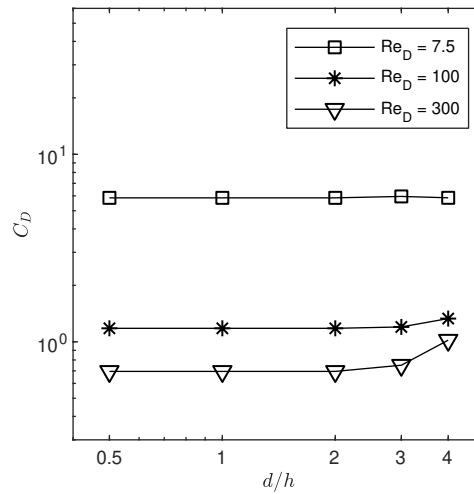
Source: Own elaboration.

Figure 5.7 – Geometry of one particle settling in a Newtonian fluid used by Cate et al. (2002).
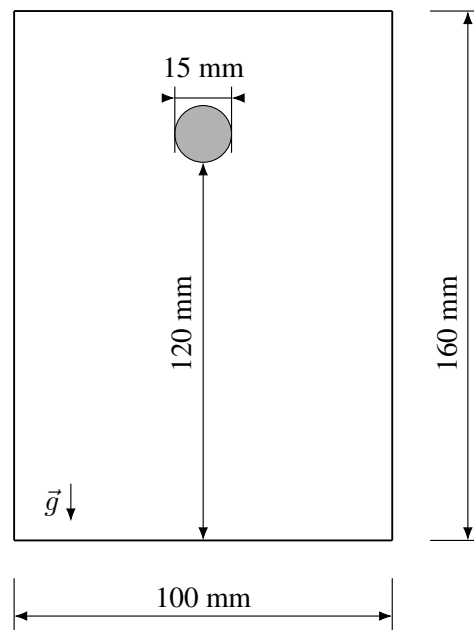
Source: Own elaboration.

Initially, a spherical particle with a diameter equal to $15\,\mathrm{mm}$ and density $1120\,\mathrm{kg\,m^{-3}}$ is positioned at $120\,\mathrm{mm}$ from the bottom of a rectangular tank. The tank has dimensions of $100\,\mathrm{mm} \times 100\,\mathrm{mm} \times 160\,\mathrm{mm}$ and it is filled with Newtonian fluid. The half-way bounce-back method is used as a boundary condition for all the domain frontier. Three meshes with different degrees of refinement are utilized: $1\,\mathrm{mm}$, $0.66\,\mathrm{mm}$, and $0.5\,\mathrm{mm}$. The fluid properties and the simulation parameters for the coarse mesh $\Delta x = 1\,\mathrm{mm}$ are exhibited in Table 5.3. The procedure to determine the simulation's parameters for the other meshes can be found in Appendix B.

The number of sub-iterations in the immersed boundary method is the first test performed. The test

Table 5.3 – Fluid properties and simulation parameters for $\Delta x = 1\,\mathrm{mm}$

Case	Re_D	$\rho_f\,[\mathrm{kg\,m^{-3}}]$	$\mu_f[\mathrm{Pa\,s}]$	τ	$\Delta t\,[\mathrm{s}]$	g^*
1	1.5	970	0.373	0.90	3.47×10^{-4}	1.18×10^{-3}
2	4.1	965	0.212	0.90	6.07×10^{-4}	3.61×10^{-3}
3	11.6	962	0.113	0.80	8.51×10^{-4}	7.11×10^{-3}
4	31.9	960	0.058	0.65	8.28×10^{-4}	6.72×10^{-3}

Source: Own elaboration.

employed the parameters of case 4 with 1, 2, and 3 sub-iterations. The particle sedimentation velocity results are exposed in Fig. 5.8. There was no perceived difference in the particle velocity when increasing

Figure 5.8 – Effect of the number sub-iterations performed (m) in the immersed boundary method for case 4.
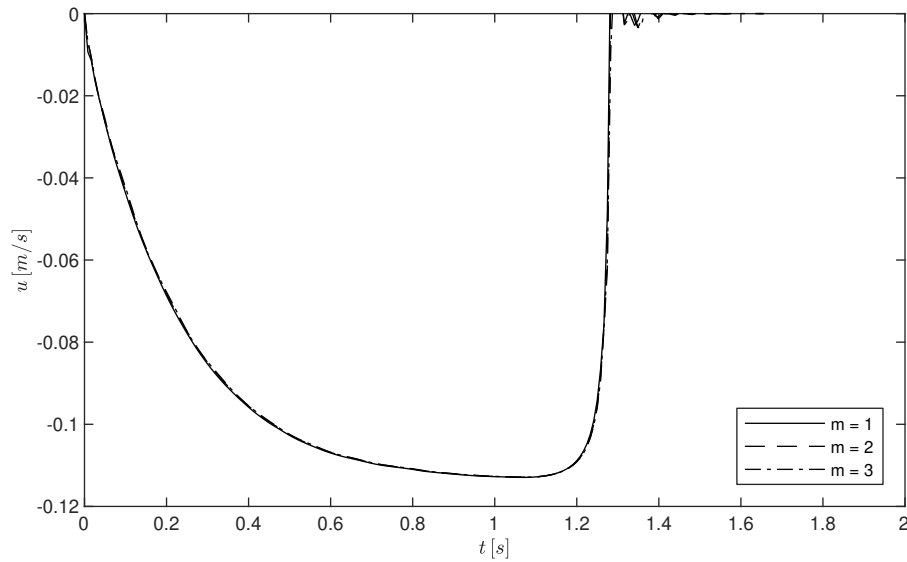
Source: Own elaboration.

the number of sub-iterations and a 0.1% difference in the maximum terminal velocity. With only 714 Lagrangian nodes the simulation speed suffered a 20% performance impact when going from 1 to 3 sub-iterations, 77.7 MLUPS[1] versus 63.4 MLUPS, respectively. The performance is expected to decrease as the number of Lagrangian nodes increases as well as increasing the number of sub-iterations. Based on these results and considering the performance impacts, the simulations for particle settling will use just one sub-iteration.

The next test is the verification of the numeric results with the experimental data of Cate et al. (2002). The particle velocity and trajectory as a function of the time for the cases, listed in Table 5.3, are exposed in Fig. 5.9 and Fig. 5.10.

As the mesh is refined, the results lean toward the experimental data of Cate et al. (2002), demonstrating that the code so far is satisfactorily capable of predicting the settling behavior of a spherical particle in a reasonable range of Reynolds numbers.

---

[1]   MLUPS stands for Million lattices updates per second.

Figure 5.9 – Comparison between the numeric and experimental results of Cate et al. (2002) of the particle velocity with three mesh refinements. Black: $\Delta x = 1\,\mathrm{mm}$; Red: $\Delta x = 0.66\,\mathrm{mm}$; Blue: $\Delta x = 0.5\,\mathrm{mm}$.
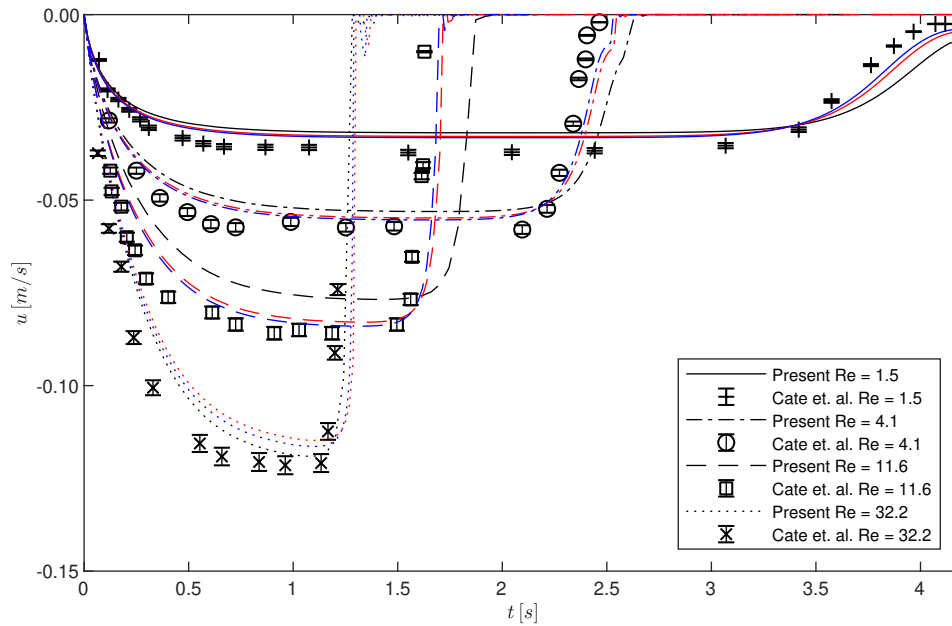
Source: Own elaboration.

5.2 Non-Newtonian Fluids

5.2.1 Power-Law and Bingham Hagen-Poiseuille Flow

The first validation with non-Newtonian is the Hagen-Poiseuille flow between two infinite planes. The geometry of this problem is represented in Fig. 5.11. The no-slip boundary condition in the walls is formulated based on the half-way bounce-back method. The rest of the domain frontier is set as periodic conditions to create the aspect of an infinite plate. With the fluid initially at rest, a body force is applied to start the flow. After a sufficient period, a steady-state is achieved.

Two fluid models are initially evaluated: Power-Law and Bingham and its velocity profile are compared with the analytical solution for this flow (BIRD and STEWART, 2002). For the Power-Law model, the domain size is fixed at $64{\times}64{\times}4$ lattices. The fluid is initialized with $\tau = 0.6$ and one million time-steps are performed to ensure a steady-state solution. Three Power-Law indexes are evaluated: 0.5, 1.0, and 1.5. Each of the Power-Law indexes has a corresponding body force of 10^{-4}, 10^{-5}, and 10^{-7}, respectively. The velocity profile results are shown in Fig. 5.12. The results show that the model can represent both shear-thickening and shear-thinning behaviors.

Next, the Bingham model is evaluated for this Hagen-Poiseuille flow. The L_2 error is evaluated for four Bingham numbers: 0, 0.23, 0.34, and 0.45. Like the Power-Law fluid, a body force is applied in the fluid and has a value of 10^{-5}. Only the yield-stress of the fluid is then modified in order to assess different Bingham numbers, The yield-stress values, as well as the respective domain size and L_2, errors are exposed in Table 5.4.

Figure 5.10 – Comparison between the numeric and experimental results of Cate et al. (2002) for the particle trajectory with three mesh refinements. Black: $\Delta x = 1\,\text{mm}$; Red: $\Delta x = 0.66\,\text{mm}$; Blue: $\Delta x = 0.5\,\text{mm}$.
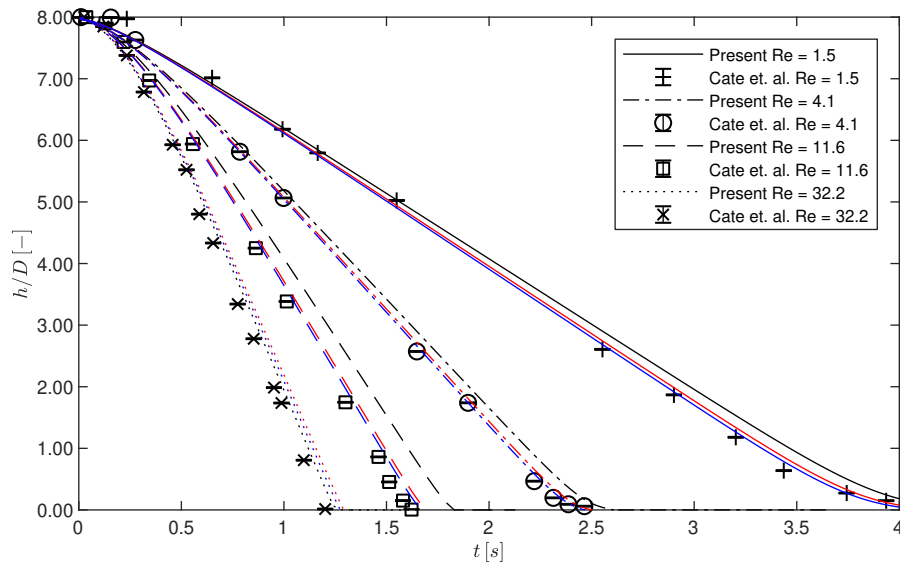
Source: Own elaboration.

Figure 5.11 – Schematic representation of Hagen-Poiseuille flow between two parallel plates.
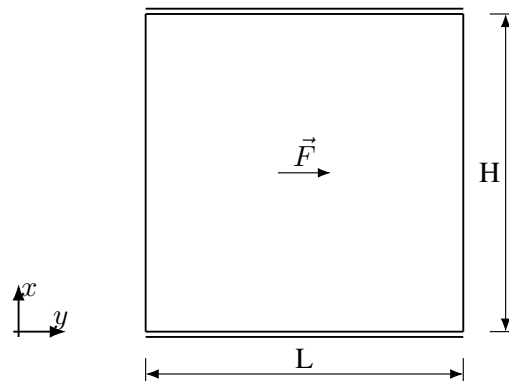
Source: Own elaboration.

Table 5.4 – Fluid properties and simulation parameters for Bingham channel flow.

Bn	Domain	τ_y	L_2
0.00	64×64×4	0.00×10^{-4}	0.02%
0.23	64×64×4	1.44×10^{-4}	0.18%
0.34	128×128×4	2.16×10^{-4}	0.57%
0.45	256×256×4	2.89×10^{-4}	0.72%

Source: Own elaboration.

The steady-state condition is then satisfied after performing one million time steps. For this flow, a Bingham number of 0.5 corresponds to channel flow plugged. The velocity profiles as a function of the Bingham numbers are shown in Fig. 5.13.

Figure 5.12 – Comparison between the obtained numerical results and the analytical solution of the steady-state velocity profile for Power-Law fluid between two infinite plates with three Power-law index.
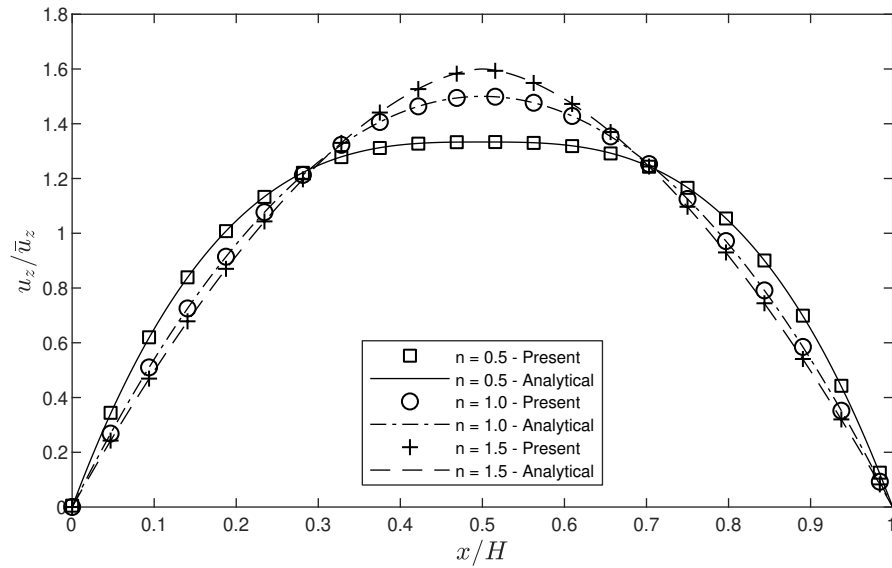
Source: Own elaboration.

Figure 5.13 – Comparison between the obtained numerical results and the analytical solution of the steady-state velocity profile for Bingham fluid between two infinite plates with four Bingham numbers.
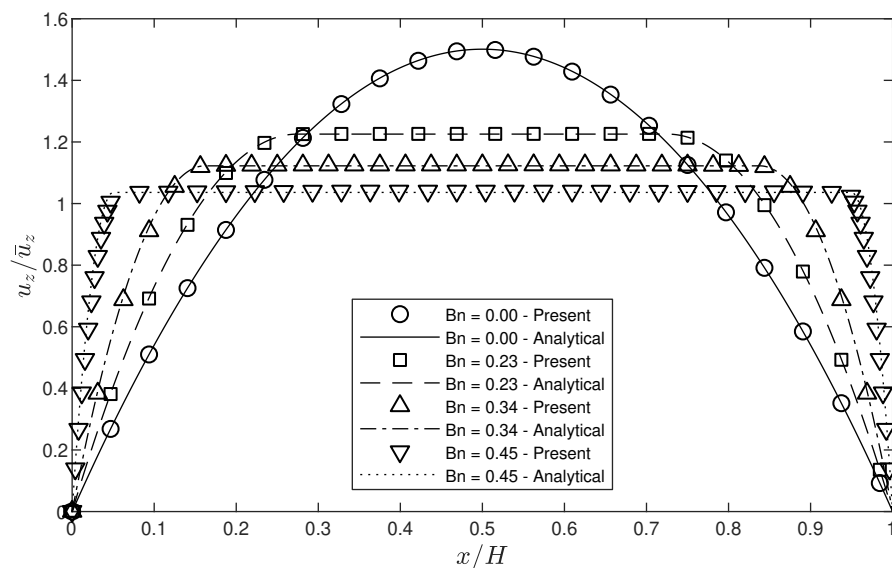
Source: Own elaboration.

The domain size was increased for higher Bingham numbers to obtain a stable simulation. The increase in the domain size was necessary because, near the walls, there is a high-velocity gradient, where a small number of lattices are not capable of modeling it correctly. The results demonstrate that the algorithm is also capable of model fluids that have yield stress.

5.2.2 Drag in Bingham fluid

In this subsection, the analysis of drag around a fixed sphere is extended for a Bingham fluid. Similar to the Newtonian case, the sphere is positioned in the center of a rectangular channel. However, in this case, the sphere is located midway between the inlet and outlet. For the boundary conditions are the similar to the Newtonian case: Fixed velocity in the inlet and outlet, but with the remain frontiers with a free-slip condition. The numeric results will be compared with the data obtained by the finite element method of Blackery and Mitsoulis (1997). The domain utilized was $8D \times 8D \times 8D$, with the sphere's diameter being 30 lattice units. τ is kept constant at 0.8, implying an inlet velocity and walls of 3×10^{-3} for a Reynolds number of 1. In order to assess the method the Stokes' drag coefficient is utilized, which is defined as (BERIS et al., 1985):

$$\mathrm{C}_D = \frac{F}{6\pi\eta U R} \tag{5.2}$$

The results for the drag coefficient are presented in Table 5.5. The errors are relatively small, considering the mesh refinement utilized, bounded due to memory constraints. The errors could also be associated with the low flow velocity necessary to achieve the small Reynolds number and close to zero in the sphere surface. The small velocity is known for causing convergence problems in the regularized lattice Boltzmann method (MATTILA et al., 2017).

Table 5.5 – Stokes' drag coefficient for a fixed sphere in a Bingham fluid.

Bn	0	2.25	9.90	27	90
Present	1.33	6.69	19.3	44.7	131.3
Blackery and Mitsoulis (1997)	1.35	6.04	18.9	44.19	126.4
$\lvert (\theta - \theta_{ref})/\theta_{ref} \rvert \times 100\%$	0.97%	10.8%	2.26%	1.21%	3.87%

Source: Own elaboration.

Another important aspect of this test is to verify the interface between the yielded and unyielded regions of the flow, represented in Fig. 5.14. As the Bingham number decreases, the yielded zone size increases because of the reduced stress necessary to break it. The relative velocity vectors, with the reference in the unyielded fluid, are also represented. The unyielded region produced around the sphere is truncated toroid, the same format obtained by Beris et al. (1985). The zone is continually being built and destroyed as the fluid enters and exits the regions with a higher shear rate. These results follow the existing literature, showing that the method can model both non-Newtonian fluid flows with immersed bodies.

5.2.3 Thixotropic Poiseuille Flow

The Poiseuille flow of Houska's fluid can be used to assess the error decay order of the numerical solution due to the existence of an analytical solution (AHMADPOUR and SADEGHY, 2013). Here, instead of flow inside a circular duct, it is modeled the flow between two infinite parallel plates separated by a distance H. The fluid is initially at rest and unstructured; a body force F is then applied over the domain to initialize the flow. The simulation is carried out until achieving a quasi-steady-state, $\lambda (x = 0) = 0.999$. The analysis is performed for the flow case, where $\mathrm{Bn}_0 = 0.139$, $\mathrm{Bn}_\infty = 0.104$ and $\mathrm{Tx} = 12.8$. The secondary relaxation frequency is varied from 1.25 to 1.99998. The velocity

Figure 5.14 – Velocity vectors (black) and unyielded (gray) / yielded (white) regions for four Bingham numbers a) 2.25, b) 9.90, c) 27, and d) 90 for flow around a fixed sphere and Reynolds number equal to 1. Flow is from bottom to top.
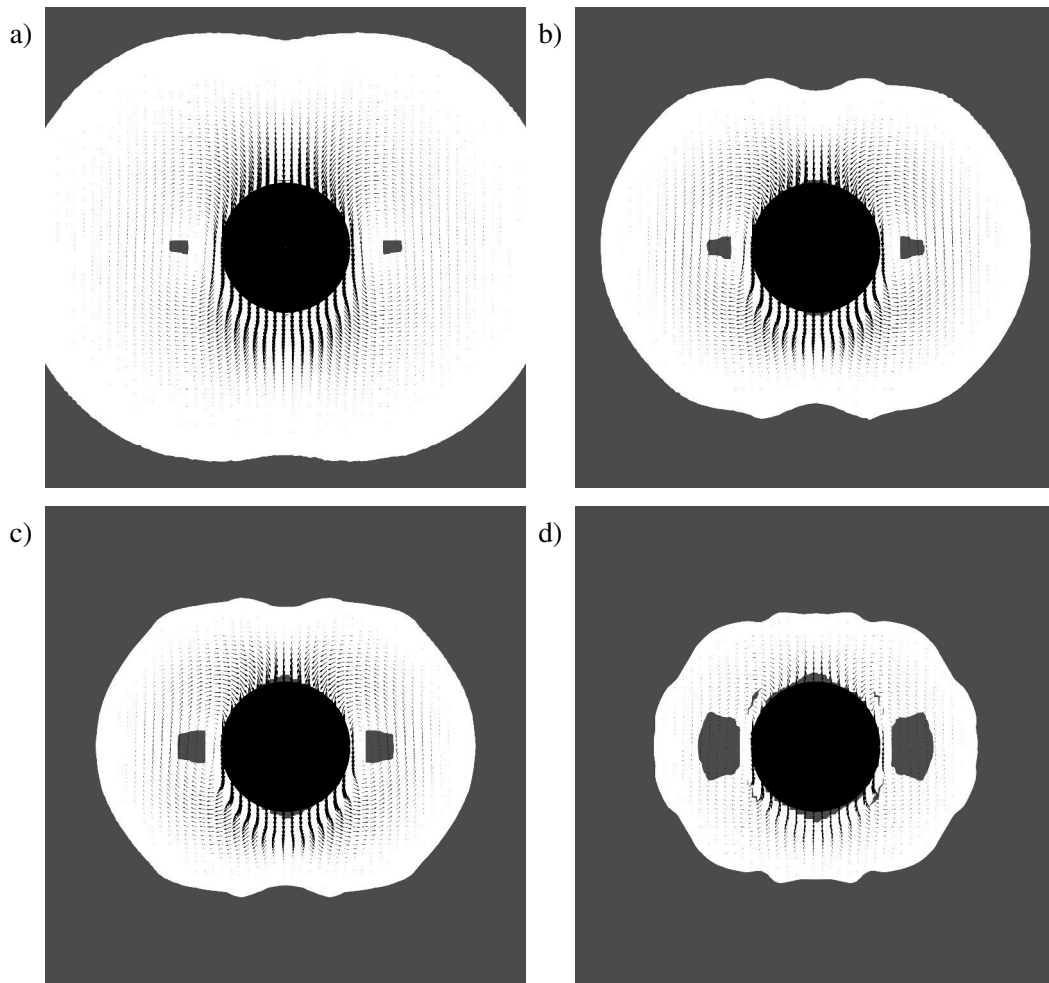
Source: Own elaboration.

scale utilized is $U_0 = FH^2/\eta_p$. The numerical results for the velocity and structural parameter profile represented in Fig. 5.15.a and Fig. 5.15.b respectively show a excellent agreement with the analytical solution, found in Appendix A.

The unyielded zone is well captured, with the structural parameter reaching the value of 0.999 in the "plug" region. As shearing the fluid, the structural parameter rapidly decreases until it reaches the minimal near the wall surface, similar to the results obtained by Ahmadpour & Sadeghy (AHMADPOUR and SADEGHY, 2013). The L_2 error for the velocity and structural parameter field as a function of the mesh discretization, where is the number of cross-section lattices, and relaxation time for the advection-diffusion equation is shown in Fig. 5.16.

Figure 5.15 – Velocity (a) and structural parameter (b) profile for analytical and numerical solutions. $N = 128$, $\mathrm{Bn}_0 = 0.139$, $\mathrm{Bn}_\infty = 0.104$, Tx $= 12.8$.
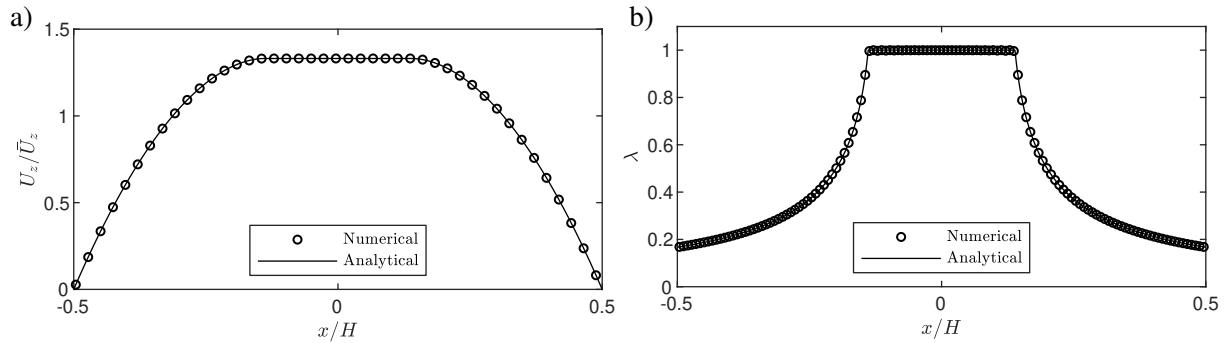
Source: Own elaboration.

Figure 5.16 – L_2-error norm for the Velocity and structural parameter as a function mesh size (a and b) and diffusion coefficient (c and d) respectively.
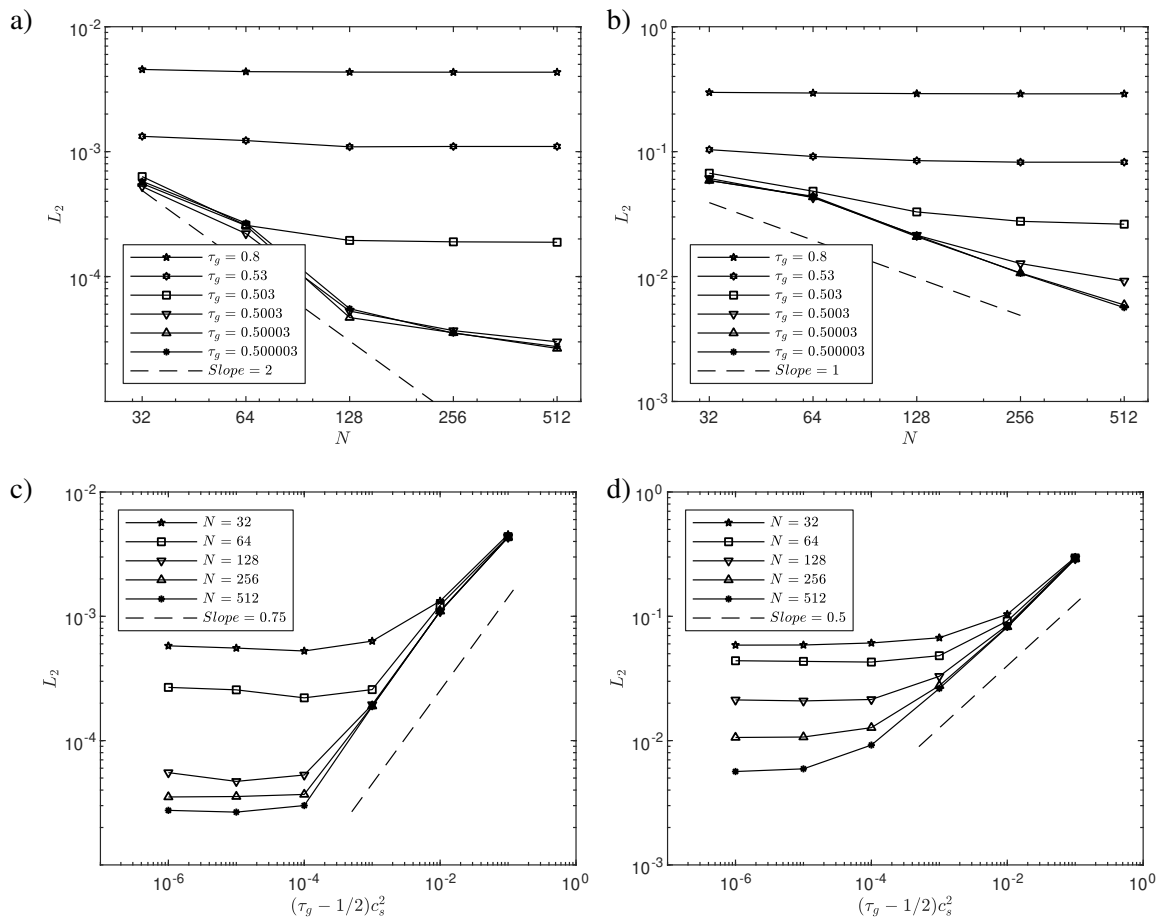
Source: Own elaboration.

When τ_g is sufficiently high (high diffusion coefficient), the error from the numerical diffusion effect surpasses the spatial discretization error when the mesh is refined, indicated by the plateaus. As τ_g reduces, the dominant error is the spatial one, which makes the overall error initially decay with order 2 for the fluid velocity, Fig. 5.16.a, similar to Malaspinas et al. (2010) and Lugarini et al. (2020), and 1 for

the structural parameter, Fig. 5.16.b. But when the diffusion error surpass it, the error decay rate reduces. If the spatial discretization is fixed, the error decay order is approximately 0.75, Fig. 5.16.c, and 0.5, Fig. 5.16.d, for the velocity and structural parameter field when it is varied the diffusion coefficient. In this case, decreasing the relaxation time further, $\tau_g < 0.500\,03$, did not improve the numerical accuracy, similarly to the results of Malaspinas et al. (2010), as instabilities in the λ field started to occur near the yield-surface. Another aspect to point out is that the difference in the error decay orders of fluid velocity and the structural parameter is not problematic since the magnitude order that $\mathfrak{D}$ can be varied is superior to the order range obtained by the spatial discretization. In conclusion, the numerical setup must be such that the spatial discretization error is superior to the diffusion error, which is achieved by choosing a sufficiently high relaxation frequency ($\mathfrak{D} \approx 10^{-5}$).

Chapter Summary

In this chapter, the verification results for the numerical method were presented. First was analyzed the error behavior for Newtonian fluids as a function of mesh parameters. Next was evaluated with the results for non-Newtonian fluids, with particular attention for the viscoplastic behavior. Finally was assessed the inherent error of adopting the advection-diffusion transport equation. The results were considered satisfactory; this allows to conduct the main study of this work: settling in thixo-viscoplastic fluid.

6 RESULTS

Here is presented the results for particle settling in a thixo-viscoplastic fluid. First, the results for a single particle settling, where the influence of the fluid properties in the particle velocity is investigated, divided when the dynamic Bingham number is equal to zero or not. The results are used to propose a correlation for the particle terminal velocity as a function of the Bingham and Thixotropic numbers. All results are presented in dimensionless numbers. The analysis of the dimensionless equations and groups for this problem can be found in Appendix D. Next the analysis is extended for two particles settling in the same type of fluid.

6.1 One particle settling

It is considered a spherical particle with diameter $D = 25$ (lattice units) and a density ratio equal to 2.65, similar to the cuttings encountered during a drilling operation. Initially, the particle center is positioned at $18.75D$ from the bottom in a tank with dimensions $8D \times 8D \times 20D$. The fluid is initially fully unstructured, represented in Fig. 6.1.

Figure 6.1 – Geometry of the one-particle settling study.
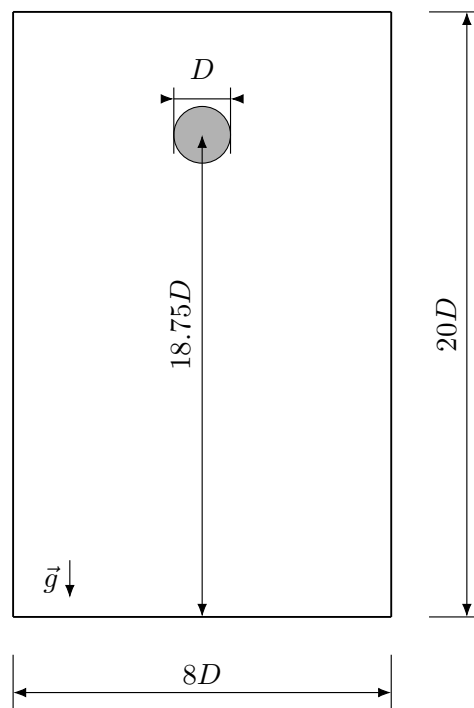
Source: Own elaboration.

The particle is released under the action of gravity and settles towards the bottom. In the present study, focused on the effects of the fluid's rheology, hence the dynamic and static Bingham numbers, as well as the kinetic parameters. Based on the characteristic velocity, the Archimedes number is fixed at 139. The yield stress values, as well as the kinetic parameters, are varied in the present study.

The domain is discretized with $200 \times 200 \times 500$ lattice units, and the spherical particle has a diameter of 25 lattice units. The first relaxation time, responsible for the mass and momentum transport, is kept constant as $1/\omega_p = 0.8$, while the relaxation time for the λ transport equation is $\tau_g = 0.5001$.

6.1.1 Case study $\mathrm{Bn}_\infty = 0$

First, it is analyzed the velocity and structural parameter field for the case where $\mathrm{Bn}_0 = 0.028$, $k_1^* = 2.25$, and $k_2^* = 1/344$. The snapshots of these fields for the times $t^* = 83$ and 334 are represented in Fig. 6.2.

Figure 6.2 – Velocity and structural parameter field for $\mathrm{Bn}_0 = 0.028$, $k_1^* = 2.25$, and $k_2^* = 1/344$ at times $t^* = 83$ and $t^* = 334$.
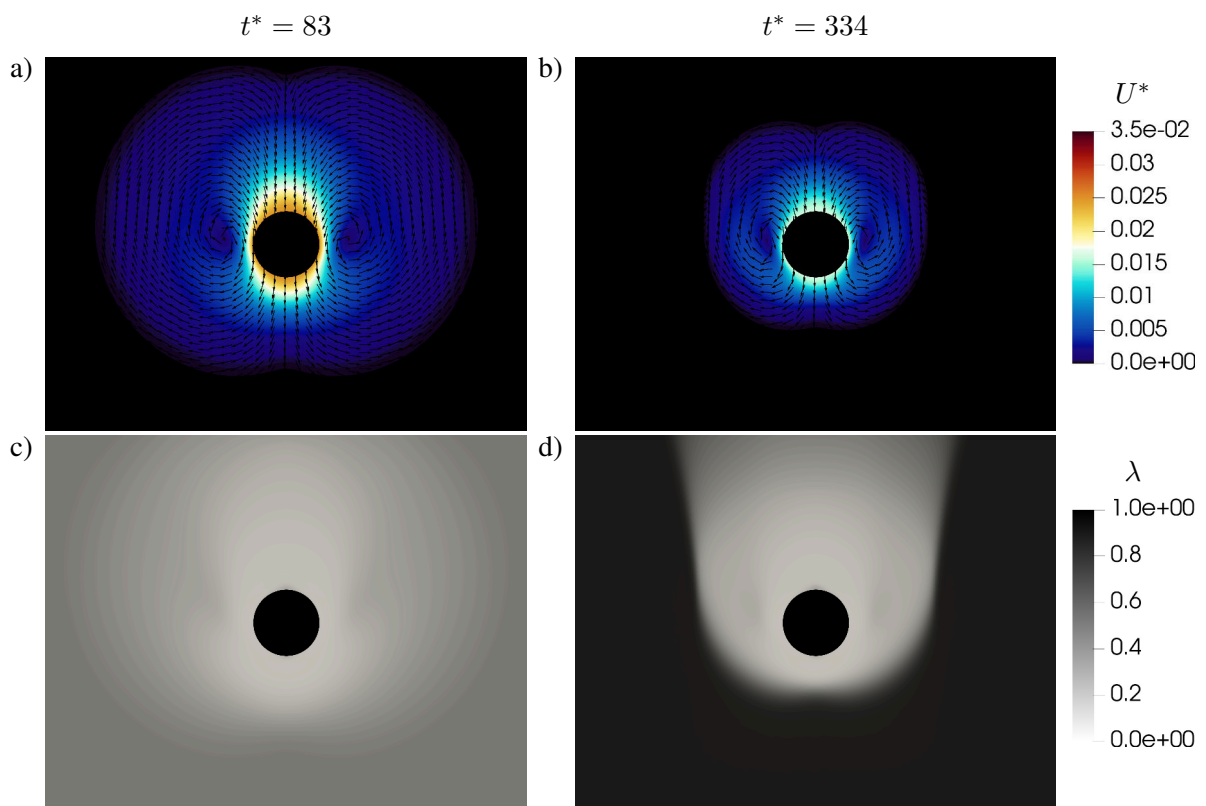
Source: Own elaboration.

The particle accelerates due to the gravitational force in the initial settling moments until it reaches a peak velocity. During this stage, the fluid has an almost homogeneous structural parameter value, Fig. 6.2.c. Consequently, the particle settles with characteristics similar to the Bingham fluid with a low yield-stress value, e.g., the yield-surface acquiring a shape similar to the Bingham fluids. As time passes, the fluid build-up and progressively reduces the yield envelope size around the particle, which can be perceived by the reduced diameter of the unstructured fluid trail behind the particle, Fig. 6.2.b. The sharp interface in the trail of the structural parameter field, Fig. 6.2.d, occurs because the fluid only breaks inside the yield-surface, creating two distinct zones: one where the particle traveled and sheared the fluid (in gray), and another where the fluid did not suffer any kind of shear and only structured itself (in black).

After some time, the particle reaches a quasi-steady-state regime (when the unsheared fluid has $\lambda \approx 0.95$). Here, it is compared two different static Bingham numbers, $Bn_0 = 0.012$ and $Bn_0 = 0.028$, with the same breakdown and build-up parameters, $k_1^* = 2.25$ and $k_2^* = 1/344$. The velocity, shear-rate, and structural parameter field for these two cases are represented in Fig. 6.3.

Figure 6.3 – Velocity, shear-rate, and structural parameter field for $Bn_0 = 0.012$ and $Bn_0 = 0.028$ with $k_1^* = 2.25$ and $k_2^* = 1/344$.
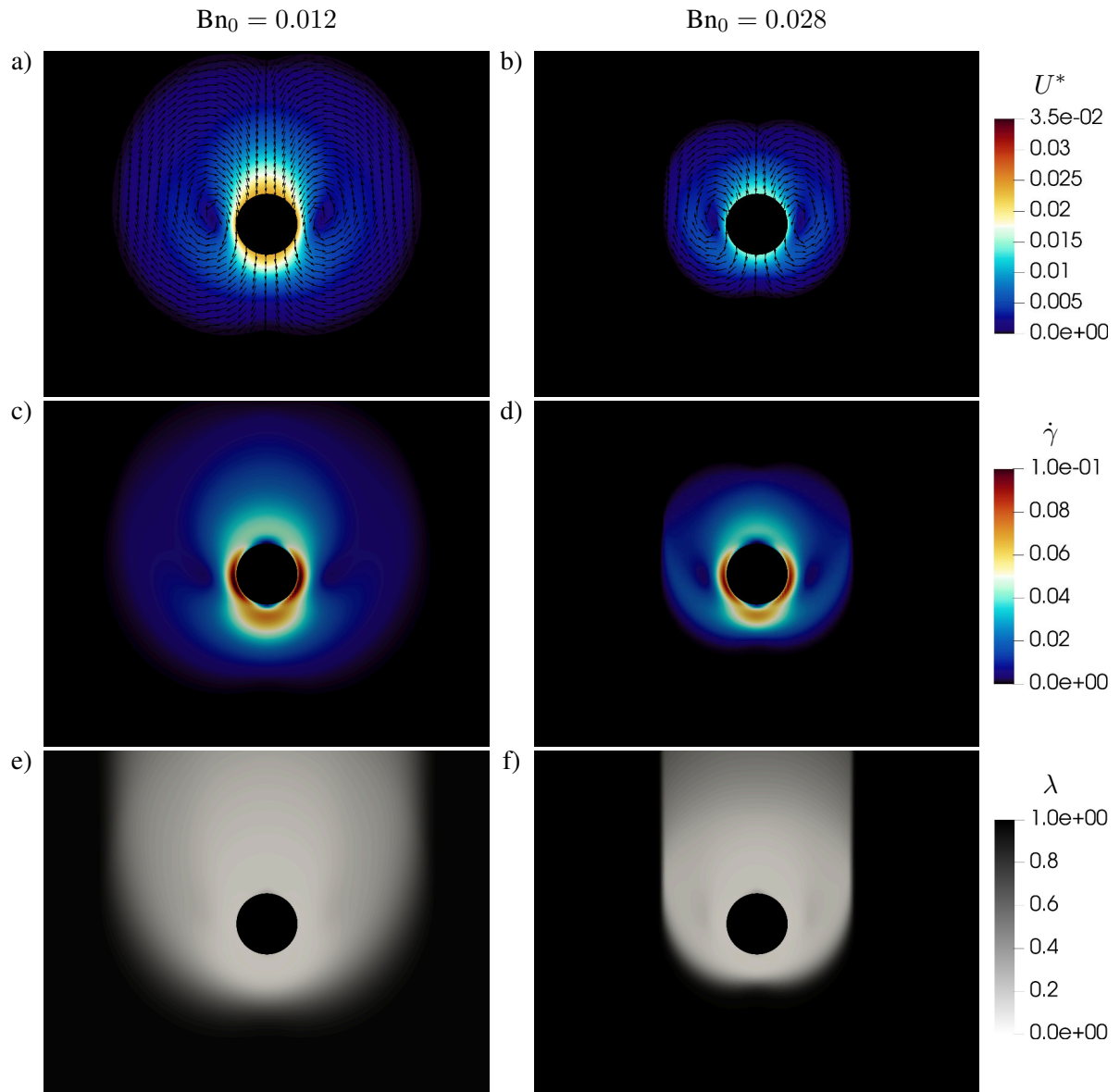
Source: Own elaboration.

The lower static Bingham number causes an increase in the yielded surface size around the particle, black regions in Fig. 6.3.a and Fig. 6.3.b. The shape is similar to the one encountered using the Bingham fluid model. However, there is a difference for the thixotropic case: the broken structural parameter, which reduces the yield stress, extends the yield surface downstream - causing the appearance of an asymmetry between the fore and aft sections of the particle. The particle's uneven position causes the flow inside the yield envelope to be compressed in the fore section and, consequently, increase the shear-

rate magnitude. The recirculation zone's position does not seem to be altered relative to the particle remaining near its equator. The structural parameter only starts to break when inside the yielded surface, and it reaches its minimal value in the particle surface, Fig. 6.3.e and Fig. 6.3.f. The exact location where the fluid-structure rupture occurs can be seen in the $D\lambda/Dt$ field, as shown in Fig. 6.4, where the orange-red regions represent the breakdown zones and the green zones the recovery of the material.

Figure 6.4 – $D\lambda/Dt$ field for a) $\text{Bn}_0 = 0.012$ and b) $\text{Bn}_0 = 0.028$ with $k_1^* = 2.25$, and $k_2^* = 1/344$. Red: $D\lambda/Dt < 0$, Green: $D\lambda/Dt > 0$.

a) $\text{Bn}_0 = 0.012$ b) $\text{Bn}_0 = 0.028$
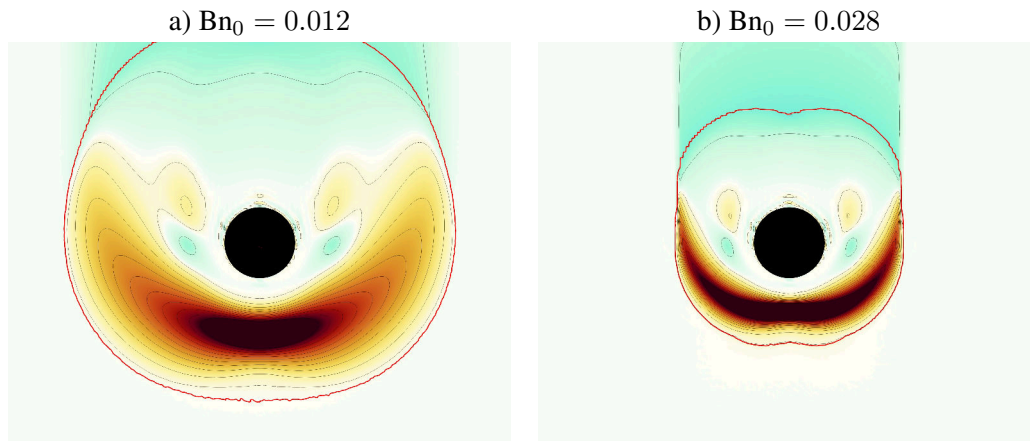
Source: Own elaboration.

Despite the fact that the highest shear-rate is near the particle's equator, as seen in Fig. 6.3, the fluid is mostly broken in its fore section, which corresponds to the zone where the settling particle displaces the fluid. Consequently, the fluid passing through this region will have a structural parameter close to 0 when near the particle surface. The high shear-rate will be responsible for keeping the structural parameter in an equilibrium state, where its recovery balances the fluid breakdown.

There are another two regions where this equilibrium state will occur: the first is in the edge of the recirculation zone, which inherently has a reduced shear-rate, causing the fluid to restructure. After the fluid leaves the recirculation, it moves to a higher shear-rate region and starts to break up again. Further downstream, the other transition occurs when the material that was sheared in the fore section and transported to a less shear-rate region. Here, the material is mainly unstructured, and consequently, it has a higher build-up rate. The fore-aft asymmetry then increases the distance between the particle and the yield envelope; therefore, the fluid has more space to flow, reducing the shear rate. The combination of these two effects causes the fluid to build-up past the end of the particle. When the particle settles further, the aft section's fluid will yield, and consequently will only age since it does not shear anymore.

Increasing the material's static yield stress raised the shear intensity in the fore section because the yielded envelope reduced in size, despite having a lower settling rate. The balance between the structure breakdown and the fluid yield-stress near the yield surface causes a parallel alignment in the mid-section with the settling direction. The yield surface then starts to curve back when the fluid transits from breakdown to recovering. The particle velocity response will depend on these different flows inside the yield envelope, which depend on the model's parameters.

6.1.1.1 Effect of the build-up parameter k_2^*

In the first analysis of the parameters' effect in the particle velocity, the dynamic Bingham number (Bn_∞) is kept constant at 0, while three build-up parameters are compared with a static Bingham number (Bn_0) ranging from 0.012 to 0.05. Due to the relatively short settling time, the build-up parameter is high: $1/344$, $1/688$, and $1/2158$. The results for the particle velocity and undisturbed structural parameter (fluid which did not suffer shear) values, represented by a dashed line, are presented in Fig. 6.5.

Figure 6.5 – Particle settling velocity over time as a function of the static Bingham number for three different build-up rates. a) $k_2^* = 1/2158$ b) $k_2^* = 1/688$ c) $k_2^* = 1/344$.
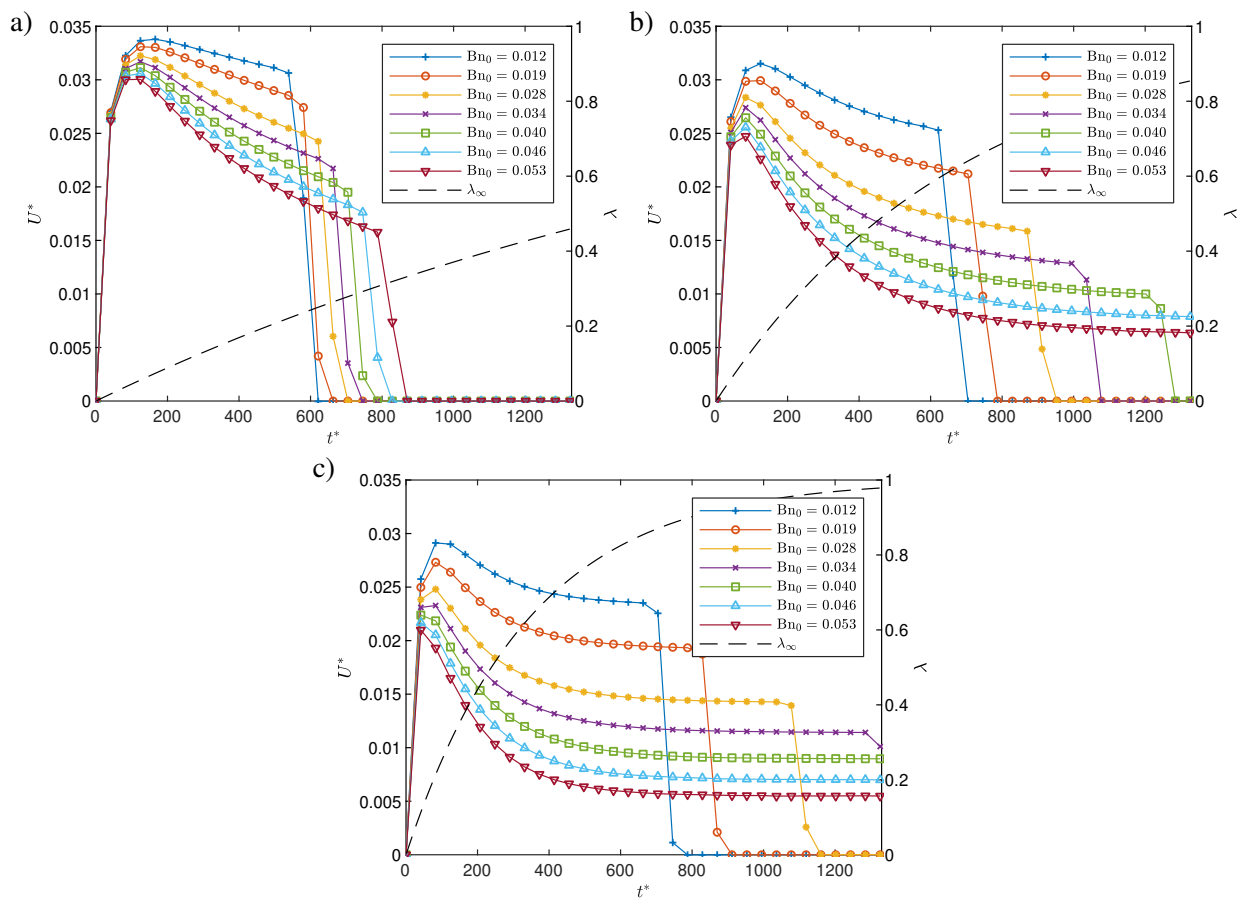
Source: Own elaboration.

First, during the acceleration phase, the particle reaches a peak velocity and afterward decay towards its terminal velocity. It is observed that for a lower build-up parameter, Fig. 6.5.a, the time to reach this peak velocity is weakly affected by the fluid static yield-stress. While for faster build-up fluids, Fig. 6.5.c, the static yield-stress has a more substantial effect in the time to reach the peak velocity, which occurs because during the acceleration phase, the fluid can be assumed as Newtonian ($\lambda \approx 0$), and the particle has approximately a constant acceleration. As the fluid starts to restructure, the plastic effects begin to rise, and consequently, the drag increases and initiate the particle deceleration sooner. Increasing the static Bingham numbers causes the peak velocity to have reduced magnitude; hence the time to achieve this peak will occur sooner.

The particle then proceeds with its deceleration until it reaches a quasi-steady-state ($\lambda_\infty > 0.95$)

regime and posteriorly collides with the domain's floor. A true steady-state would only be achieved when the undisturbed fluid is fully structured ($\lambda_\infty = 1$), which will only occur in an infinite time. Instead, it is noted that for studied cases, the particle velocity has a 1% difference when $\lambda_\infty \approx 0.95$ and 5% when $\lambda_\infty \approx 0.85$ from a theoretical terminal velocity, adjusted from exponential decay, independently of the static Bingham number. Higher build-up rates also caused a reduced time to reach the quasi-steady state velocity. For some cases, when the static Bingham number and build-up parameter are small, the particle collied with the domain floor before reaching its terminal velocity.

6.1.1.2 Effect of the breakdown parameter k_1^*

In this subsection is evaluated the effects of the breakdown parameter (k_1^*) in the settling velocity. The Bn_∞ is kept equal to zero, while the Bn_0 is 0.028 and 0.053. The breakdown parameter is varied from 0.025 to 5.5, and the results are reported in Fig. 6.6.

Figure 6.6 – Particle settling velocity over time as a function of the breakdown parameter (k_1) for two static Bingham numbers. a) $Bn_0 = 0.028$ b) $Bn_0 = 0.053$.
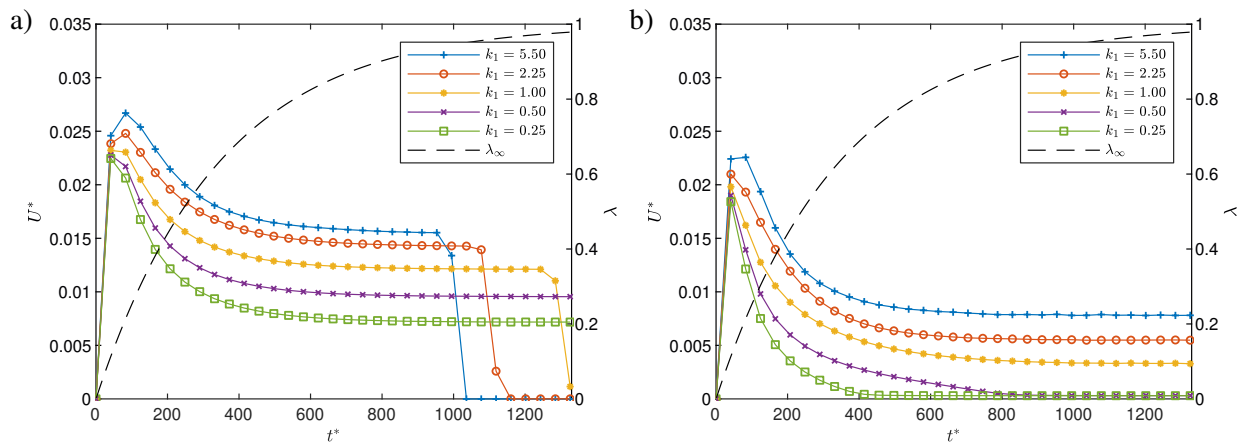
Source: Own elaboration.

The increase in the breakdown rate also increases the particle velocity because the particle creates a shear zone in its front, which breaks the fluid and reduces yield stress perceived by the particle on its surface. For $Bn_0 = 0.028$, the maximum yield number would be approximately 0.083. Independently of the breakdown parameter value, the particle always achieved a finite terminal velocity. As the breakdown parameter decreases, the particle terminal velocity asymptotically approaches the terminal velocity of a Bingham fluid with $Bn_0 = Bn_\infty$, as shown in Fig. 6.7.

For higher values of k_1^* there is also an indication that the terminal velocity asymptotically converges towards a fixed velocity value, corresponding to the velocity in an entirely unstructured fluid ($\lambda = 0$). When the fluid presents a higher breakdown parameter, the steady-state value of λ leans towards 0. Consequently, the terminal velocity will also have a value close to what would experience in a fully unstructured fluid, which can be seen in Fig. 6.8, where a significant part of the fluid inside the yielded region has a lower structural parameter value.

Another aspect is the yield surface format, which stretches in the trajectory direction with a higher breakdown rate. Downstream, where the fluid leaves the yielded region, the fluid still retains its lower

Figure 6.7 – Particle terminal velocity as a function of the breakdown parameter (k_1) for two static Bingham numbers (0.028 and 0.053). Dashed line represent the terminal velocity in a Bingham fluid with Bn = 0.028.
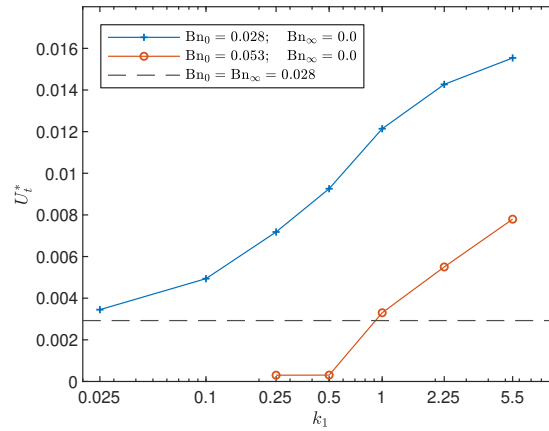
Source: Own elaboration.

Figure 6.8 – Structural parameter field and yield surface (red) at $t^* = 830$ and $Bn_0 = 0.028$ for two different breakdown parameters a) $k_1^* = 0.5$; b) $k_1^* = 2.25$.
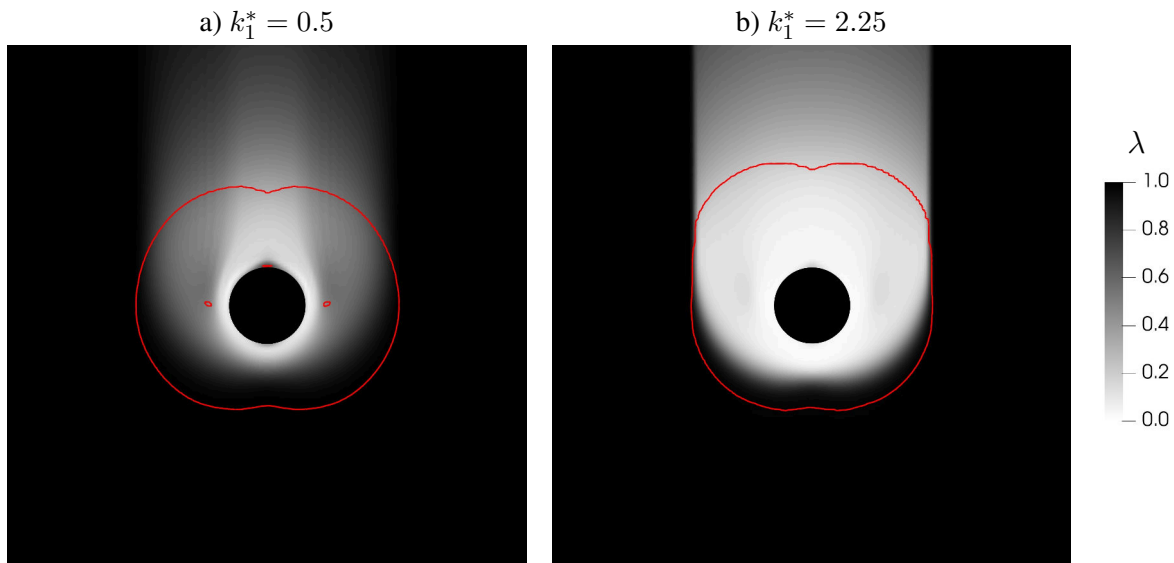
Source: Own elaboration.

structural parameter value. Consequently, if a second particle settles in that path, it will perceive this reduced yield stress and will lead to an increase in its settling velocity, as noted in experimental results in thixotropic fluids (GHEISSARY and BRULE, 1996)(MOSELEY et al., 2019).

When $Bn_0 = 0.053$, the theoretical maximum yield number would be 0.157. Due to this, there are some cases where the particle is retained by the fluid, as shown in Fig. 6.6. The time-evolution of the yield-surface with the velocity field is presented in Fig. 6.9 in order to understand the phenomenon.

Initially, the yield-surface acquire the characteristic shape of viscoplastic fluids. As time progresses, the particle decelerates and the unyielded regions, caps, and near the equator grow in size. After a point, the equatorial unyielded zone connects with the external unyielded fluid downstream. The result is distinct from the Bingham results of Wachs and Frigaard (2016), where the yield-surface uniformly

Figure 6.9 – Yielded (white) and unyielded (gray) zones for $Bn_0 = 0.053$, $Bn_\infty = 0.0$, $k_1 = 0.5$, and $k_2 = 1/344$ for different times and unscaled velocity vectors; a) $t^* = 330$, b) $t^* = 497$ c) $t^* = 662$, d) $t^* = 704$.
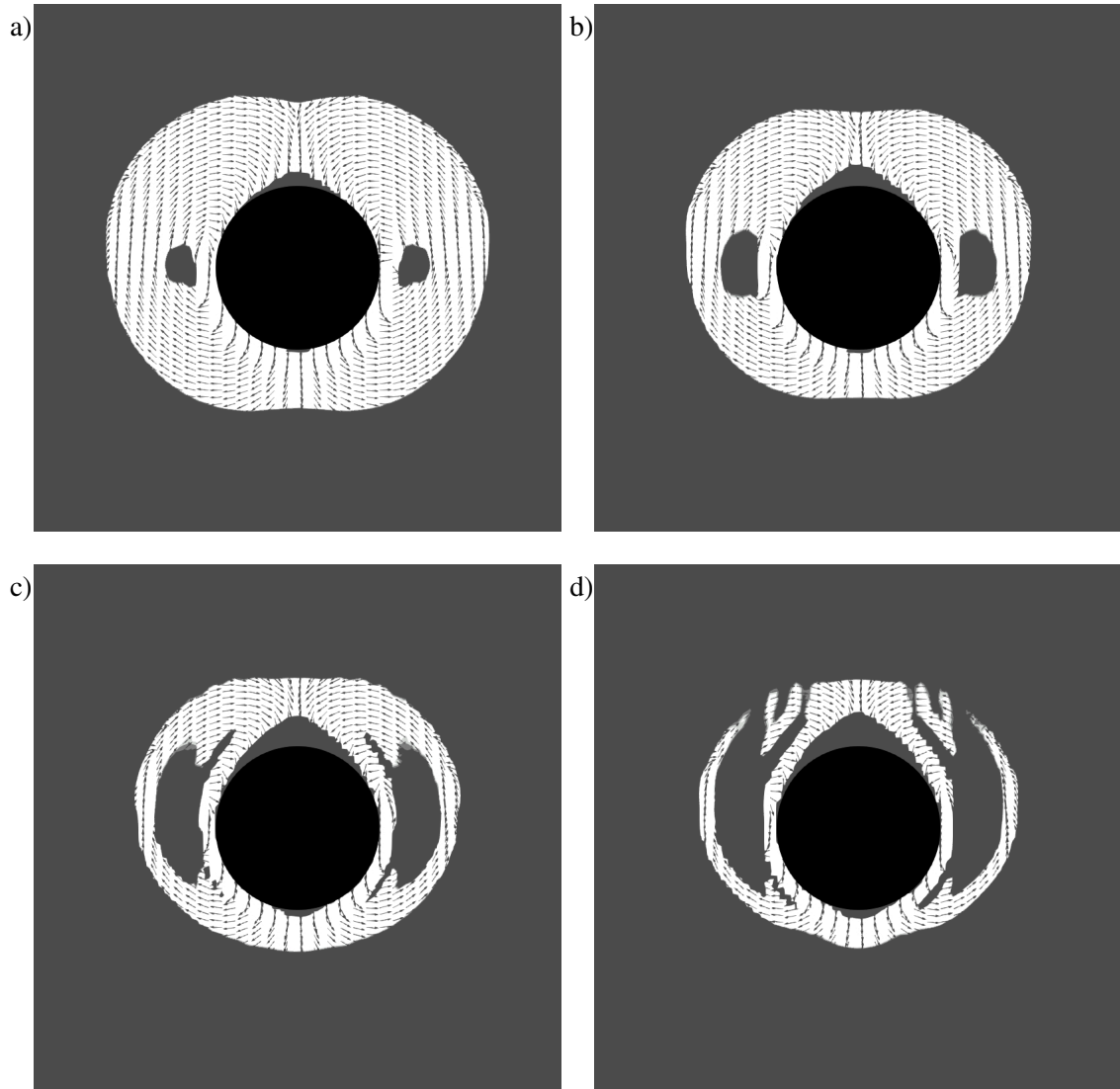
Source: Own elaboration.

collapsed. The yield surface collapse mechanism's difference can be explained by returning to the $d\lambda/dt$ field, Fig. 6.4. The breakdown zone after the recirculation zones ceases to exist due to the reduced shear-rate, causing the material to further structure. Consequently, when the material that passed through the recirculation zone hits the aft section it will have higher yield stress and yielding, blocking the flow inside the yield envelope. Afterward, the fluid movement near the particle stops, leading to an increase in the drag force until the particle ceases to move. Further analysis of the yield-surface evolution beyond this point was impossible because spatial resolution constraints forbid this fine since the yielded fluid region's scale is similar to the lattice size.

6.1.2   Case study $Bn_\infty \neq 0$

Here is evaluated the effects of the dynamic yield stress in the particle velocity. The effects are assessed for three build-up parameters and three static yield-stress values. The results for the particle

velocity are shown in Fig. 6.10. The breakdown parameter was kept constant at $k_1 = 2.25$.

Figure 6.10 – Particle velocity as a function of dynamic yield stress. $+\text{Bn}_\infty = 0.0$, $\circ\text{Bn}_\infty = 0.25\text{Bn}_0$, $*\text{Bn}_\infty = 0.5\text{Bn}_0$, $\text{- - -}\ \text{Bn}_\infty = \text{Bn}_0$
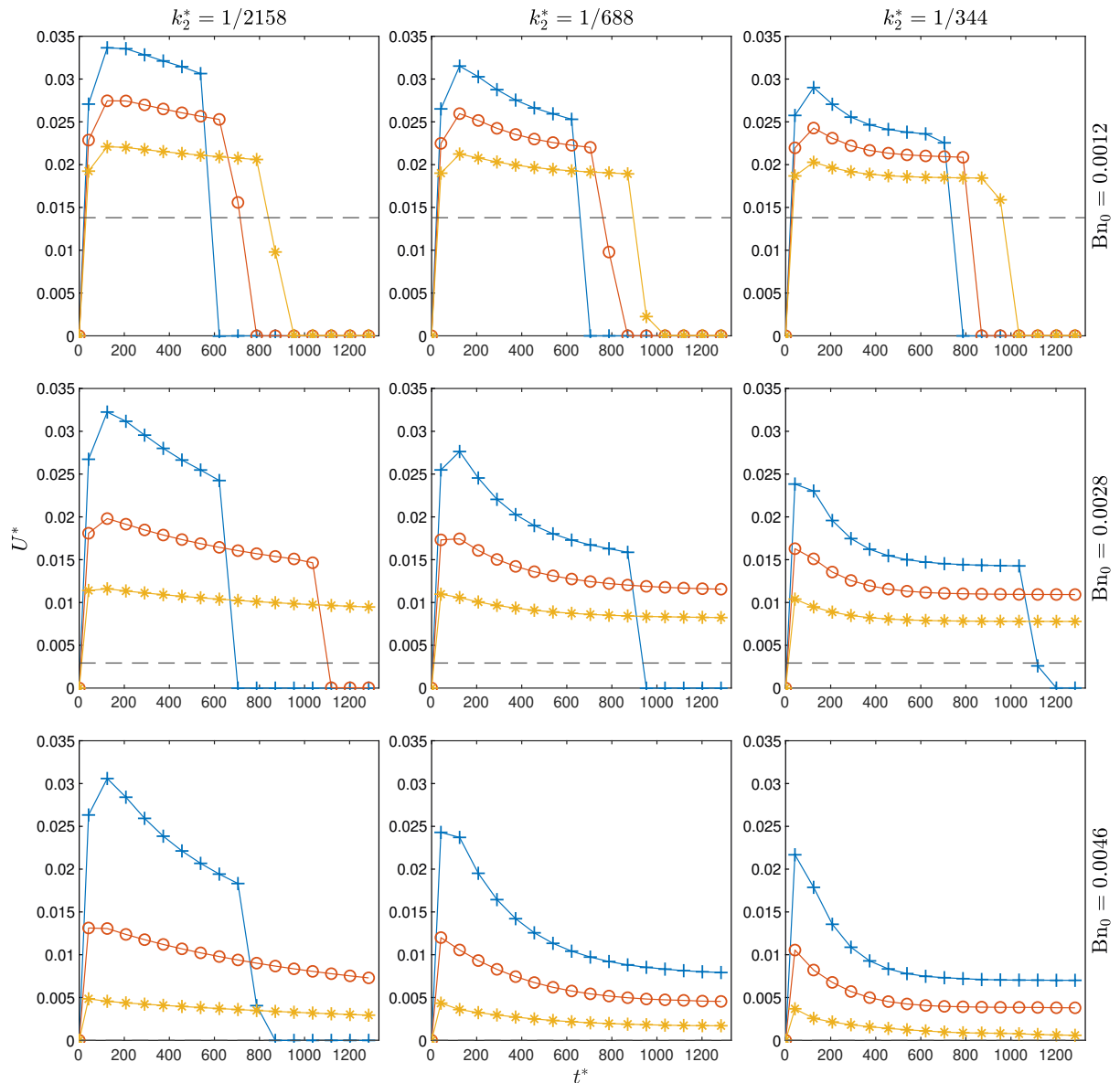
Source: Own elaboration.

It is noticed that by increasing the dynamic yield stress the particle velocity decreases, resulting from the overall increase in the flow's plastic effects. Another aspect is that dynamic yield stress reduced the particle's peak velocity compared with the terminal velocity. Increasing the Bingham ratio made the terminal velocity leans towards the value achieved in a Bingham fluid ($\text{Bn}_\infty = \text{Bn}_0$), stronger when the Bn_0 increases. A particular case occurs when $\text{Bn}_0 = 0.46$, which should not flow in the Bingham model, however for lower build-up rates, it still settles except when $\text{Bn}_\infty = 0.5\text{Bn}_0 = 0.23$ and $k_2^* = 1/344$, where the particle leans towards a cease of movement. Meaning that average yield stress around the particle was enough to cause this condition.

6.1.2.1 Numerical correlation

Finally, based on the numerical results, it is proposed a correlation for terminal velocity as a function of the Thixotropic number, static and dynamic Bingham numbers. As previously noted, the particle velocity will always be limited between two velocities, which corresponds to viscoplastic fluid with Bingham numbers between Bn_0 and Bn_∞. With that in mind, the proposed correlation utilizes a new variable, denominated effective structural parameter, which is responsible for translating between these two states:

$$U = \lambda_{\text{eff}} U^* (Bn_0) + (1 - \lambda_{\text{eff}}) U^* (Bn_\infty) \tag{6.1}$$

where λ_{eff} is the effective structural parameter, $U (Bn_0)$ and $U (Bn_\infty)$ is the particle terminal velocity in a Bingham fluid with Bingham number equal to Bn_0 and Bn_∞, respectively. The effects of the breakdown and build-up parameter are consolidated in the Thixotropic number, which will have an S-shape in semi-log scale, based on Fig. 6.7, which translates initially to:

$$\lambda_{\text{eff}} = 1 - \frac{\text{Tx}}{\text{Tx} + a} \tag{6.2}$$

Its value then needs to be scaled when $\text{Tx} \to \infty$, which is made by an approximation using the results when $\text{Tx} = 1550$ and $Bn_\infty = 0$, shown in Fig. 6.11.

Figure 6.11 – Particle terminal velocity as function of the static Bingham number for $Bn_\infty = 0$ and $Bn_\infty = Bn_0$ with $\text{Tx} = 1550$.
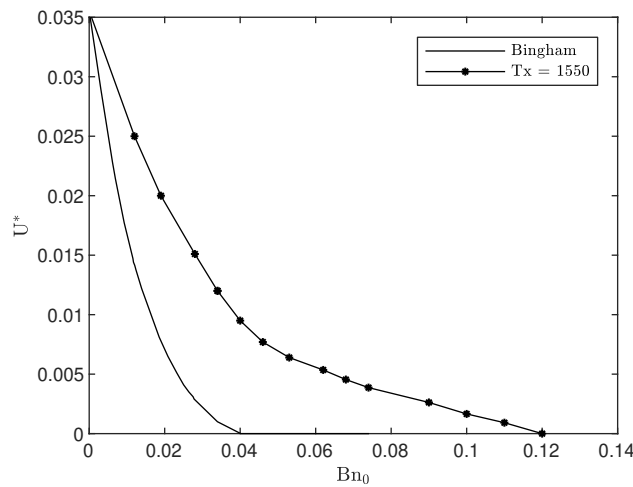
Source: Own elaboration.

The result can be approximated by a power decay $f(Bn_0) = c(Bn_0)^d + e$. For static Bingham number values superior to 0.12, the particle reached a state that could be considered retained by the fluid, which is approximately three times the necessary yield stress to retain the particle compared with a Bingham fluid model.

To account for the effect of a higher Bn_∞ in the terminal velocity, it was investigated its effect in the two Thixotropic numbers ($\text{Tx} = 34$ and 755), the results are represented in Fig. 6.12.

As the Bingham number ratio increases, the effective structural parameter linearly decreases until the yield stress ratio gets closes to 1, where it abruptly converges towards 0. To account for this effect in Eq. 6.1 it is utilized a linear approximation that is independent of the Thixotropic number. The lack

Figure 6.12 – The effective structural parameter value as a function of the Bingham ratio for Tx = 34 and 755.
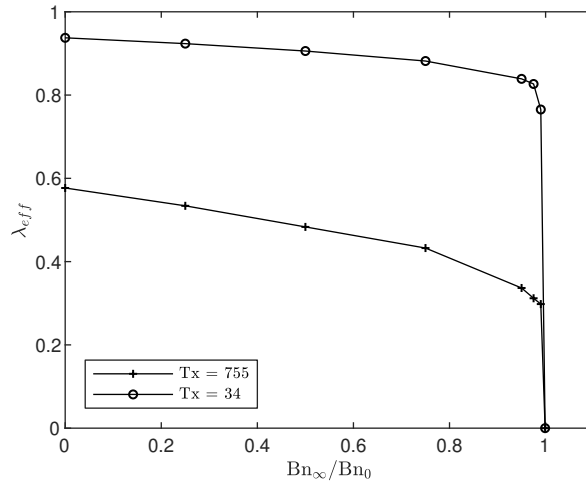
Source: Own elaboration.

of the asymptote in the linear approximation does not generate a considerable error in the velocity result since for Bingham ratios close to a unit, the velocities will approximately equal. As a result, the final correlation for the effective structural parameter is:

$$\lambda_{\text{eff}} = 1 - \frac{\text{Tx}}{\text{Tx} + a} \left[1 + b \left(\frac{\text{Bn}_\infty}{\text{Bn}_0} \right) \right] \left[c(\text{Bn}_0)^d + e \right] \qquad (6.3)$$

With the present numerical results, a regression analysis returns the fitting parameters: $a = 105$, $b = 0.75$, $c = -2.57$, $d = 0.15$, and $e = 1.87$. The comparison between the numerical results and the calculated results from the Eq. 6.3 are shown in Fig. 6.13, where the dashed lines represent the relative error of $\pm 10\%$. The adjusted R^2 obtained by this correlation was 0.9860, with the tabulated numerical results data for the terminal velocity in Appendix E. The correlation should capture all the behaviors observed in the cases analyzed, with the only exception being the cease of the particle motion.

6.2 Two particle settling

In this section, the previous study is extended for a two-particle system configuration. A schematic representation of the problem geometry is represented in Fig. 6.14. The particle and fluid properties are the same as the one-particle configuration. In this study, the trailing particle is positioned $43.4D$ from the bottom of the tank, which has dimensions of $7.5D \times 7.5D \times 45D$. The center of the leading particle is then positioned a distance W from the tailing particle center. It also exists an offset of $0.02\,D$ in the horizontal alignment to induce perturbation when the particles collide.

For this settling configuration, the domain is discretized with a lattice size of $h = 0.2$ mm, as consequence, the domain has a size of $150 \times 150 \times 900$ lattice units, and the spherical particles have a diameter of 20 lattice units. In all cases, the lattice viscosity is kept constant as 0.1 ($1/\omega_p = 0.8$), which leads to a time-step of 4×10^{-5}s and a lattice gravity acceleration of $g^* = 7.85 \times 10^{-5}$. The relaxation time for the λ transport equation is $\tau_g = 0.5001$.

Figure 6.13 – Comparison between the obtained terminal velocity results and the correlated ones. Dashed lines represent the relative error of $\pm 10\%$.
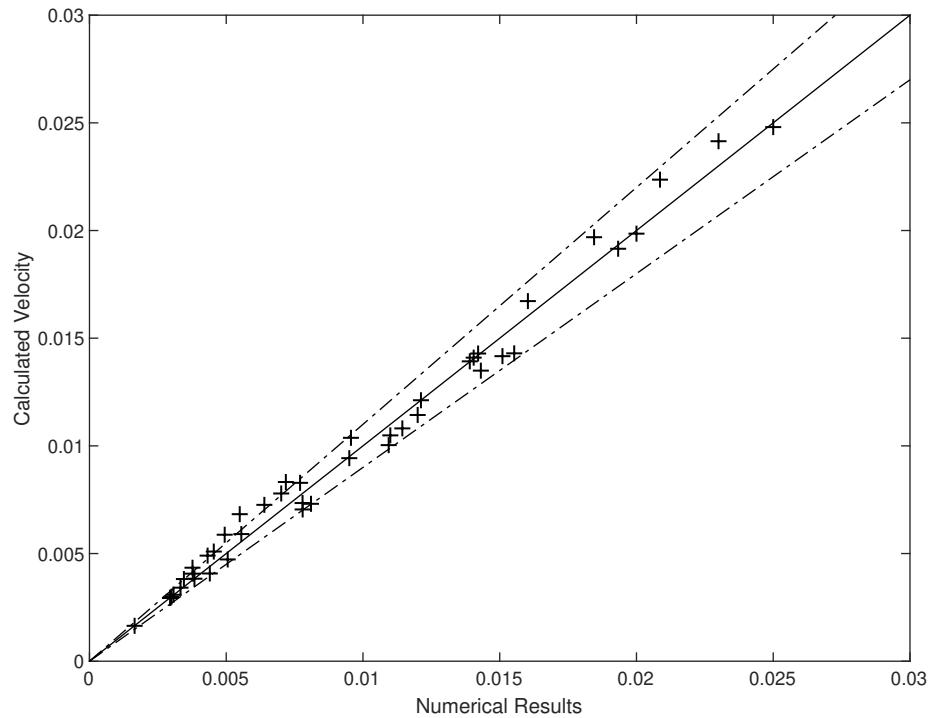
Source: Own elaboration.

6.2.1 Bingham cases $Bn_\infty = Bn_0$

First is investigated the settling in a Bingham fluid, which will provide a base for future comparisons in order to understand two-particle thixotropic settling. The settling is assessed for three Bingham numbers: Bn = 0.0031, 0.0093, and 0.0278 and with an initial separation distance of $W = 2D$. Figure 6.15 shows the results for the particle velocities and the separation over time.

Based on these results, it is possible to differentiate three regimes. The first regime occurs for low Bingham numbers, where the DKT process develops. The trailing and leading particles had a higher velocity than the settling of a single sphere. because the new flow configuration of the sphere pair reduces the drag effect. After the collision, the trailing slowly tumbles and finally collides with the domain floor. The second regime occurred for intermediate Bingham numbers. In this regime, the particles still draft but do not collide with each other. Here a the trailing particle moves towards the leading particle until they reach a critical distance and remain stable in this position without collision, as seen by the relative distance between the particles. In the final regime, for high Bingham numbers, there is no relative velocity between the settling particles, meaning that they start from a stable position. Therefore, it suggests that exists a minimal stable distance on which the particles will not perform the DKT process, which will be a function of the Bingham number. Figure 6.16 shows the flow around the particles for these two stable state regimes.

Differently from the settling of a single sphere, the yielded surfaces of the particles connect in the central region while a larger external yielded surface surges. Resulting in the rise of new internal unyielding regions, reported by Liu et al. (2003) and Prashant and Derksen (2011). The first unyielded

Figure 6.14 – Geometry of the two particle settling study.
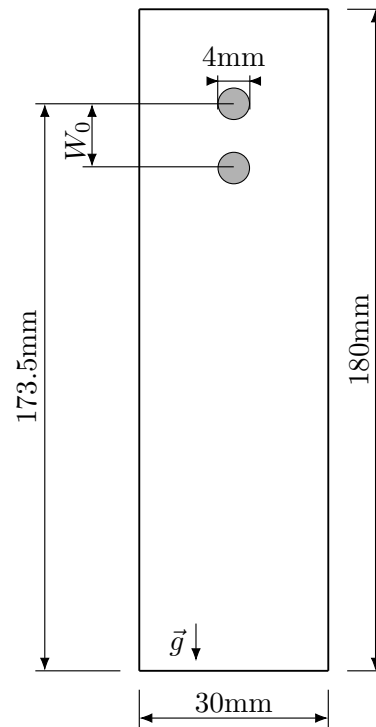
Source: Own elaboration.

region is located in the midplane away from the particles, assuming a toroidal shape. Meanwhile, the second is located in the central region between the particle centers.

6.2.2 Effect of the initial separation distance W_0^*

The first evaluation of the dual particle settling in a thixo-viscoplastic fluid is for the case where $\text{Bn}_\infty = 0$ and with different initial distances, ranging from $W_0^* = 2$ to 5. The breakdown and build-up parameters are $k_1^* = 3$ and $k_2^* = 1/650$, while the static Bingham number is $\text{Bn}_0 = 0.0278$. The temporal evolution of the structural parameter field and yield surface when $W_0^* = 5$ is shown in Fig. 6.17.

During the early settling stages ($t^* = 104$), Fig. 6.17.a, the fluid is still weakly structured ($\lambda \approx 0.15$), which causes the yield zone to extend until the walls. Its shape exhibit the characteristic form which occurred for the Bingham fluid case. As time passes ($t^* = 363$), Fig. 6.17.b, the increase in fluid structuring level causes the yield surface in the side of the leading particle to shrink. Meanwhile, the yield surface in the trailing particle remains practically the same size. The difference in size results in a yield surface with a slope, in agreement with the structural parameter field. The unsheared fluid then forces the yield surface of the trailing particle to shrink, according to the structural parameter field. The particles continue to settle until a point ($t^* = 623$), Fig. 6.17.c, where the slope is low enough, and the particles are close enough, that the stress caused by both displace the outside unyielding fluid. Causing an acceleration in both particles, which can be seen in Fig. 6.18.a through c. The only exception being for $W_0^* = 2$, because of the already initial proximity between the particles.

The trailing particle then continues to drift towards the leading one ($t^* = 881$), Fig. 6.17.d, until

Figure 6.15 – Left: Settling velocity for ○ - trailing and △ - leading particle; Right: Particle center distance; a) Bn = 0.0031; b) Bn = 0.0093; c) Bn = 0.0278
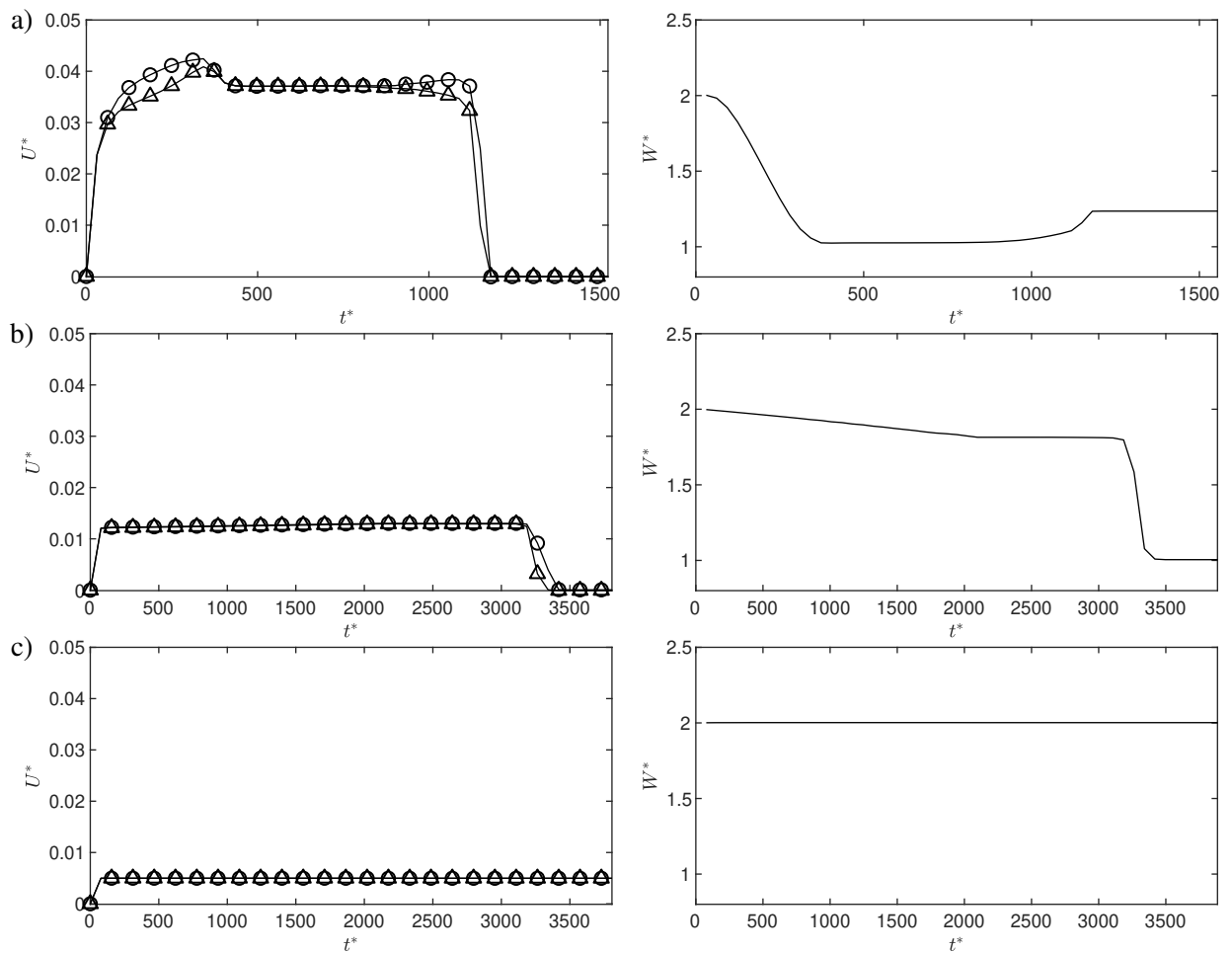
Source: Own elaboration.

it collides. The tumbling then begins, which is perceived by the increase in the velocity of the trilling particle while maintaining the same relative distance. With the tumbling finished, the particles separate and settle with the same velocity towards the bottom in a side-by-side configuration. The side-by-side settling then can be explained as follow: if one of the particles is in a lower position, it will experience a higher resistance by the fluid, which reduces its velocity. Meanwhile, the particle in a higher position would felt a lower drag because the fluid is being broke by the lower particle and consequently accelerates. As a result, the particles reach a periodic state where both have the same average terminal velocity and vertical position.

$W_0^* = 2$ is meaningful because it allows comparing the terminal velocity with results obtained for a single particle settling. Utilizing Eq.6.3, the terminal velocity for this case would be $U_t^* = 0.0126$ for a single particle, meanwhile for the dual particle settling, the terminal velocity was $U_t^* = 0.0148$, an increase of 17%.

Figure 6.16 – Yielded (white) and unyielded (gray) zones for a) Bn = 0.0093 and b) Bn = 0.0278 with unscaled velocity vectors for two particle settling in a Bingham fluid.

a) Bn = 0.0093   b) Bn = 0.0278
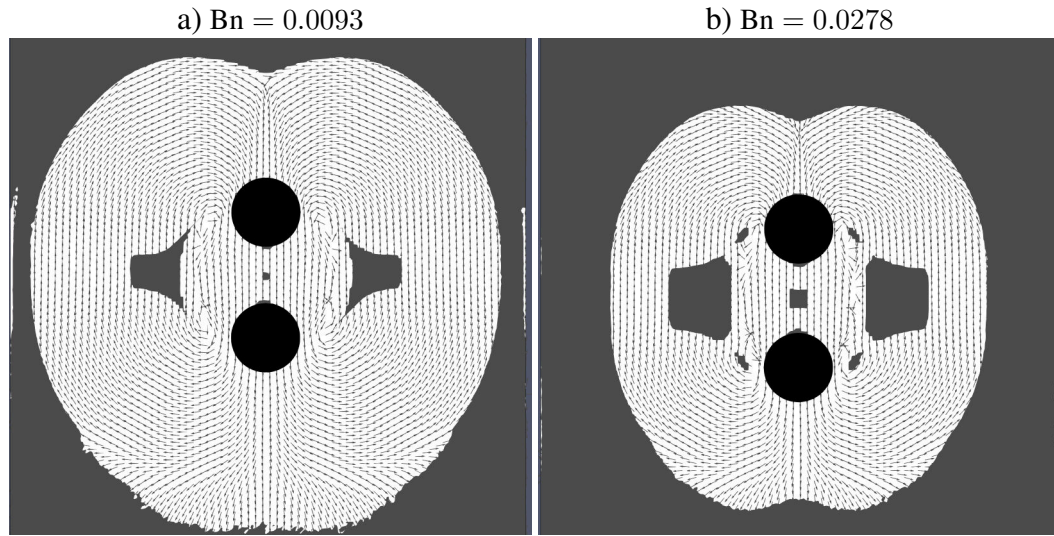
Source: Own elaboration.

6.2.3 Effect of the dynamic yield stress

Next is evaluated the effects of the dynamic yield stress in the settling of two particles. The static Bingham number is fixed in 0.046, while the dynamic Bingham number varies from 0 to 0.023. The initial separation distance is equal to $3D$, while the remaining parameters are equal to the previous results. The results for the particle velocities and relative distance are shown in Fig. 6.19.

In Fig. 6.19.a, where $Bn_\infty = 0$, is observed the same DKT behavior from the separation distance analysis. The differences when compared with Fig. 6.18.c, $Bn_0 = 0.046$ versus $Bn_0 = 0.028$, is a lower terminal velocity and a deceleration of the trailing particle during the drafting. It does not appear that the increase in the static yield number influenced the time for the collision between the particles. But decreased the tumbling duration in almost half. It is unclear if this is due to different yield stress or the chaotic behavior of the double particle system.

Increasing to dynamic yield stress to $Bn_\infty = 0.015$ reduced the initial peak velocity for both particles, similar to what was observed for the single-particle case. With the initial separation distance of $W_0^* = 3$, the yield surface to connected in the central annular region, Fig. 6.20 ($t^* = 647$), similar to the Bingham results from Liu et al. (2003). However, this was enough to reduce the drag force and reduce the particle distance over time. When the distance between the particles reduces beyond a certain point ($t^* = 1942$), the external yield surface saw in the Bingham case shows up and will increase the velocity of both particles, as seen in Fig. 6.19.b. For this case, the tumbling duration was short, which led the particles to a side-by-side configuration, and consequently, a decrease in the velocity.

The final case is when $Bn_\infty = 0.023$. Here the initial yield surfaces around the particles connect in the same annular central region as in the previous case. However, differently from the previous case, where the particles reduce the separation distance over time, here the trailing particle increases this separation distance, which may be attributed to a combination of the lower terminal velocity and the higher structural parameter between the particles. That causes the drag force of the leading particle to be

Figure 6.17 – Time evolution of structural parameter field and yield surface (red). $\text{Bn}_\infty = 0.0$, $\text{Bn}_0 = 0.0278$, $k_1^* = 3$, $k_2^* = 1/650$, and $W_0^* = 5$.

a) $t^* = 104$ b) $t^* = 363$ c) $t^* = 623$ d) $t^* = 881$
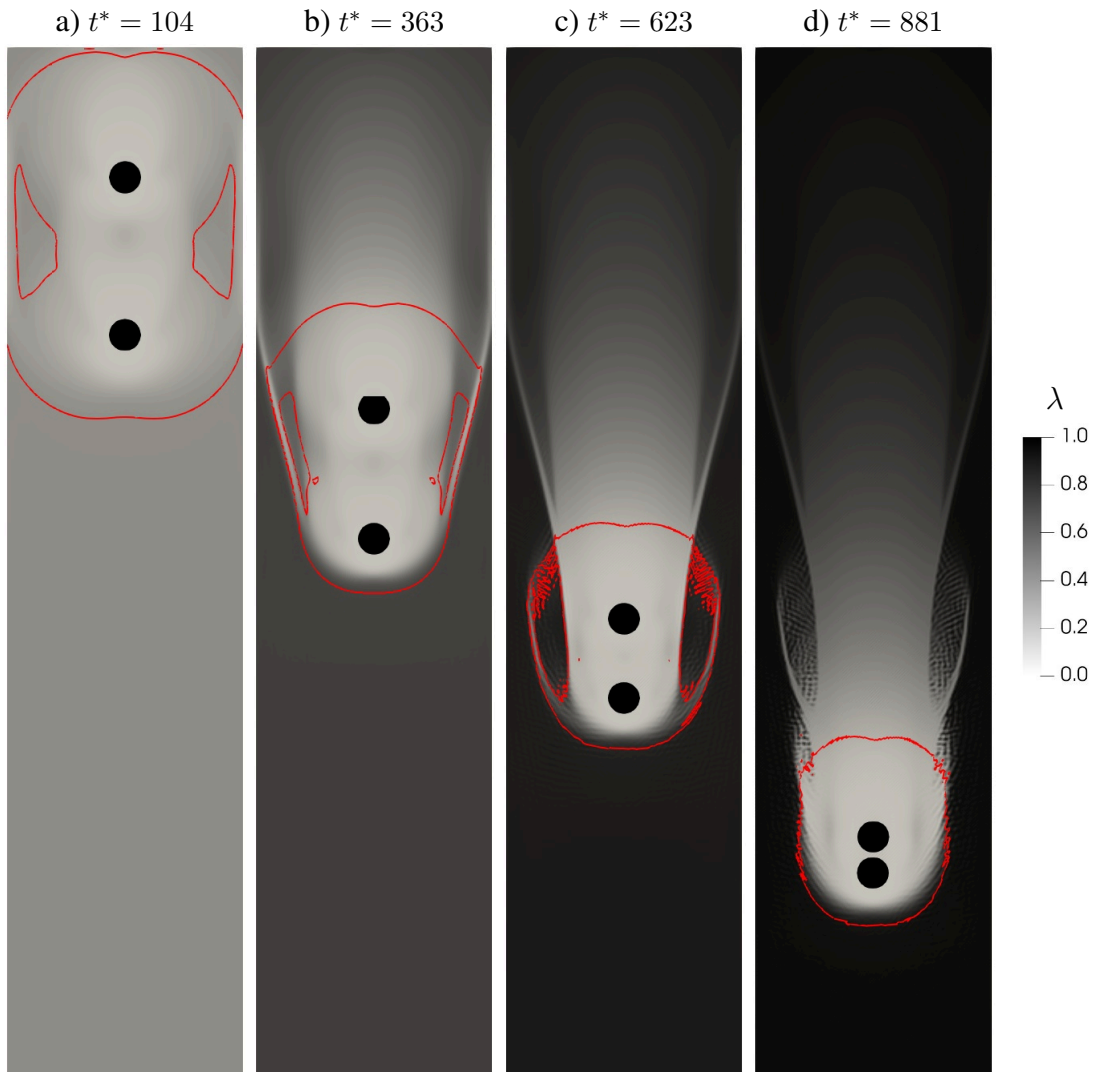
Source: Own elaboration.

lower than the trailing one.

6.2.4 Effect of the breakdown parameter k_1^*

The evaluation of thixotropic effects is performed for the breakdown parameter k_1^* with values equal to 4, 2, 1, and 0.5. The initial separation distance is $W_0^* = 3$ and the build-up parameter is $k_2^* = 1/650$. The static and dynamic Bingham numbers are respectively equal to 0.0278 and 0. The results for the particle velocities and trajectories are shown in Fig. 6.21.

The first observation, based on these cases, is that as the breakdown parameter decreases the time for the collision between the particles increases because the leading particle breaks the fluid with higher intensity, and consequently, the trailing particle perceives a reduced viscosity that increases its relative velocity.

Two regimes can be described in the studied range of the breakdown parameter. The first is for high

Figure 6.18 – Left: Settling velocity for ○ - trailing and △ - leading particle; Right: Particle center distance; a) $W_0^* = 5$; b) $W_0^* = 4$; c) $W_0^* = 3$; d) $W_0^* = 2$;
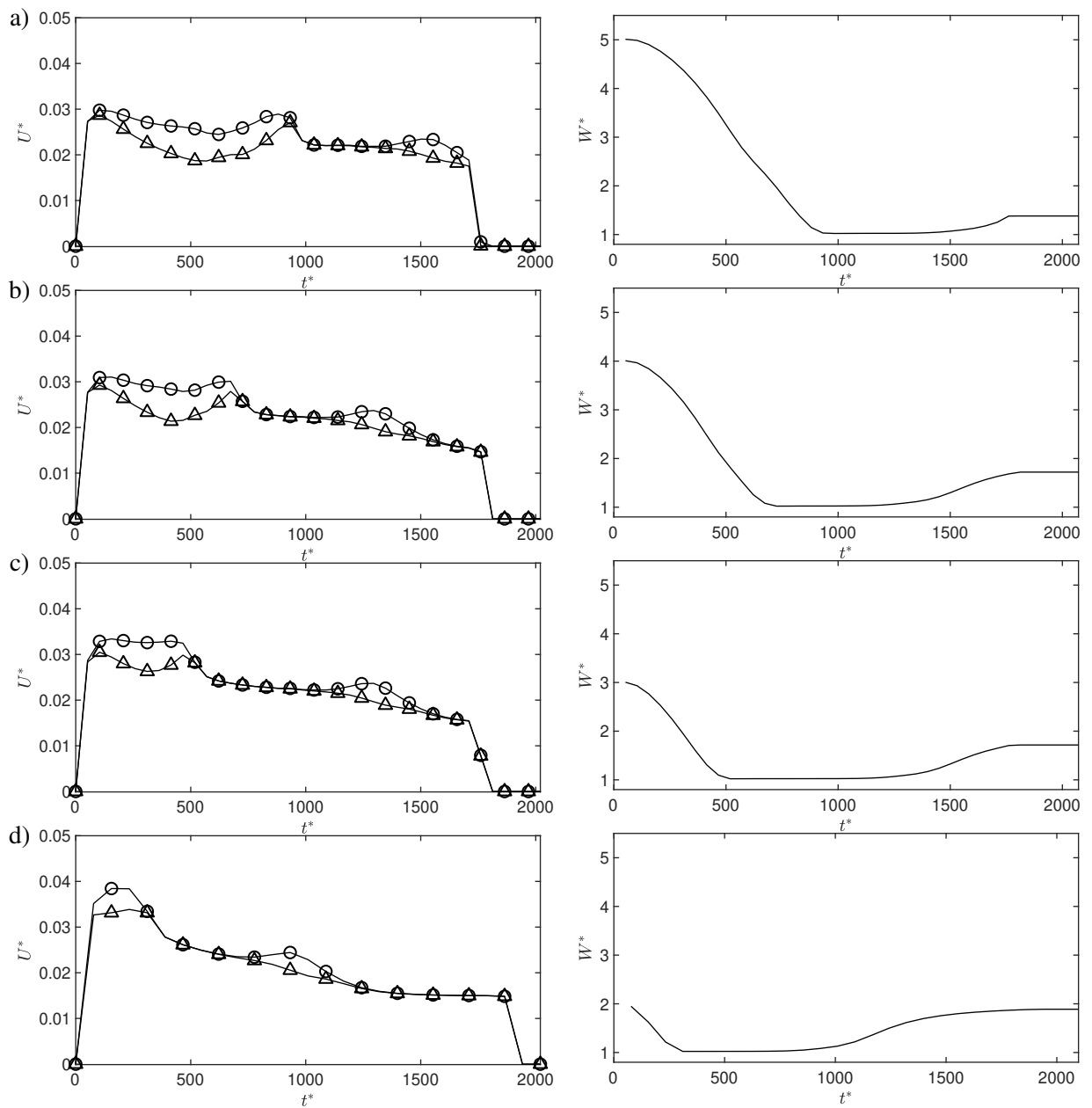
Source: Own elaboration.

values of k_1^*, represented in Fig. 6.21.a and b. In this regime, the breakdown rate is high enough to permit the lateral movement of the trailing particle, which leads to the observation of the DKT process.

The second regime occurs for low values of k_1^*, represented in Fig. 6.21.d and c. Here the trailing particle performs the draft until it collides with the leading particle. Nevertheless, after the collision, it does not perform the tumbling process. A possible explanation can be obtained by analyzing the structural parameter field, shown in Fig. 6.22.

Here it can be seen the difference between the two regimes. In the second regime the DKT process is not completed is that the leading particle creates a narrow path of reduced viscosity, as seen previously

Figure 6.19 – Left: Settling velocity for $\bigcirc$ - trailing and $\triangle$ - leading particle; Right: Particle center distance; a) $\mathrm{Bn}_\infty/\mathrm{Bn}_0 = 0$; b) $\mathrm{Bn}_\infty/\mathrm{Bn}_0 = 0.3$; c) $\mathrm{Bn}_\infty/\mathrm{Bn}_0 = 0.5$;

Source: Own elaboration.

in Fig. 6.8.a. As a consequence, the trailing particle is trapped in this path. The reason is that when the trailing particle starts its lateral movement, it encounters a region of higher viscosity while leaving one of reduced viscosity empty in the opposite direction. Since the particle seeks the path of least resistance to settle, it will return to the previous position, creating a stable system where both particles settle in a vertical alignment. When they finally collide with the domain floor, the trailing particle can finally tumble if existed a lateral displacement to the leading one, 6.21.c, or remain stacked one over the other, 6.21.d.

6.2.5 Build-up parameter k_2^* and cease of movement

To investigate the ability of the fluid to retain the particle is necessary to reduce the breakdown parameter while also increase the build-up rate. For that is used the same fluid conditions for a single sphere where was observed a cease of particle movement, Fig. 6.7. The breakdown parameter for that case $k_1^* = 0.25$ and the build-up parameter was $k_2^* = 1/344$, while the yield stresses are $\mathrm{Bn}_\infty = 0$ and $\mathrm{Bn}_0 = 0.053$. Since that for this condition is know that a single particle will be retained by the fluid, the introduction of the second particle will only affect if both are close together. For that is again evaluated

Figure 6.20 – Time evolution of structural parameter field and yield surface (red). $Bn_\infty = 0.015$, $Bn_0 = 0.046$, $k_1^* = 3$, and $k_2^* = 1/650$.

a) $t^* = 647$ b) $t^* = 1942$ c) $t^* = 2590$ d) $t^* = 3237$
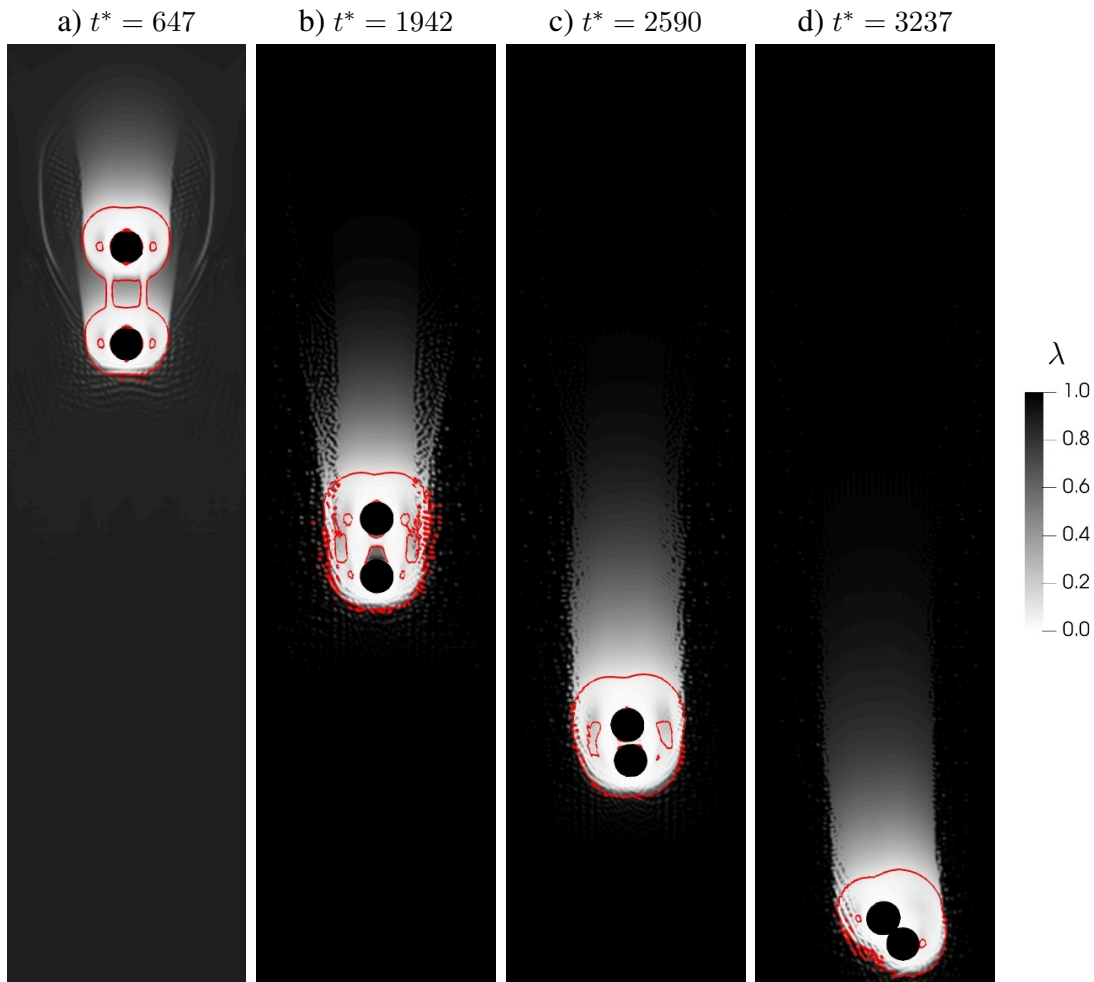
Source: Own elaboration.

the initial separation distance, which will range from $W_0^* = 3$ to 1.05. The results are presented in Fig. 6.23.

In Fig.6.23.a the particles initially approach each other while the fluid is still unstructured. After the fluid is broke by the leading particle it starts to restructure, increasing the structural parameter, and consequently, the yield stress, as seen in the previous images. The structuring level downstream then can be associated as a function of distance from the leading particle. Making that a particle with a higher separation distance will perceive a higher structuring level of the material causing it to have a lower velocity. If the separation distance is large enough, the trailing particle will still be retained by the fluid. In the other two cases, where the separation decreased, the trailing particle was not retained by fluid and accelerate both itself and the leading particle. As a result, the capacity of a thixo-viscoplastic fluid to hold particles is not only determined by its properties but also the distance and quantity of particles that settle together.

Figure 6.21 – Left: Settling velocity for $\bigcirc$ - trailing and $\triangle$ - leading particle; Right: Particle center distance; a) $k_1^* = 4$; b) $k_1^* = 2$; c) $k_1^* = 1$; d) $k_1^* = 0.5$;
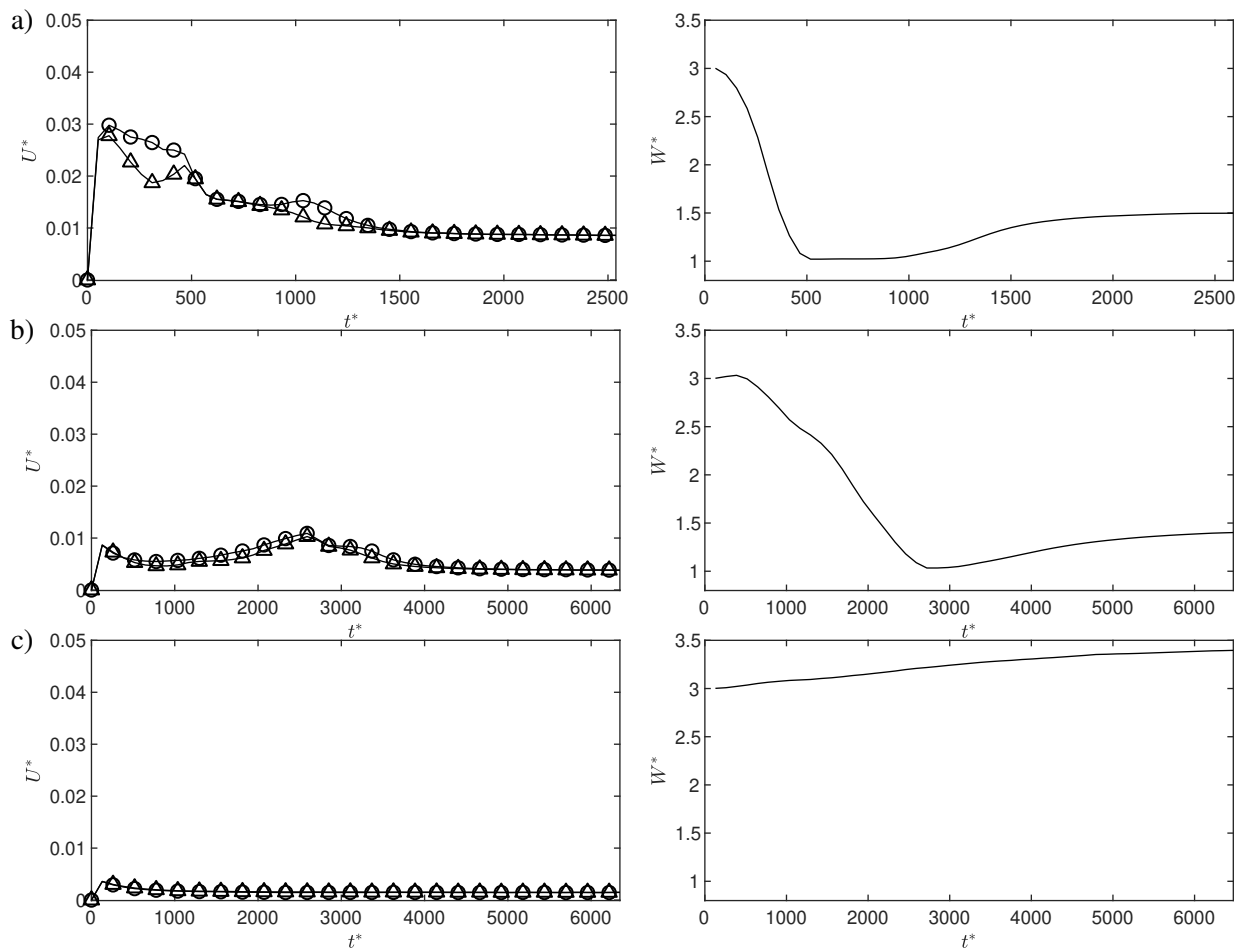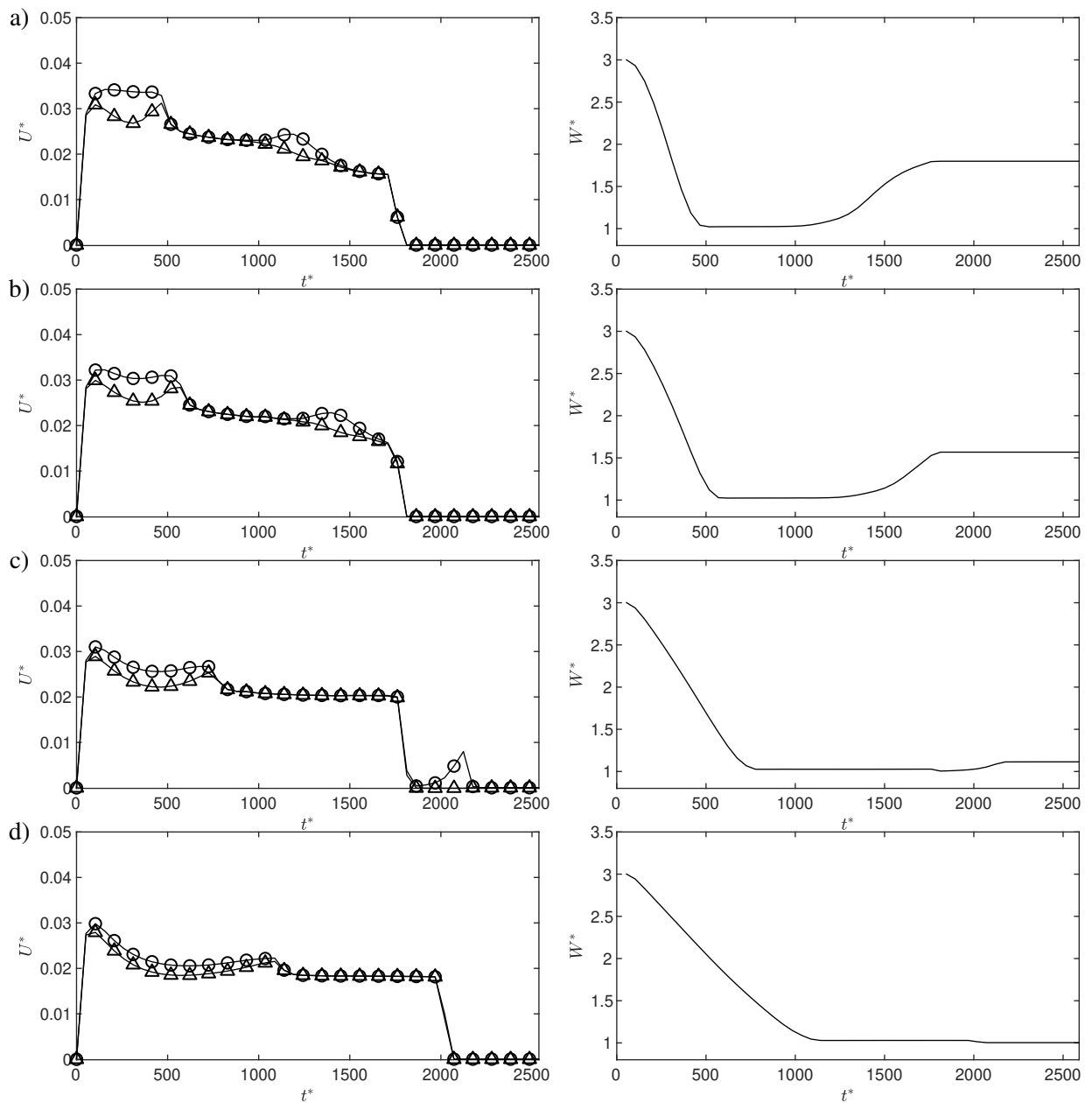

Source: Own elaboration.

Chapter Summary

In this chapter, it was presented the new results, not present in the literature for one and two particles settling in a thixo-viscoplastic fluid. For a single particle settling, it was evaluated the effects of the yield stress and kinematic parameters in the flow and evolution of the particle velocity over time. In the end is proposed, for the studied case, a correlation for the particle terminal velocity as a function of the Bingham and Thixotropic numbers. Next, a qualitative analysis of the two-particle system was realized. It was observed different settling regimes depending on the fluid properties which will influence the terminal velocity of the particle couple. And the fluid's capacity to retain a settling particle reduced

Figure 6.22 – Time evolution of structural parameter field and yield surface (red) for different breakdown parameters at $t^* = 1035$.
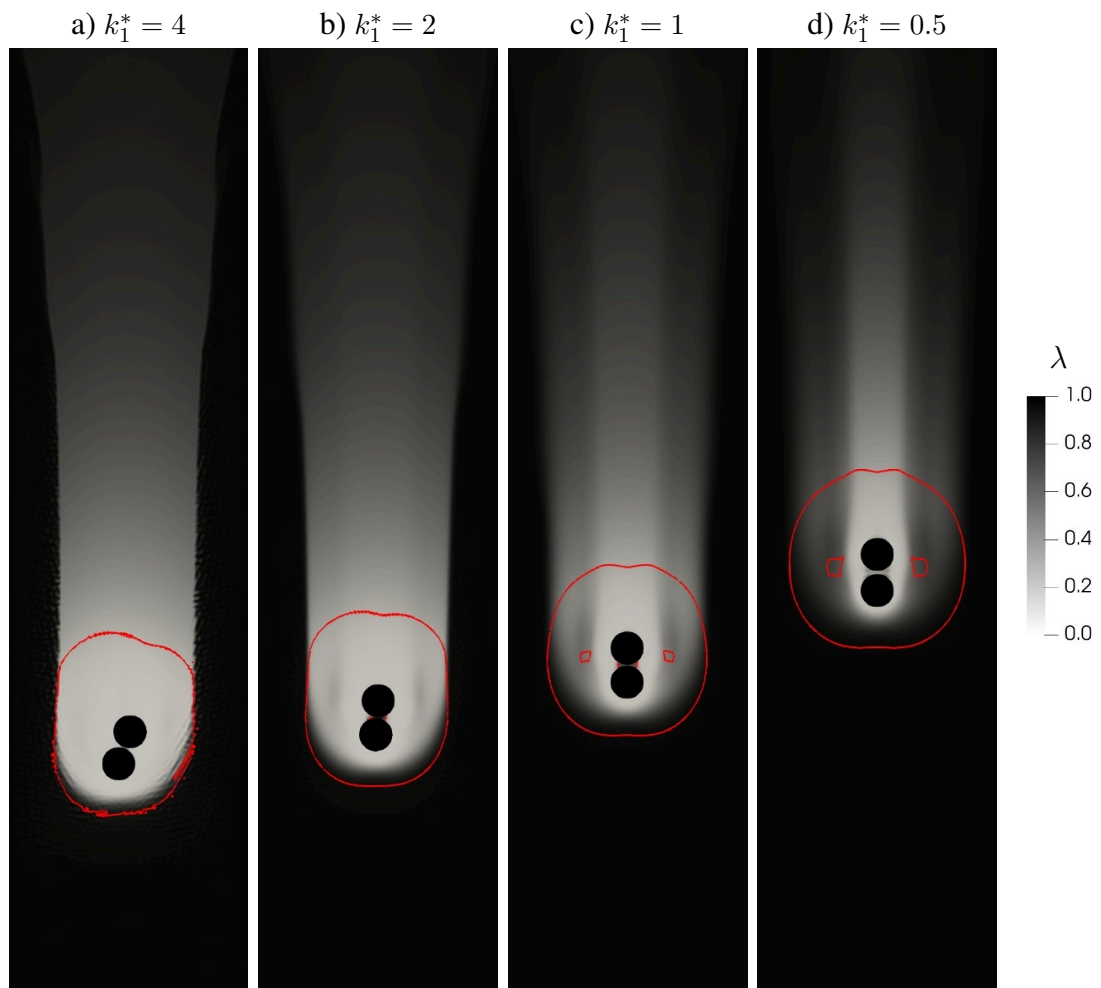
Source: Own elaboration.

when material recovery rate is not high enough that prevents the interaction between two or more settling particles.

Figure 6.23 – Left: Settling velocity for ○ - trailing and △ - leading particle; Right: Particle center distance; a) $W_0^* = 3$; b) $W_0^* = 1.5$; c) $W_0^* = 1.05$;
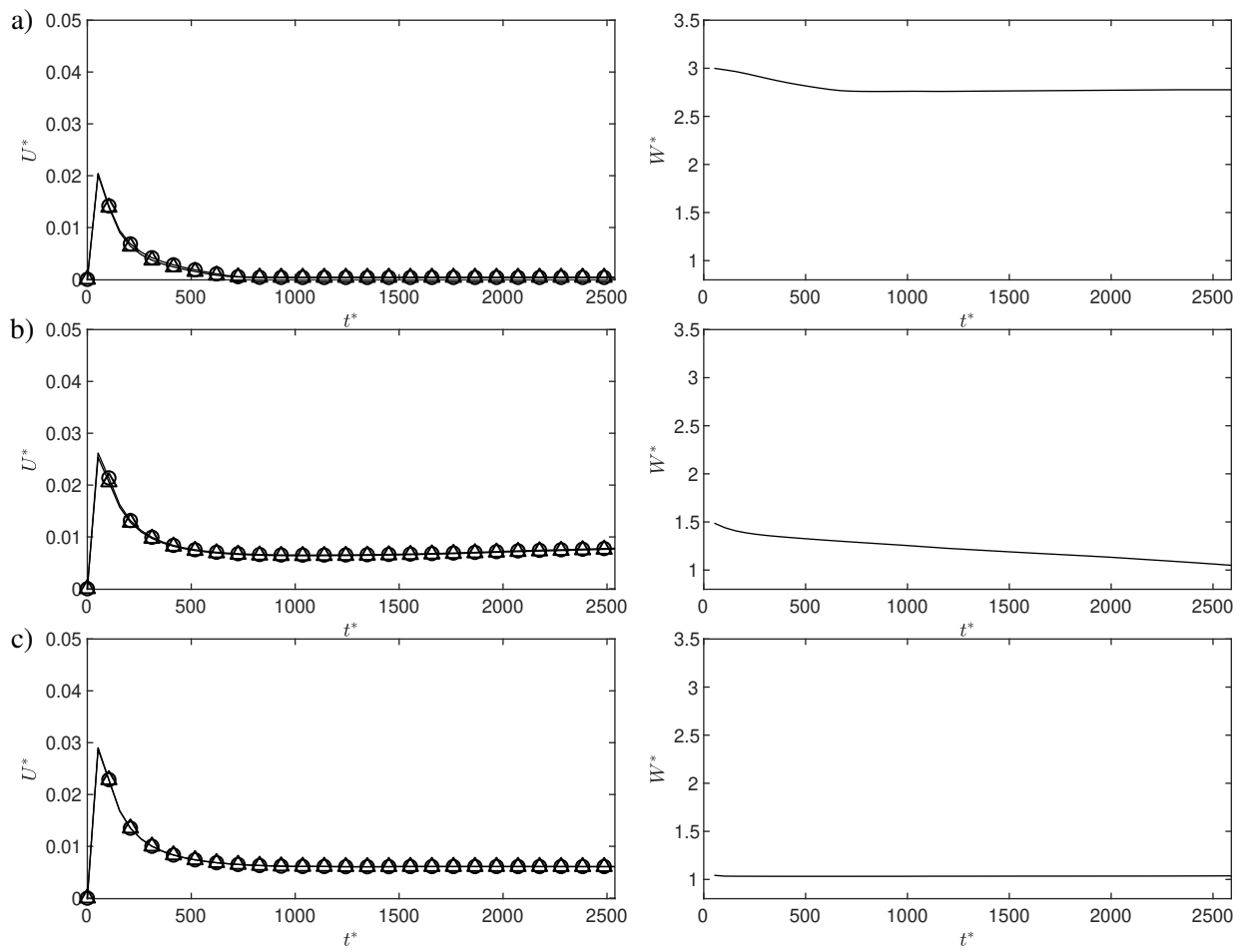
Source: Own elaboration.

7 CONCLUSION

The prediction of the settling rate is vital in several industrial applications. In the oil and gas industry, especially during the drilling operation, a wrong prediction can lead to a rise in the operation costs. For that reason, it is critical to have a reliable method to study the settling phenomenon in drilling fluids. Therefore, in the present work, a numerical method was proposed to study the particle settling in a thixo-viscoplastic material. The method was based on a dual-population lattice Boltzmann method, one responsible for mass and moment transport equations while the second was responsible for the thixotropic phenomenon. The particle-fluid coupling was achieved by using the immersed boundary method, while the particle-particle interaction used a soft-sphere model. The numerical code was written in CUDA®/C++ in order to take advantage of GPUs parallel computing advantage.

The numerical method was then verified against the analytical solutions for Poiseuille flows and validate for some cases in Newtonian and non-Newtonian flows. Later, it was evaluated the single-particle settling in a thixo-viscoplastic fluid, where the effects of kinetic parameter and yield stress in the particle terminal velocity are assessed. By analyzing the $d\lambda/dt$ field, it was found that the fluid mainly breaks in the fore section away from the particle, despite the highest shear-rate located near the equatorial surface of the particle. The particle terminal velocity had a sigmoidal behavior between the minimum and maximum permissible velocities as a function of the breakdown parameter. The breakdown parameter, depict as the Thixotropic number, was also responsible for increasing the critical yield number for a particle that is already in movement. The results were compiled and used to propose a numerical correlation for the terminal velocity as a function of the studied parameters

In a two-particle configuration was evaluated the effects of initial separation distance, dynamic yield stress, and breakdown rate. Depending on the initial distance between the particles, it was observed the formation of flow structures that resemble the flow in a viscoplastic fluid. These structures rise and disappear depending on the separation distance and structural parameter field around the particles. In the dynamic yield stress analysis, increasing it will also increase its resemblance with the flow in Bingham fluid since the dynamic and static yield stresses are close. It is also explained the stability the arises in the side-by-side settling configuration that occurs after the tumbling. The fluid breakdown rate had some interesting effects on the steady-state settling alignment between the particles. Lower values create a narrow wake of reduced viscosity that traps the trailing particle and consequently hinders the system from performing the tumbling phase of the DKT process.

All these results are significant since it increases the understanding of particle settling in thixo-viscoplastic fluids, which in the future might help field-engineers to determine the settling rate of cuttings. The knowledge that the addition of a second particle impacts the capacity of thixo-viscoplastic fluid to hold the cuttings have a direct translation with a multi-particle settling that occur in the borehole, with initial separation distance correlating to the particle concentration. By performing a non-dimensional study, it is expect that the results here presented can be extrapolated to problems in field, taking due precautions.

7.1 Recommendations

The main objectives of this work were achieved, develop a three-dimensional program, and study particle settling in a thixo-viscoplastic fluid. However, some improvements still can be made in future works.

The settling in a viscoplastic model can be improved since the current method to obtain the forces acting in the particle is based on the velocity difference between the particle and the fluid, which does not allow the particle to remain truly static in an unyielded fluid. Extend the fluid models in such a way that permits the addition of viscoelastic models and posteriorly a full thixo-elasto-visco-plastic material. Which will allow the fluid calibration with rheological data and later a validation with experimental results.

The collision model can also be improved. The soft-sphere collision model has its advantages, e.g. allows a triple collision in the case of multiple particle settling. However, a hard-sphere scheme would enable the model to be calibrated with real parameters, such as the coefficient of restitution and friction factor. The collision model can also be enhanced to allow cohesion forces between the particles.

Regarding the particle settling phenomenon, some cases still need to be explored. The study of one/two-particle settling can be extended for other diameters and density ratios and assess if the proposed correlation is still valid. It can also be evaluated the effect of different channel sizes and different particle shapes, such as ellipsoidal or prismatic particles. Ultimately the goal would be the study of multi-particle settling, where the distribution particle velocity would be obtained and utilized to elaborate a predictive model for the particle settling rate.

BIBLIOGRAPHY

ACHENBACH, E. Vortex shedding from spheres. *Journal of Fluid Mechanics*, v. 62, n. 2, p. 209–221, 1974.

AHMADPOUR, A.; SADEGHY, K. An exact solution for laminar, unidirectional flow of Houska thixotropic fluids in a circular pipe. *Journal of Non-Newtonian Fluid Mechanics*, v. 194, p. 23–31, 2013.

ANSLEY, R. W.; SMITH, T. N. Motion of spherical particles in a Bingham plastic. *AIChE Journal*, v. 13, n. 6, p. 1193–1196, 1967.

ATAPATTU, D.; CHHABRA, R.; UHLHERR, P. Creeping sphere motion in Herschel-Bulkley fluids: flow field and drag. *Journal of Non-Newtonian Fluid Mechanics*, v. 59, n. 2-3, p. 245–265, 1995.

BARNES, H. A. Thixotropy—a review. *Journal of Non-Newtonian Fluid Mechanics*, v. 70, n. 1-2, p. 1–33, 1997.

BEAULNE, M.; MITSOULIS, E. Creeping motion of a sphere in tubes filled with Herschel–Bulkley fluids. *Journal of Non-Newtonian Fluid Mechanics*, v. 72, n. 1, p. 55–71, 1997.

BERIS, A. N.; TSAMOPOULOS, J. A.; ARMSTRONG, R. C.; BROWN, R. A. Creeping motion of a sphere through a Bingham plastic. *Journal of Fluid Mechanics*, v. 158, n. July 2014, p. 219–244, 1985.

BHATNAGAR, P. L.; GROSS, E. P.; KROOK, M. A Model for Collision Processes in Gases. I. Small Amplitude Processes in Charged and Neutral One-Component Systems. *Physical Review*, v. 94, n. 3, p. 511–525, 1954.

BIRD, R. B.; ARMSTRONG, R. C.; HASSAGER, O. *Dynamics of Polymerics Liquids*. 2. ed. Wiley, 1987. 649 p.

BIRD, R. B.; STEWART, W. E. *Transport Phenomena*. 2. ed. Wiley, 2002. 895 p.

BLACKERY, J.; MITSOULIS, E. Creeping motion of a sphere in tubes filled with a Bingham plastic material. *Journal of Non-Newtonian Fluid Mechanics*, v. 70, n. 1-2, p. 59–77, 1997.

BOLTZMANN, L. *Vorlesungen uber Gastheorie*. Leipzig, J. A. Barth, 1896. 469 p.

BROMWICH, T. J. I. Motion of a Sphere in a Viscous Fluid. *Mathematical Proceedings of the Cambridge Philosophical Society*, v. 25, n. 4, p. 369–383, 1929.

BUICK, J. M.; GREATED, C. A. Gravity in a lattice Boltzmann model. *Physical Review E*, v. 61, n. 5, p. 5307–5320, 2000.

CATE, A. ten; NIEUWSTAD, C. H.; DERKSEN, J. J.; Van den Akker, H. E. A. Particle imaging velocimetry experiments and lattice-Boltzmann simulations on a single sphere settling under gravity. *Physics of Fluids*, v. 14, n. 11, p. 4012–4025, 2002.

CHHABRA, R. *Bubbles, Drops and Particles in Non-Newtonian Fluids*. 2. ed. CRC Press, 2006. 771 p.

CHHABRA, R.; RICHARDSON, J. F. *Non-Newtonian Flow and Applied Rheology*. Elsevier, 2008. v. 3. (Advances in Computational Fluid Dynamics, v. 3). Available on: <https://linkinghub.elsevier.com/retrieve/pii/B9780750685320X00017>.

CHILINGAR, G. V.; BURYAKOVSKY, L.; EREMENKO, N. A.; GORFUNKEL, M. V. *Geology and geochemistry of oil and gas*. 1. ed. Elsevier, 2005. 390 p.

CHOPARD, B.; FALCONE, J. L.; LATT, J. The lattice Boltzmann advection-diffusion model revisited. *European Physical Journal: Special Topics*, v. 171, n. 1, p. 245–249, 2009.

CLIFF, R.; GRACE, J. R.; WEBER, M. E. *Bubbles, Drops, and Particles*. 1. ed. Academic Press, 2005. 400 p.

COUSSOT, P.; NGUYEN, Q. D.; HUYNH, H. T.; BONN, D. Viscosity bifurcation in thixotropic, yielding fluids. *Journal of Rheology*, v. 46, n. 3, p. 573–589, 2002.

DASH, S.; LEE, T.; LIM, T.; HUANG, H. A flexible forcing three dimension IB–LBM scheme for flow past stationary and moving spheres. *Computers & Fluids*, Elsevier Ltd, v. 95, p. 159–170, 2014.

DAUGAN, S.; TALINI, L.; HERZHAFT, B.; ALLAIN, C. Aggregation of particles settling in shear-thinning fluids - Part 2. *The European Physical Journal E*, v. 9, n. 1, p. 55–62, 2002.

DAVIS, R. H.; ACRIVOS, A. Sedimentation of Noncolloidal Particles at Low Reynolds Numbers. *Annual Review of Fluid Mechanics*, v. 17, n. 1, p. 91–118, 1985.

DERKSEN, J. J.; PRASHANT. Simulations of complex flow of thixotropic liquids. *Journal of Non-Newtonian Fluid Mechanics*, v. 160, n. 2-3, p. 65–75, 2009.

DULLAERT, K.; MEWIS, J. A structural kinetics model for thixotropy. *Journal of Non-Newtonian Fluid Mechanics*, v. 139, n. 1-2, p. 21–30, 2006.

EUSTES, A. *Drilling Fluids*. 1. ed. [S.l.: s.n.], 2011. v. 12.

EWOLDT, R. H.; MCKINLEY, G. H. Mapping thixo-elasto-visco-plastic behavior. *Rheologica Acta*, Rheologica Acta, v. 56, n. 3, p. 195–210, 2017.

FENG, Z.-G.; MICHAELIDES, E. E. The immersed boundary-lattice Boltzmann method for solving fluid–particles interaction problems. *Journal of Computational Physics*, v. 195, n. 2, p. 602–628, 2004.

FENG, Z.-G.; MICHAELIDES, E. E. Proteus: a direct forcing method in the simulations of particulate flows. *Journal of Computational Physics*, v. 202, n. 1, p. 20–51, 2005.

FENG, Z.-G.; MICHAELIDES, E. E. Robust treatment of no-slip boundary condition and velocity updating for the lattice-Boltzmann simulation of particulate flows. *Computers & Fluids*, Elsevier Ltd, v. 38, n. 2, p. 370–381, 2009.

FERROIR, T.; HUYNH, H. T.; CHATEAU, X.; COUSSOT, P. Motion of a solid object through a pasty (thixotropic) fluid. *Physics of Fluids*, v. 16, n. 3, p. 594–601, 2004.

FONSECA, C.; FREY, S.; NACCACHE, M. F.; Souza Mendes, P. R. Flow of elasto-viscoplastic thixotropic liquids past a confined cylinder. *Journal of Non-Newtonian Fluid Mechanics*, Elsevier B.V., v. 193, p. 80–88, 2013.

FORTES, A. F.; JOSEPH, D. D.; LUNDGREN, T. S. Nonlinear mechanics of fluidization of beds of spherical particles. *Journal of Fluid Mechanics*, v. 177, p. 467–483, 1987.

FRAGGEDAKIS, D.; DIMAKOPOULOS, Y.; TSAMOPOULOS, J. Yielding the yield-stress analysis: A study focused on the effects of elasticity on the settling of a single spherical particle in simple yield-stress fluids. *Soft Matter*, Royal Society of Chemistry, v. 12, n. 24, p. 5378–5401, 2016.

FRIGAARD, I. A.; IGLESIAS, J. A.; MERCIER, G.; PÖSCHL, C.; SCHERZER, O. Critical yield numbers of rigid particles settling in Bingham fluids and cheeger sets. *SIAM Journal on Applied Mathematics*, v. 77, n. 2, p. 638–663, 2017.

FUČÍK, R.; EICHLER, P.; STRAKA, R.; PAUŠ, P.; KLINKOVSKÝ, J.; OBERHUBER, T. On optimal node spacing for immersed boundary–lattice Boltzmann method in 2D and 3D. *Computers & Mathematics with Applications*, v. 77, n. 4, p. 1144–1162, 2019.

GHEISSARY, G.; BRULE, B. van den. Unexpected phenomena observed in particle settling in non-Newtonian media. *Journal of Non-Newtonian Fluid Mechanics*, v. 67, n. 1-3, p. 1–18, 1996.

GINZBURG, I.; D'HUMIÈRES, D.; KUZMIN, A. Optimal stability of advection-diffusion lattice boltzmann models with two relaxation times for positive/negative equilibrium. *Journal of Statistical Physics*, v. 139, n. 6, p. 1090–1143, 2010.

GINZBURG, I.; VERHAEGHE, F.; D'HUMIÈRES, D. Two-relaxation-time Lattice Boltzmann scheme: About parametrization, velocity, pressure and mixed boundary conditions. *Communications in Computational Physics*, v. 3, n. 2, p. 427–478, 2008.

GLOWINSKI, R.; PAN, T.; HESLA, T.; JOSEPH, D.; PÉRIAUX, J. A Fictitious Domain Approach to the Direct Numerical Simulation of Incompressible Viscous Flow past Moving Rigid Bodies: Application to Particulate Flow. *Journal of Computational Physics*, v. 169, n. 2, p. 363–426, 2001.

GUESLIN, B.; TALINI, L.; PEYSSON, Y. Sphere settling in an aging yield stress fluid: link between the induced flows and the rheological behavior. *Rheologica Acta*, v. 48, n. 9, p. 961–970, 2009.

GUMULYA, M.; HORSLEY, R.; PAREEK, V. Numerical simulation of the settling behaviour of particles in thixotropic fluids. *Physics of Fluids*, v. 26, n. 2, p. 023102, 2014.

GUO, Z.; SHI, B.; ZHENG, C. A coupled lattice BGK model for the Boussinesq equations. *International Journal for Numerical Methods in Fluids*, v. 39, n. 4, p. 325–342, 2002.

GUO, Z.; SHU, C. *Lattice Boltzmann Method and Its Applications in Engineering*. WORLD SCIENTIFIC, 2013. v. 3. (Advances in Computational Fluid Dynamics, v. 3). Available on: <https://www.worldscientific.com/worldscibooks/10.1142/8806>.

GUO, Z.; ZHENG, C.; SHI, B. Discrete lattice effects on the forcing term in the lattice Boltzmann method. *Physical Review E*, v. 65, n. 4, p. 046308, 2002.

HE, X.; CHEN, S.; DOOLEN, G. D. A Novel Thermal Model for the Lattice Boltzmann Method in Incompressible Limit. *Journal of Computational Physics*, v. 146, n. 1, p. 282–300, 1998.

HE, X.; LUO, L. shi. Theory of the lattice Boltzmann method: From the Boltzmann equation to the lattice Boltzmann equation. *Physical Review E*, v. 56, n. 6, p. 6811–6817, 1997.

HEDSTRÖM, B. O. A. Flow of Plastic Materials in Pipes. *Industrial & Engineering Chemistry*, v. 44, n. 3, p. 651–656, 1952.

HOROWITZ, M.; WILLIAMSON, C. H. K. The effect of Reynolds number on the dynamics and wakes of freely rising and falling spheres. *Journal of Fluid Mechanics*, v. 651, p. 251–294, 2010.

HOUSKA, M. *Engineering Aspects of the Rheology of Thixotropic Liquids*. Thesis (Doctorate Degree) — Technical University of Prague, 1981.

HUILGOL, R. R. *Fluid Mechanics of Viscoplasticity*. Berlin, Heidelberg: Springer Berlin Heidelberg, 2015. 1–276 p. Available on: <http://link.springer.com/10.1007/978-3-662-45617-0>.

HUMIERES, D. Generalized Lattice-Boltzmann Equations. In: *Rarefied Gas Dynamics: Theory and Simulations*. Washington DC: American Institute of Aeronautics and Astronautics, 1994. p. 450–458. ISBN 9781600866319. Available on: <http://arc.aiaa.org/doi/10.2514/5.9781600866319.0450.0458>.

JANUSZEWSKI, M.; KOSTUR, M. Sailfish: A flexible multi-GPU implementation of the lattice Boltzmann method. *Computer Physics Communications*, v. 185, n. 9, p. 2350–2368, 2014.

KANG, S. K.; HASSAN, Y. A. A comparative study of direct-forcing immersed boundary-lattice Boltzmann methods for stationary complex boundaries. *International Journal for Numerical Methods in Fluids*, v. 66, n. 9, p. 1132–1158, 2011.

KATANFOROUSH, A.; SHAHSHAHANI, M. Distributing Points on the Sphere, I. *Experimental Mathematics*, v. 12, n. 2, p. 199–209, 2003.

KREMER, G. M. *An Introduction to the Boltzmann Equation and Transport Processes in Gases*. Berlin, Heidelberg: Springer Berlin Heidelberg, 2010. (Interaction of Mechanics and Mathematics). ISBN 978-3-642-11695-7. Available on: <http://link.springer.com/10.1007/978-3-642-11696-4>.

KRÜGER, T.; KUSUMAATMAJA, H.; KUZMIN, A.; SHARDT, O.; SILVA, G.; VIGGEN, E. M. *The Lattice Boltzmann Method*. 1. ed. Cham: Springer International Publishing, 2017. v. 23. 694 p. (Graduate Texts in Physics, 2). Available on: <http://link.springer.com/10.1007/978-3-319-44649-3>.

KRÜGER, T.; VARNIK, F.; RAABE, D. Efficient and accurate simulations of deformable particles immersed in a fluid using a combined immersed boundary lattice Boltzmann finite element method. *Computers & Mathematics with Applications*, Elsevier Ltd, v. 61, n. 12, p. 3485–3505, 2011.

LADD, A. J. C.; VERBERG, R. Lattice-Boltzmann Simulations of Particle-Fluid Suspensions. *Journal of Statistical Physics*, v. 104, n. September, p. 1191–1251, 2001.

LALLEMAND, P.; LUO, L.-S. Lattice Boltzmann method for moving boundaries. *Journal of Computational Physics*, v. 184, n. 2, p. 406–421, 2003.

LATT, J.; CHOPARD, B. Lattice Boltzmann method with regularized pre-collision distribution functions. *Mathematics and Computers in Simulation*, v. 72, n. 2-6, p. 165–168, 2006.

LIU, B. T.; MULLER, S. J.; DENN, M. M. Interactions of two rigid spheres translating collinearly in creeping flow in a Bingham material. *Journal of Non-Newtonian Fluid Mechanics*, v. 113, n. 1, p. 49–67, 2003.

LUGARINI, A.; FRANCO, A. T.; PHILIPPI, P. C. Lattice Boltzmann Method for Viscoplastic Fluid Flow Based on Regularization of Ghost Moments. *Journal of Non-Newtonian Fluid Mechanics*, Elsevier B.V., v. 286, n. August, p. 104413, 2020.

LUO, K.; WANG, Z.; FAN, J.; CEN, K. Full-scale solutions to particle-laden flows: Multidirect forcing and immersed boundary method. *Physical Review E*, v. 76, n. 6, p. 066709, 2007.

MALASPINAS, O.; FIÉTIER, N.; DEVILLE, M. Lattice Boltzmann method for the simulation of viscoelastic fluid flows. *Journal of Non-Newtonian Fluid Mechanics*, Elsevier B.V., v. 165, n. 23-24, p. 1637–1653, 2010.

MATTILA, K. K.; PHILIPPI, P. C.; HEGELE, L. A. High-order regularization in lattice-Boltzmann equations. *Physics of Fluids*, v. 29, n. 4, 2017.

MAWSON, M. J.; REVELL, A. J. Memory transfer optimization for a lattice Boltzmann solver on Kepler architecture nVidia GPUs. *Computer Physics Communications*, Elsevier B.V., v. 185, n. 10, p. 2566–2574, 2014.

MAXWELL, J. C. On the Dynamical Theory of Gases. In: *Phil. Trans. R. Soc. Lond.* [s.n.], 1867. p. 197–261. Available on: <http://www.worldscientific.com/doi/abs/10.1142/9781848161337{_}0>.

MEWIS, J.; WAGNER, N. J. Thixotropy. *Advances in Colloid and Interface Science*, v. 147-148, n. C, p. 214–227, 2009.

MITSOULIS, E. On creeping drag flow of a viscoplastic fluid past a circular cylinder: Wall effects. *Chemical Engineering Science*, v. 59, n. 4, p. 789–800, 2004.

MOORE, C. Data processing in exascale-class computer systems. In: *The Salishan Conference on High Speed Computing*. [S.l.: s.n.], 2011.

MOORE, F. The rheology of ceramic slips and bodies. *Trans Br Ceram Soc*, p. 470–494, 1959.

MORRISON, F. A. *An Introduction to fluid mechanics*. 1. ed. Cambridge University Press, 2013. 948 p. ISBN 9781107003538.

MOSELEY, K.; FAIRWEATHER, M.; HARBOTTLE, D. Settling dynamics of two identical vertically aligned spheres in a thixotropic fluid. *Journal of Non-Newtonian Fluid Mechanics*, Elsevier B.V., v. 271, n. June, p. 104146, 2019.

MUJUMDAR, A.; BERIS, A. N.; METZNER, A. B. Transient phenomena in thixotropic systems. *Journal of Non-Newtonian Fluid Mechanics*, v. 102, n. 2, p. 157–178, 2002.

NARDI, V. G.; FRANCO, A. T. Immersed Boundary - Lattice Boltzmann method for 2D particle sedimentation in Power-law fluids. In: *CILAMCE*. [S.l.: s.n.], 2018. p. 4.

NOBLE, D. R.; TORCZYNSKI, J. R. A Lattice-Boltzmann Method for Partially Saturated Computational Cells. *International Journal of Modern Physics C*, v. 09, n. 08, p. 1189–1201, 1998.

OLIVEIRA, W. B.; LUGARINI, A.; FRANCO, A. T. Performance Analysis of the Lattice Boltzmann Method Implementation on GPU. *XL Ibero-Latin-American Congress on Computational Methods in Engineering (CILAMCE 2019)*, 2019.

PAN, T.-W.; GLOWINSKI, R. Numerical study of spheres settling in Oldroyd-B fluids. *Physics of Fluids*, v. 30, n. 11, p. 113102, 2018.

PENG, C.; AYALA, O. M.; WANG, L.-P. A comparative study of immersed boundary method and interpolated bounce-back scheme for no-slip boundary treatment in the lattice Boltzmann method: Part I, laminar flows. *Computers & Fluids*, Elsevier Ltd, v. 192, p. 104233, 2019.

PESKIN, C. S. Flow patterns around heart valves: A numerical method. *Journal of Computational Physics*, v. 10, n. 2, p. 252–271, 1972.

PESKIN, C. S. The immersed boundary method. *Acta Numerica*, Unicamp, v. 11, n. May 2019, p. 479–517, 2002.

PHILIPPI, P. C.; HEGELE, L. A.; SANTOS, L. O. E. dos; SURMAS, R. From the continuous to the lattice Boltzmann equation: The discretization problem and thermal models. *Physical Review E*, v. 73, n. 5, p. 056702, 2006.

POOLE, R. The Deborah and Weissenberg numbers. *Rheology Bulletin*, v. 53, n. 2, p. 32–39, 2012.

PRASHANT; DERKSEN, J. J. Direct simulations of spherical particle motion in Bingham liquids. *Computers & Chemical Engineering*, Elsevier Ltd, v. 35, n. 7, p. 1200–1214, 2011.

PUTZ, A.; FRIGAARD, I. A. Creeping flow around particles in a Bingham fluid. *Journal of Non-Newtonian Fluid Mechanics*, Elsevier B.V., v. 165, n. 5-6, p. 263–280, 2010.

REYNOLDS, P.; JONES, T. An experimental study of the settling velocities of single particles in non-Newtonian fluids. *International Journal of Mineral Processing*, v. 25, n. 1-2, p. 47–77, 1989.

RIDDLE, M. J.; NARVAEZ, C.; BIRD, R. B. Interactions between two spheres falling along their line of centers in a viscoelastic fluid. *Journal of Non-Newtonian Fluid Mechanics*, v. 2, n. 1, p. 23–35, 1977.

SAKAMOTO, H.; HANIU, H. A Study on Vortex Shedding From Spheres in a Uniform Flow. *Journal of Fluids Engineering*, v. 112, n. 4, p. 386–392, 1990.

SCHLICHTING, H. *Boundary-Layer-Theory-Schlichting*. 7. ed. McGraw-Hill, 1979. 520 p.

SETA, T. Implicit temperature-correction-based immersed-boundary thermal lattice Boltzmann method for the simulation of natural convection. *Physical Review E - Statistical, Nonlinear, and Soft Matter Physics*, v. 87, n. 6, p. 1–16, 2013.

SHAN, X.; YUAN, X.-F.; CHEN, H. Kinetic theory representation of hydrodynamics: a way beyond the Navier–Stokes equation. *Journal of Fluid Mechanics*, v. 550, n. -1, p. 413, 2006.

SILVA, G.; SEMIAO, V. First-and second-order forcing expansions in a lattice Boltzmann method reproducing isothermal hydrodynamics in artificial compressibility form. *Journal of Fluid Mechanics*, v. 698, p. 282–303, 2012.

Souza Mendes, P. R. Modeling the thixotropic behavior of structured fluids. *Journal of Non-Newtonian Fluid Mechanics*, v. 164, n. 1-3, p. 66–75, 2009.

STOKES, G. G. On the Effect of the Internal Friction of Fluids on the Motion of Pendulums. In: *Transactions of the Cambridge Philosophical Society*. Cambridge: Cambridge University Press, 1850. cap. 9, p. 8–106. Available on: <https://archive.org/details/transactionsofca09camb/page/8>.

SULAYMON, A. H.; WILSON, C. A.; ALWARED, A. I. An experimental investigation of the settling behavior of two spheres in a power-law fluid. *Journal of Non-Newtonian Fluid Mechanics*, Elsevier B.V., v. 192, p. 29–36, 2013.

SUZUKI, K.; INAMURO, T. Effect of internal mass in the simulation of a moving body by the immersed boundary method. *Computers & Fluids*, Elsevier Ltd, v. 49, n. 1, p. 173–187, 2011.

SYRAKOS, A.; GEORGIOU, G. C.; ALEXANDROU, A. N. Thixotropic flow past a cylinder. *Journal of Non-Newtonian Fluid Mechanics*, Elsevier B.V., v. 220, p. 44–56, 2015.

TABUTEAU, H.; COUSSOT, P.; BRUYN, J. R. de. Drag force on a sphere in steady motion through a yield-stress fluid. *Journal of Rheology*, v. 51, n. 1, p. 125–137, 2007.

TANEDA, S. Experimental Investigation of the Wake behind a Sphere at Low Reynolds Numbers. *Journal of the Physical Society of Japan*, v. 11, n. 10, p. 1104–1108, 1956.

TOORMAN, E. A. Modelling the thixotropic behaviour of dense cohesive sediment suspensions. *Rheologica Acta*, v. 36, n. 1, p. 56–65, 1997.

UHLMANN, M. An immersed boundary method with direct forcing for the simulation of particulate flows. *Journal of Computational Physics*, v. 209, n. 2, p. 448–476, 2005.

VALERO-LARA, P.; IGUAL, F. D.; PRIETO-MATÍAS, M.; PINELLI, A.; FAVIER, J. Accelerating fluid–solid simulations (Lattice-Boltzmann & Immersed-Boundary) on heterogeneous architectures. *Journal of Computational Science*, Elsevier B.V., v. 10, p. 249–261, 2015.

WACHS, A.; FRIGAARD, I. A. Particle settling in yield stress fluids: Limiting time, distance and applications. *Journal of Non-Newtonian Fluid Mechanics*, Elsevier B.V., v. 238, p. 189–204, 2016.

WANG, D.; TAN, D.; PHAN-THIEN, N. A lattice Boltzmann method for simulating viscoelastic drops. *Physics of Fluids*, v. 31, n. 7, 2019.

WANG, Z.; FAN, J.; LUO, K. Combined multi-direct forcing and immersed boundary method for simulating flows with moving particles. *International Journal of Multiphase Flow*, v. 34, n. 3, p. 283–302, 2008.

WHITMORE, R. L.; BOARDMAN, G. Yield stress exerted on a body immersed in a bingham fluid. *Nature*, v. 194, n. 4825, p. 272, 1962.

WORRALL, W. E.; TULIANI, S. Viscosity changes during the ageing of clay-water suspensions. *Trans Br Ceram Soc*, p. 167–185, 1964.

WU, J.; SHU, C. Particulate Flow Simulation via a Boundary Condition-Enforced Immersed Boundary-Lattice Boltzmann Scheme. *Communications in Computational Physics*, v. 7, n. 4, p. 793–812, 2009.

WU, J.; SHU, C. An improved immersed boundary-lattice Boltzmann method for simulating three-dimensional incompressible flows. *Journal of Computational Physics*, Elsevier Inc., v. 229, n. 13, p. 5022–5042, 2010.

YU, D.; MEI, R.; SHYY, W. A multi-block lattice Boltzmann method for viscous fluid flows. *International Journal for Numerical Methods in Fluids*, v. 39, n. 2, p. 99–120, 2002.

YU, Z.; FAN, L.-S. Lattice Boltzmann method for simulating particle–fluid interactions. *Particuology*, Chinese Society of Particuology, v. 8, n. 6, p. 539–543, 2010.

YU, Z.; WACHS, A.; PEYSSON, Y. Numerical simulation of particle sedimentation in shear-thinning fluids with a fictitious domain method. *Journal of Non-Newtonian Fluid Mechanics*, v. 136, n. 2-3, p. 126–139, 2006.

ZOU, Q.; HE, X. On pressure and velocity boundary conditions for the lattice Boltzmann BGK model. *Physics of Fluids*, v. 9, n. 6, p. 1591–1598, 1997.

A ANALYTICAL DERIVATIONS

A.1 Thixotropic relaxation frequency

For a Herschel-Bulkley fluid stress/strain-rate relation is:

$$|\sigma| = K|\dot{\gamma}|^n + \sigma_y \tag{A.1}$$

From the Eqs. 4.14, 4.22, and generalized Newtonian fluid:

$$\eta = \rho c_s^2 \left(\tau - \frac{\Delta t}{2} \right) \tag{A.2a}$$

$$|\sigma| = \left(1 - \frac{\omega \Delta t}{2} \right) |T| \tag{A.2b}$$

$$|\dot{\gamma}| = \frac{|\sigma|}{\eta} \tag{A.2c}$$

Substituting these equations in Eq. A.1 and considering $\Delta t = 1$:

$$K \left(\frac{1}{\rho c_s^2} \right)^n \left(\frac{2\omega}{2-\omega} \right)^n \left[\left(\frac{2-\omega}{2} \right) |T| \right]^n + \frac{|T|\omega}{2} - |T| + \sigma_y = 0 \tag{A.3}$$

Factoring ω

$$\frac{2K}{(\rho c_s^2)^n} |T|^n \omega^n + |T|\omega + 2(\sigma_y - T) = 0 \tag{A.4}$$

But from Eq. 4.14 it is also possible:

$$\frac{2K}{\rho c_s^2} |\dot{\gamma}|^{n-1} = \frac{2}{\omega_p} - 1 \tag{A.5}$$

Consequently, Eq. A.4 becomes:

$$|T|\omega + \left(\frac{1}{|\dot{\gamma}|\rho c_s^2} \right)^{n-1} \left(\frac{2}{\omega_p} - 1 \right) |T|^n \omega^n - 2(|T| - \sigma_y) = 0 \tag{A.6}$$

which can be solved ω with iterative methods. In the simplified Houska's model used in this work $n = 1$. Hence Eq. A.6 becomes:

$$|T|\omega + \left(\frac{2}{\omega_p} - 1 \right) |T|\omega - 2(|T| - \sigma_y) = 0 \tag{A.7}$$

solving for ω:

$$\omega = \omega_p \left(1 - \frac{\sigma_y}{|T|} \right) \tag{A.8}$$

The yield stress in model is $\sigma_y = \lambda \sigma_{y,0} + (1 - \lambda) \sigma_{y,\infty}$ and $\omega > 0$, consequently:

$$\omega = \omega_p \text{max} \left(0, 1 - \frac{\lambda \sigma_{y,0} + (1 - \lambda) \sigma_{y,\infty}}{|T|} \right) \tag{A.9}$$

which is the Eq. 4.33.

A.2 Thixo-viscoplastic Hagen-Poiseuille – Analytical Solution

Channel diagram:
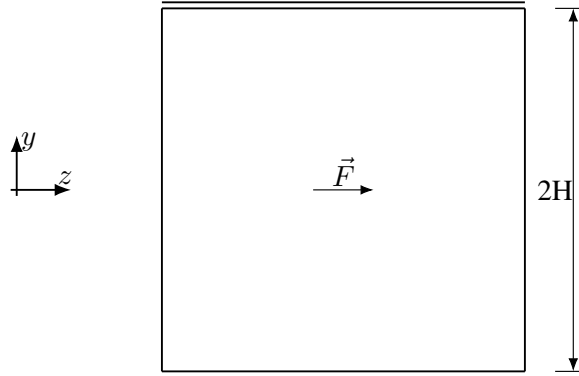
The conservation of mass and momentum equations:

$$\frac{\partial u_x}{\partial x} + \frac{\partial u_y}{\partial y} + \frac{\partial u_z}{\partial z} = 0 \tag{A.10}$$

$$\rho \left(\frac{\partial u_x}{\partial t} + u_x \frac{\partial u_x}{\partial x} + u_y \frac{\partial u_x}{\partial y} + u_z \frac{\partial u_x}{\partial z} \right) = - \left[\frac{\partial \sigma_{xx}}{\partial x} + \frac{\partial \sigma_{yx}}{\partial y} + \frac{\partial \sigma_{zx}}{\partial z} \right] + \rho g_x \tag{A.11a}$$

$$\rho \left(\frac{\partial u_y}{\partial t} + u_x \frac{\partial u_y}{\partial x} + u_y \frac{\partial u_y}{\partial y} + u_z \frac{\partial u_y}{\partial z} \right) = - \left[\frac{\partial \sigma_{xy}}{\partial x} + \frac{\partial \sigma_{yy}}{\partial y} + \frac{\partial \sigma_{zy}}{\partial z} \right] + \rho g_y \tag{A.11b}$$

$$\rho \left(\frac{\partial u_z}{\partial t} + u_x \frac{\partial u_z}{\partial x} + u_y \frac{\partial u_z}{\partial y} + u_z \frac{\partial u_z}{\partial z} \right) = - \left[\frac{\partial \sigma_{xz}}{\partial x} + \frac{\partial \sigma_{yz}}{\partial y} + \frac{\partial \sigma_{zz}}{\partial z} \right] + \rho g_z \tag{A.11c}$$

with the hypotheses:

- Incompressible fluid;
- Isotropic fluid;
- Unidimensional;
- Isothermal;
- Body force field only in the z-direction;

reduces to:

$$0 = -\frac{\partial \sigma_{yz}}{\partial y} + F \tag{A.12a}$$

$$u_y = 0 \tag{A.12b}$$

$$u_x = 0 \tag{A.12c}$$

on this uni-dimensional flow: $\sigma_{yz} = \sigma$. The thixotropic model used is based on Houska (1981):

$$\boldsymbol{\sigma} = \eta(\dot{\gamma}, \lambda)\dot{\boldsymbol{\gamma}}, \tag{A.13a}$$

$$\eta(\dot{\gamma}, \lambda) = \begin{cases} \infty & , |\sigma| \leq \sigma_y \\ \eta_p + \sigma_y |\dot{\gamma}| & , |\sigma| > \sigma_y \end{cases} \tag{A.13b}$$

$$\sigma_y = \lambda \sigma_{y,0} + (1 - \lambda)\, \sigma_{y,\infty} \tag{A.13c}$$

$$\frac{\partial \lambda}{\partial t} + u_i \frac{\partial \lambda}{\partial x_i} = -k_1 \lambda |\dot{\gamma}| + k_2 (1 - \lambda) \tag{A.13d}$$

for the Hagen-Poiseuille channel flow, the shear stress on steady-state can be written as a function of the distance from the channel center:

$$\sigma = Fy \tag{A.14}$$

rewriting in terms of shear-rate:

$$\dot{\gamma} = \left| \frac{Fy}{\eta(\lambda)} \right| \tag{A.15}$$

and considering the yield-stress:

$$\dot{\gamma} = \begin{cases} 0 & , |\sigma| \leq \sigma_y \\ |Fy - \sigma_y(\lambda)|/\eta_p & , |\sigma| > \sigma_y \end{cases} \tag{A.16}$$

In the steady-state kinetic equation for the structural parameter, Eq.A.13d reduces to:

$$k_1 \lambda \dot{\gamma} = k_2(1 - \lambda) \tag{A.17}$$

substituting it on the Eq. A.16:

$$\begin{cases} \lambda_{ss} = 1 & , |\sigma| \leq \sigma_y \\ k_1 \lambda_{ss} |yF - \sigma_y(\lambda_{ss})|/\eta_p = k_2(1 - \lambda_{ss}) & , |\sigma| > \sigma_y \end{cases} \tag{A.18}$$

for $|\sigma| > \sigma_y$ and $y > 0$, it can be rewritten as:

$$\frac{k_1(\sigma_{y,\infty} - \sigma_{y,0})}{\eta_p} \lambda_{ss}^2 + \left[k_2 - \frac{k_1(\sigma_{y,\infty} - Fy)}{\eta_p} \right] \lambda_{ss} - k_2 = 0 \tag{A.19}$$

with valid solution for $y > 0$:

$$\lambda_{ss}(y) = \frac{-[k_2\eta_p - k_1(\sigma_{y,\infty} - Fy)] + \sqrt{[k_2\eta_p - k_1(\sigma_{y,\infty} - Fy)]^2 + 4k_1 k_2 \eta_p (\sigma_{y,\infty} - \sigma_{y,0})}}{2k_1(\sigma_{y,\infty} - \sigma_{y,0})} \tag{A.20}$$

With the the solution for the structural parameter defined, the velocity profile can be obtained by substituting the Eq.A.20 in the Eq.A.15:

$$\frac{\partial u_z}{\partial y} = \frac{Fy - [\lambda_{ss}\sigma_{y,0} + (1 - \lambda_{ss})\sigma_{y,\infty}]}{\eta_p} \tag{A.21}$$

Considering the boundary condition $u_z = 0$ at $y = H$, it has the solution:

$$
\begin{aligned}
u_z = & \frac{1}{4k_1\eta_p} \left\{ \frac{\eta_p(k_2\eta_p - k_1\sigma_{y,\infty} + k_1 Fy)}{k_1 F} \sqrt{k_2^2 + \frac{k_1^2(\sigma_{y,\infty} - Fy)^2}{\eta_p^2} + \frac{2k_1 k_2(\sigma_{y,\infty} - 2\sigma_{y,0} + Fy)}{\eta_p}} \right. \\
& + \frac{4k_2\eta_p(\sigma_{y,\infty} - \sigma_{y,0})}{F} \ln\left[\eta_p k_2 - k_1(\sigma_{y,\infty} - Fy) + \eta_p\sqrt{k_2^2 + \frac{k_1^2(\sigma_{y,\infty} - Fy)^2}{\eta_p^2} + \frac{2k_1 k_2(\sigma_{y,\infty} - 2\sigma_{y,0} + Fy)}{\eta_p}} \right] \\
& \left. - y^2 k_1 F - 2y(k_2\eta_p + k_1\sigma_{y,\infty}) \right\} \\
& - \frac{1}{4k_1\eta_p} \left\{ \frac{\eta_p(k_2\eta_p - k_1\sigma_{y,\infty} + k_1 FH)}{k_1 F} \sqrt{k_2^2 + \frac{k_1^2(\sigma_{y,\infty} - FH)^2}{\eta_p^2} + \frac{2k_1 k_2(\sigma_{y,\infty} - 2\sigma_{y,0} + FH)}{\eta_p}} \right. \\
& + \frac{4k_2\eta_p(\sigma_{y,\infty} - \sigma_{y,0})}{F} \ln\left[\eta_p k_2 - k_1(\sigma_{y,\infty} - FH) + \eta_p\sqrt{k_2^2 + \frac{k_1^2(\sigma_{y,\infty} - FH)^2}{\eta_p^2} + \frac{2k_1 k_2(\sigma_{y,\infty} - 2\sigma_{y,0} + FH)}{\eta_p}} \right] \\
& \left. - k_1 FH^2 - 2H(k_2\eta_p + k_1\sigma_{y,\infty}) \right\}
\end{aligned}
\tag{A.22}
$$

B CONVERSION LATTICE UNITS TO REAL PARAMETERS

Due to the nature of the lattice Boltzmann method, it is necessary to convert the mesoscopic values to real values, and vice-versa. The procedure will depend on the information that is initially provided. For the case of a particle settling, the three known units are length, viscosity, and density. The conversion procedure is the follow (KRÜGER et al., 2017):

1. Define length conversion rate:
$$C_l = \frac{L}{N_x} = \frac{\Delta x}{h} \tag{B.1}$$

   where L is real characteristic length, N is the characteristic lattice length, Δx is the real length of one lattice unit and h is the size of one lattice unit, usually adopted as 1.

2. Define the lattice relaxation time used in the simulation and calculate the lattice viscosity:
$$\nu^+ = c_s^{+2} \left(\tau^+ - \frac{1}{2} \right) \tag{B.2}$$

   where τ^+ is the lattice relaxation time, c_s^+ is the lattice sound speed and ν^+ is the lattice kinematic viscosity.

3. Define the viscosity conversion rate:
$$C_\nu = \frac{\nu}{\nu^+} \tag{B.3}$$

   where ν is the real viscosity.

4. Determine the time conversion rate:
$$C_t = \frac{C_l^2}{C_\nu} = \frac{\delta}{\Delta t} \tag{B.4}$$

   where δ is the real time for one lattice time step and Δt is the step time size, usually adopted as 1.

5. Determine the velocity conversion rate:
$$C_u = \frac{C_l}{C_t} = \frac{U}{U^+} \tag{B.5}$$

   where U is the real velocity and U^+ is the lattice velocity.

6. Determine the correct value for the lattice gravity:
$$g^+ = g \frac{C_t}{C_u} \tag{B.6}$$

   where g is the real gravity and g^+ is the lattice acceleration field.

7. Define the density conversion rate
$$C_\rho = \frac{\rho}{\rho^+} \tag{B.7}$$

   where ρ is the real fluids density and ρ^+ is the lattice density, usually defined as 1.

8. Define mass conversion rate:

$$C_m = C_\rho C_l^3 \tag{B.8}$$

9. Define stress conversion rate:

$$C_p = C_\rho C_u^2 = \frac{C_m}{C_l C_t^2} = \frac{\sigma}{\sigma^+} \tag{B.9}$$

10. Determine the pressure field (KRÜGER et al., 2017):

$$P - P_0 = c_s^{+2} \left(\rho^+ - \rho_0^+ \right) C_p \tag{B.10}$$

where P_0 is the real reference pressure, P is the real pressure, $\left(\rho^+ - \rho_0^+ \right)$ is the lattice density variation.

C SPHERICAL MESH DISCRETIZATION

Meshing a sphere where the distance between the closest nodes is the same is a complicated task. Several methods can be found in the literature (KRÜGER et al., 2011) (KATANFOROUSH and SHAHSHA-HANI, 2003). On the icosahedron division, there is a fixed sequence of the number of nodes that the sphere can have, based on the number of iterations. Meanwhile using a randomized node placement followed by using the Coulomb law to distribute the nodes in the surface, similar to charged particles, allows a precise control on number of nodes but does not allow estimate the distance between the nodes before its execution. For this reason, will be used the Polar Coordinates Subdivision approach with a post-processing execution of the Coulomb energy optimization defined by Katanforoush and Shahshahani (2003). This formulation allows use the distance between nodes as input parameter while maintaining the distribution of distance between nodes narrow.

Defining the base distance between nodes equal to 1 for a sphere with radius of 5, result in a sphere composed of 263 nodes. The minimum node distance is 1.05 instead of the desired 1.0 while the maximum node distance is 1.55. This can be attributed by the irrationality of the circle perimeter when divided by an integer. To reduce this effect, the nodes positions are modified in order to minimize the potential Coulomb energy. The results of the Coulomb optimization are represented in the Fig. C.1 as a function of number of iterations used.

Figure C.1 – Relative Coulomb energy of each node without and with Coulomb energy optimization for a sphere with radius 5 lattice units.
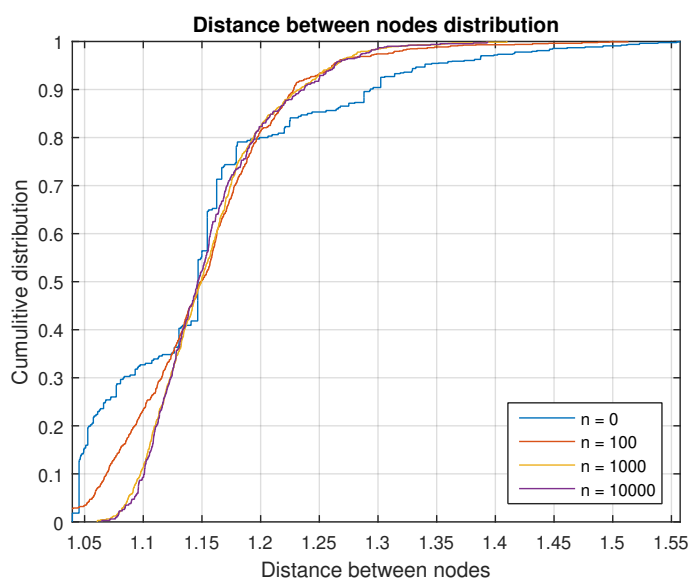
Source: Own elaboration.

As the number of iterations increased the node distribution trend to a stable configuration. This method smooth the distance between the nodes while also reducing the difference between the minimum and maximum distance.

The mesh structure of the spherical particle is represented in Fig. C.2. Where the colors of each node

represent the relative Coulomb energy while not optimized. The standard deviation of Coulomb energy for the not optimized mesh is 0.001 while for the optimized reduces to 8.36×10^{-6}, showing that the optimization smoothed the energy distribution in the sphere surface.

Figure C.2 – Relative Coulomb energy of each node without (a) and with Coulomb energy optimization (b) for a sphere with radius 5 lattice units.
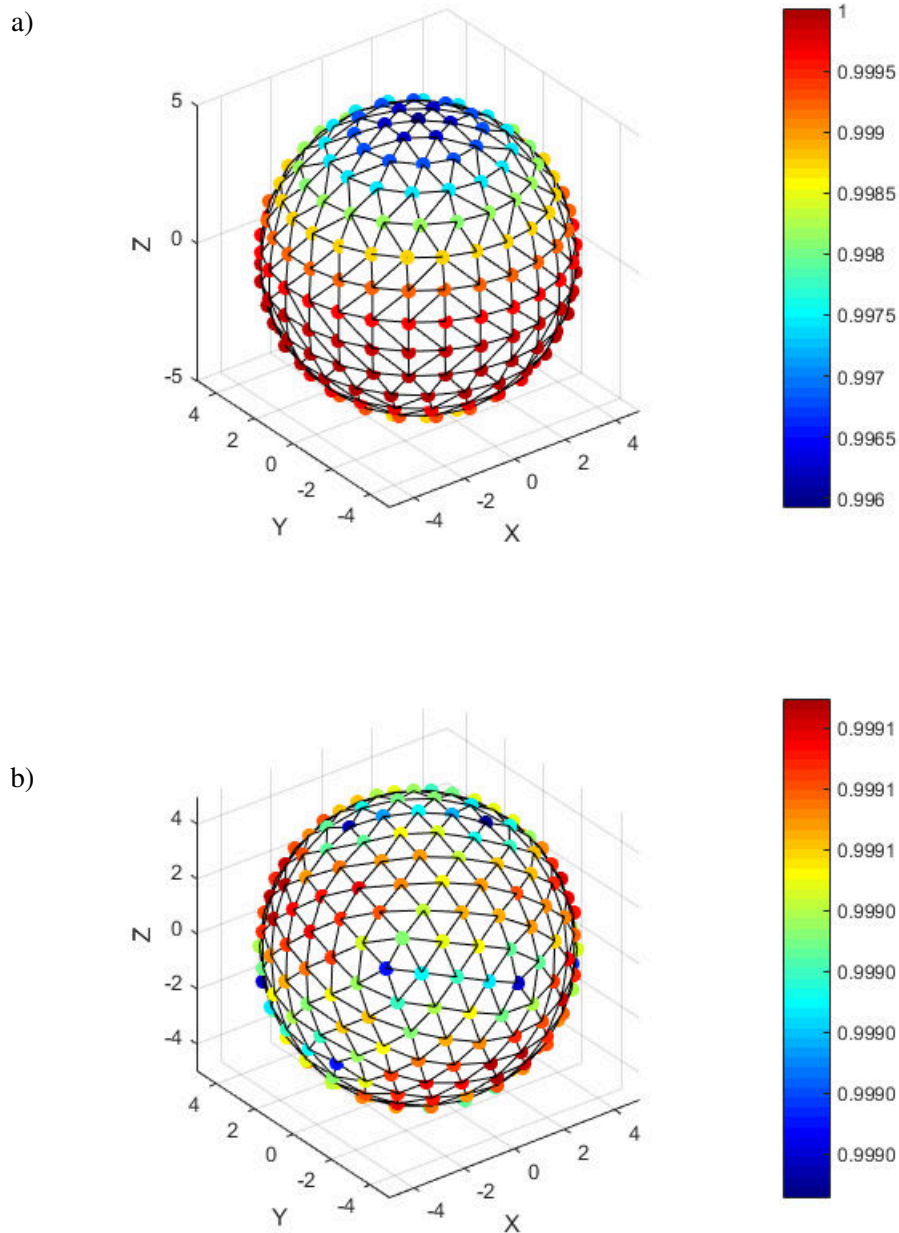
D DIMENSIONLESS EQUATIONS AND GROUPS

In this work, it was used the following normalization parameters:

$$l^* = \frac{l}{L_c} \tag{D.1a}$$

$$U^* = \frac{U}{U_0} \tag{D.1b}$$

$$t^* = t\frac{U_0}{L_c} \tag{D.1c}$$

$$\dot{\gamma}^* = \frac{L_c\dot{\gamma}}{U_0} \tag{D.1d}$$

$$\sigma^* = \frac{\sigma}{\eta_p}\frac{L_c}{U_0} \tag{D.1e}$$

where L_c is the characteristic length equal to the particle diameter, and $U_0 = (\rho_p - \rho_f)\,gL_c^2/\eta_p$ is the characteristic velocity of a settling particle. The constitutive equation, Eq. 4.32 in terms of apparent viscosity, transforms in:

$$\begin{cases} \eta = \lambda\frac{\mathrm{Bn_0}}{|\dot{\gamma}^*|} + (1-\lambda)\frac{\mathrm{Bn_\infty}}{|\dot{\gamma}^*|} + 1 & ,|\sigma^*| \geq \lambda\mathrm{Bn_0} + (1-\lambda)\,\mathrm{Bn_\infty} \\ \eta = \infty & ,|\sigma^*| < \lambda\mathrm{Bn_0} + (1-\lambda)\,\mathrm{Bn_\infty} \end{cases} \tag{D.2}$$

the kinetic equation:

$$\frac{\partial\lambda}{\partial t^*} + u^* \cdot \nabla\lambda = -k_1^*\lambda|\dot{\gamma}^*| + k_2^*(1-\lambda); \tag{D.3}$$

the mass and momentum transport equation, without static pressure, is:

$$\frac{\partial u_i^*}{\partial x_i^*} = 0 \tag{D.4}$$

$$\frac{\partial u_i^*}{\partial t^*} + u_j^*\frac{\partial u_i^*}{\partial x_j^*} = \frac{1}{\mathrm{Re}}\frac{\partial\sigma_{ji}^*}{\partial x_j^*} + F_i^* \tag{D.5}$$

and the particle movement equations, Eq. 4.51 and Eq. 4.54 is:

$$\rho_r\mathrm{Re}\frac{m_p}{\rho_pD^3}\frac{d\boldsymbol{U}^*}{dt^*} = \int_\Gamma \boldsymbol{\sigma}^* \cdot d\boldsymbol{S}^* + \frac{\mathbf{g}}{|\mathbf{g}|}\frac{m_p}{\rho_pD^3} \tag{D.6a}$$

$$\rho_r\mathrm{Re}\frac{\mathbf{I}}{D^5}\frac{d\boldsymbol{\omega}^*}{dt^*} = \int_\Gamma (\boldsymbol{X}^* - \boldsymbol{X}^*_p) \times \boldsymbol{\sigma}^* \cdot d\boldsymbol{S}^* \tag{D.6b}$$

These dimensionless equations have the following dimensionless groups:

- Bingham Number:

$$\mathrm{Bn}_x = \frac{\sigma_{y,x}}{\eta_p}\frac{L_c}{U_0} = \frac{\sigma_{y,x}}{(\rho_p - \rho_f)\,gD} \tag{D.7}$$

- Kinetic parameters:

$$k_1^* = k_1 \tag{D.8a}$$

$$k_2^* = k_2\frac{L_c}{U_0} = k_2\frac{\eta_p}{(\rho_p - \rho_f)\,gD} \tag{D.8b}$$

- Reynolds Number:

$$\text{Re} = \frac{\rho_f U_0 L_c}{\eta_p} = \frac{\rho_f \left(\rho_p - \rho_f\right) g D^3}{\eta_p^2} \tag{D.9}$$

- Density Ratio:

$$\rho_r = \frac{\rho_p}{\rho_f} \tag{D.10}$$

And in a steady-state regime:

- Thixotropic Number:

$$\text{Tx} = \frac{k_1^*}{k_2^*} \tag{D.11}$$

Is important to highlight that the Reynolds number here defined have the same form as the Archimedes numbers, defined in Chapter 2, differing by a factor of $4/3$. The same applies to the Bingham number, which will differ from the Yield number, defined in Chapter 3, by a factor of 3.

E SINGLE PARTICLE TERMINAL VELOCITY

ID	Bn_0	Bn_∞	k_1^*	$1/k_2^*$	U_t^*	ID	Bn_0	Bn_∞	k_1^*	$1/k_2^*$	U_t^*
000	0.000	0.000	0	0	0.036	041	0.046	0.023	2.25	344	0.000
001	0.028	0.000	2.25	689	0.015	042	0.046	0.012	2.25	344	0.004
002	0.034	0.000	2.25	689	0.013	043	0.046	0.012	2.25	689	0.004
003	0.040	0.000	2.25	689	0.010	044	0.046	0.012	2.25	2158	–
004	0.028	0.000	2.25	344	0.014	045	0.028	0.007	2.25	344	0.011
005	0.034	0.000	2.25	344	0.011	046	0.028	0.007	2.25	689	0.011
006	0.046	0.000	2.25	344	0.007	047	0.028	0.007	2.25	2158	–
007	0.040	0.000	2.25	344	0.009	048	0.012	0.003	2.25	344	0.021
008	0.019	0.000	2.25	344	0.019	049	0.012	0.003	2.25	689	0.021
009	0.012	0.000	2.25	344	0.023	050	0.012	0.003	2.25	2158	–
010	0.046	0.000	2.25	689	0.008	051	0.053	0.000	5.5	344	0.008
011	0.019	0.000	2.25	689	0.020	052	0.028	0.000	0.1	344	0.005
012	0.012	0.000	2.25	689	0.024	053	0.028	0.000	5.5	344	0.016
013	0.012	0.000	2.25	2158	–	054	0.028	0.000	0.025	344	0.003
014	0.019	0.000	2.25	2158	–	055	0.003	0.003	0.025	344	0.029
015	0.028	0.000	2.25	2158	–	056	0.006	0.006	0.025	344	0.023
016	0.034	0.000	2.25	2158	–	057	0.007	0.007	0.025	344	0.021
017	0.040	0.000	2.25	2158	–	058	0.014	0.014	0.025	344	0.012
018	0.046	0.000	2.25	2158	–	059	0.023	0.023	0.025	344	0.005
019	0.053	0.000	2.25	2158	–	060	0.012	0.012	2.25	689	0.015
020	0.053	0.000	2.25	689	0.006	061	0.040	0.040	2.25	2158	0.000
021	0.053	0.000	2.25	344	0.005	062	0.009	0.009	2.25	2158	0.018
022	0.053	0.000	1	344	0.003	063	0.021	0.021	2.25	2158	0.006
023	0.053	0.000	0.5	344	0.000	064	0.012	0.009	2.25	344	0.016
024	0.053	0.000	0.25	344	0.000	065	0.028	0.021	2.25	344	0.005
025	0.028	0.000	1	344	0.012	066	0.028	0.007	0.1	344	0.004
026	0.028	0.000	0.5	344	0.010	067	0.028	0.014	0.1	344	0.004
027	0.028	0.000	0.25	344	0.007	068	0.028	0.021	0.1	344	0.003
028	0.046	0.046	0.25	344	0.000	069	0.062	0.000	4.5	344	0.006
029	0.034	0.034	0.25	344	0.001	070	0.068	0.000	4.5	344	0.005
030	0.028	0.028	0.25	344	0.003	071	0.074	0.000	4.5	344	0.004
031	0.019	0.019	0.25	344	0.008	072	0.028	0.025	0.1	344	0.003
032	0.012	0.012	0.25	344	0.014	073	0.028	0.026	0.1	344	0.003
033	0.012	0.006	2.25	2158	–	074	0.028	0.027	0.1	344	0.003
034	0.012	0.006	2.25	689	0.019	075	0.028	0.028	0.1	344	0.003
035	0.012	0.006	2.25	344	0.018	076	0.012	0.012	2.25	344	0.014
036	0.028	0.014	2.25	2158	–	077	0.012	0.012	2.25	344	0.014
037	0.028	0.014	2.25	689	0.008	078	0.012	0.012	2.25	344	0.014
038	0.028	0.014	2.25	344	0.008	079	0.012	0.012	2.25	344	0.014
039	0.046	0.023	2.25	2158	–	080	0.012	0.012	2.25	344	0.014
040	0.046	0.023	2.25	689	0.002	081	0.090	0.000	4.5	344	0.003

ID	Bn_0	Bn_∞	k_1^*	$1/k_2^*$	U_t^*	ID	Bn_0	Bn_∞	k_1^*	$1/k_2^*$	U_t^*
082	0.100	0.000	4.5	344	0.002	151	0.062	0.000	2.25	344	0.004
083	0.110	0.000	4.5	344	0.001	152	0.068	0.000	2.25	344	0.003
084	0.120	0.000	4.5	344	0.000	153	0.074	0.000	2.25	344	0.002
101	0.012	0.000	0.025	344	0.015	154	0.062	0.000	1	344	0.000
102	0.012	0.000	0.1	344	0.016	155	0.068	0.000	1	344	0.000
103	0.012	0.000	0.25	344	0.018	161	0.009	0.000	4.5	344	0.027
104	0.012	0.000	0.5	344	0.020	162	0.006	0.000	4.5	344	0.029
105	0.012	0.000	1	344	0.021	163	0.003	0.000	4.5	344	0.033
106	0.012	0.000	2.25	344	0.023	164	0.015	0.000	4.5	344	0.022
111	0.019	0.000	0.025	344	0.009	165	0.002	0.000	4.5	344	0.034
112	0.019	0.000	0.1	344	0.011	201	0.046	0.023	4.5	344	0.002
113	0.019	0.000	0.25	344	0.013	202	0.053	0.026	4.5	344	0.000
114	0.019	0.000	0.5	344	0.015	203	0.062	0.031	4.5	344	0.000
115	0.019	0.000	1	344	0.017	211	0.046	0.012	4.5	344	0.005
116	0.019	0.000	2.25	344	0.019	212	0.053	0.013	4.5	344	0.004
121	0.034	0.000	0.025	344	0.001	213	0.062	0.015	4.5	344	0.002
122	0.034	0.000	0.1	344	0.002	214	0.068	0.017	4.5	344	0.000
123	0.034	0.000	0.25	344	0.005	215	0.074	0.019	4.5	344	0.000
124	0.034	0.000	0.5	344	0.007	216	0.090	0.022	4.5	344	0.000
125	0.034	0.000	1	344	0.010	221	0.046	0.012	2.25	344	0.004
131	0.040	0.000	0.025	344	0.000	222	0.053	0.013	2.25	344	0.002
132	0.040	0.000	0.1	344	0.000	223	0.062	0.015	2.25	344	0.000
133	0.040	0.000	0.25	344	0.002	224	0.068	0.017	2.25	344	0.000
134	0.040	0.000	0.5	344	0.005	225	0.074	0.019	2.25	344	0.000
135	0.040	0.000	1	344	0.007	231	0.046	0.012	1	344	0.002
141	0.046	0.000	0.025	344	0.000	232	0.053	0.013	1	344	0.000
142	0.046	0.000	0.1	344	0.000	241	0.046	0.012	0.5	344	0.000
144	0.046	0.000	0.25	344	0.000						
143	0.046	0.000	0.5	344	0.003						
145	0.046	0.000	1	344	0.005						